Catalyst Substrate Interaction of Organo Phosphate Brønsted Acid Catalysts with Imines

Dissertation

zur Erlangung des Grades

„Doktor der Naturwissenschaften“

im Promotionsfach Chemie

am Fachbereich 09

Chemie, Pharmazie, Geographie und Geowissenschaften

der Johannes Gutenberg-Universität Mainz

Christian Malm

geboren in Diez

Mainz, 2019

1. Berichterstatter: XXX

2. Berichterstatter: XXX

Tag der mündlichen Prüfung: 30.10.2019

Statutory Declaration

I hereby declare that I wrote this dissertation submitted without any unauthorized external assistance and used only sources acknowledged in the work. All textual passages which are appropriated verbatim or paraphrased from published and unpublished texts as well as all information obtained from oral sources are duly indicated and listed in accordance with bibliographical rules. In carrying out this research, I complied with the rules of standard scientific practice as formulated in the statutes of the Johannes Gutenberg-University Mainz to insure standard scientific practice. In the chapters 4 to 6, I will write in the first person plural instead of singular (we instead of I) to make the text more readable.

Christian Malm

"It's the question we can't answer
that teach us the most.
They teach us how to think.
If you give a man an answer,
all he gains is a little fact.
But give him a question
and he'll look for his own answers."

Patrick Rothfuss
in The Wise Man's Fear

Abstract

In this thesis, I study the interaction of Brønsted acid organocatalysts with imines. I answer the question, which species are formed and quantify their association constants. In my work, I investigate the solvent dependence of those association constants and compare the results for two different imines in order to generalize my findings. My results show that the formed aggregates are based on very strong doubly ionic hydrogen bonds in which the proton vibrations are strongly coupled. Apart from this, I find the proton residing in a very anharmonic energy potential, which strongly affects the energies of the vibrational transitions. I use linear and non-linear infrared (IR) spectroscopy as well as nuclear magnetic resonance (NMR) and dielectric relaxation spectroscopy (DRS).

In order to address the question which species are formed in solutions of a Brønsted acid organocatalyst and an imine, I first present the results for a model system. I choose diphenyl phosphate (DPP) as the catalyst and quinaldine (Qu) as the imine for my study. My concentration-dependent NMR and DRS experiments in dichloromethane (DCM) provide evidence for not only the formation of ion-pairs, but also of multimers, such as trimers consisting of one Qu and two DPP molecules. The presence of multimers in solution and their possible contribution to the catalytic process could explain the high catalyst loadings, which are needed in organocatalysis.

A major challenge in the field of organocatalysis remains the development of rational catalyst design. I address this topic in my thesis by quantifying the ion-pair and multimer formation of DPP with two imines (quinaldine and 2-phenylquinoline) in three different solvents (DCM, chloroform, and tetrahydrofuran). I find a correlation of the solvents hydrogen bonding affinity with the yield of the reaction and the strength of its ion-pair formation.

Finally, I use optical spectroscopy to take a detailed look at the interaction motif within the ion-pair. Here, I apply linear and non-linear IR spectroscopy to study the vibrations related to the acidic proton, which governs the catalyst-substrate interaction. The concentration-dependent linear IR data show that doubly ionic hydrogen bonds are formed between the catalyst and the substrate. By means of non-linear IR spectroscopy, I observe very fast dynamics related to the acidic proton vibrations. Further, the 2D-IR data suggest that this vibration is strongly coupled to lower-frequency modes and that the proton resides within a very anharmonic energy potential, which is supported by *ab initio* calculations. The strong coupling may allow for efficient excess energy dissipation, which is a potential pathway for energy transport during the catalytic transfer hydrogenation reaction.

Zusammenfassung

Im Rahmen meiner Doktorarbeit habe ich die Wechselwirkung von Brønsted Säure Organokatalysatoren mit Iminen untersucht. Hierbei habe ich die Frage beantwortet welche Aggregate in Lösung gebildet werden und deren Assoziationskonstanten bestimmt. Außerdem habe ich die Lösungsmittelabhängigkeit der Assoziations-konstanten für die einzelnen Aggregate untersucht. Um eine allgemeinere Aussage treffen zu können, habe ich die Assoziationskonstanten für zwei verschiedene Imine in drei verschiedenen Lösungsmitteln bestimmt. Meine Untersuchungen haben gezeigt, dass die gebildeten Aggregate von doppelt ionischen Wasserstoffbrücken zusammengehalten werden, in denen die Schwingungen des aziden Protons sehr stark gekoppelt sind. Dieses Proton befindet sich in einem sehr anharmonischen Energiepotential, welches die Energien der Schwingungsübergänge beeinflusst. Meine hier präsentierten Ergebnisse beruhen sowohl auf linearer und nicht-linearer Infrarot (IR) Spektroskopie als auch auf Kernspinresonanz- (NMR) und dielektrischer Relaxationsspektroskopie (DRS).

Um die Frage zu beantworten, welche Aggregate in einer Lösung von Brønsted Säure Organokatalysatoren und Iminen gebildet werden, habe ich ein Modelsystem untersucht. Dieses besteht aus dem Brønsted Säure Organokatalysator Diphenylphosphat (DPP) und dem Imin Quinaldin (Qu). Mittels einer konzentrationsabhängigen NMR und DRS Studie im Lösungsmittel Dichlormethan (DCM) konnte ich nicht nur zeigen, dass Ionenpaare gebildet werden, sondern auch, dass zusätzlich Multimere, wie zum Beispiel Trimere aus einem Qu und zwei DPP Molekülen gebildet werden. Die Existenz von Multimeren in Lösung und deren möglicher Beitrag zur Katalyse könnten die hohen Katalysatormengen erklären, die in der Organokatalyse benötigt werden.

Eine große Herausforderung in der Organokatalyse ist die Erarbeitung eines „rational design“ zur effizienteren Entwicklung neuer katalysierter Prozesse. Meine Arbeit trägt dazu mit der Quantifizierung der Ionenpaar- und Multimerbildung bei. Um eine allgemeinere Aussage treffen zu können habe ich meine Studie auf zwei Imine (Quinaldin und 2-Phenylquinolin) in drei verschiedenen Lösungsmitteln (DCM, Chloroform und Tetrahydrofuran) ausgedehnt. Hierbei konnte ich feststellen, dass eine Korrelation zwischen der Wasserstoffbrückenbildungsaffinität, der Reaktionsausbeute, sowie der Stärke der Ionenpaarbildung im jeweiligen Lösungsmittel besteht.

Zusätzlich habe ich die Wechselwirkungen im Ionenpaar mit optischer Spektroskopie genauer untersucht. Hierbei habe ich lineare und nicht-lineare IR Spektroskopie verwendet um die Schwingungen des aziden Protons zu betrachten. Mit Hilfe von konzentrationsabhängigen linearen IR Messungen konnte ich zeigen, dass doppelt ionische Wasserstoffbrückenbindung in den Katalysator-Substrat Ionenpaaren gebildet werden. Deren sehr schnelle Schwingungsdynamik konnte ich mit nicht-linearer IR Spektroskopie zeigen. Außerdem legen die 2D-IR Spektren nahe, dass die Schwingungen in denen das azide Proton involviert ist, stark zu Schwingungsmoden bei niedrigen Frequenzen gekoppelt sind, was auch durch *ab initio* Berechnungen gestützt wird. Die

starke Kopplung ermöglicht effiziente Energiedissipation und ist ein potenzieller Pfad für den Energietransport während der katalysierten Transfer-Hydrierungs Reaktion.

This thesis is based on the following publications:

Chapter 4:

C. Malm, H. Kim, M. Wagner and J. Hunger, Complexity in acid-base titrations: Multimer formation between phosphoric acids and imines, *Chem. - A Eur. J.*, 2017, **23**, 10853–10860.

Chapter 5:

C. Malm, L. A. Prädel, A. Ehrhard, M. Wagner, J. Hunger, Determining association equilibria of Brønsted acid organocatalysts with imines - a combined dielectric and nuclear magnetic resonance approach. *(in preparation)*

Chapter 6:

C. Malm, L. A. Prädel, B. Marekha, M. Grechko, J. Hunger, Vibrational dynamics of doubly ionic hydrogen-bonded Brønsted acid-base pairs and multimers. *(submitted)*

Other publications:

H. S. Varol, M. A. Sánchez, H. Lu, J. E. Baio, **C. Malm**, N. Encinas, M. R. B. Mermet-Guyennet, N. Martzel, D. Bonn, M. Bonn, T. Weidner, E. H. G. Backus and S. H. Parekh, Multiscale effects of interfacial polymer confinement in silica nanocomposites, *Macromolecules*, 2015, **48**, 7929–7937.

H. S. Varol, F. Meng, B. Hosseinkhani, **C. Malm**, D. Bonn, M. Bonn, A. Zaccone and S. H. Parekh, Nanoparticle amount, and not size, determines chain alignment and nonlinear hardening in polymer nanocomposites, *Proc. Natl. Acad. Sci.*, 2017, **114**, E3170–E3177.

J. Luo, Y. Ao, **C. Malm**, J. Hunger, Q.-Q. Wang and D. Wang, Tritopic ion-pair receptors based on anion–π interactions for selective CaX 2 binding, *Dalt. Trans.*, 2018, **47**, 7883–7887.

V. Balos, B. Marekha, **C. Malm**, M. Wagner, Y. Nagata, M. Bonn and J. Hunger, Specific ion effects on an oligopeptide: Bidentate binding matters for the guanidinium cation, *Angew. Chemie Int. Ed.*, 2019, **58**, 332–337.

A. A. Ehrhard, S. Jäger, **C. Malm**, S. Basaran and J. Hunger, CF3-groups critically enhance the binding of thiourea catalysts to ketones – a NMR and FT-IR study. *J. Mol. Liq. (accepted)*

Contents

1 Introduction

1.1 Brønsted acid organocatalysis

Catalysts possess the unique ability to lower the activation energy of a chemical reaction without being consumed.[1,2] Therefore, they play a crucial role in the synthesis and refinery of chemicals, as well as in pollution reduction.[3] In fact, 90 % of all chemical manufacturing processes in the US involve catalysts.[3] In homogeneous catalysis, where both catalyst and solvent exist in the same phase (e.g. a solution), metal catalysts are often used. The ability of metal catalysts to perform enantioselective reactions is used in the synthesis of pharmaceutics, flavours, and other fine chemicals.[2,4] However, metals have the disadvantages of high prices, air, moisture sensitivity, and toxicity. Therefore, organocatalysts, as metal-free options have been developed. They provide good stereo control while they are easier to handle, as they are not oxidized in air. Also, many organocatalysts are small molecules and thus easy to handle and cheap in production. Further, the removal of the toxic metal-based catalyst from the product and waste streams can be avoided by the use of non-toxic organocatalysts. Thus, the development of organocatalysts allows for cheap access to chiral products by providing simpler synthetic pathways.[2,5] A particularly interesting type of catalysts are Brønsted acid organocatalysts. These have the ability to catalyse the transfer hydrogenations of imine substrates.[6] Here, the interaction of the acid catalyst with the imine substrate results in the activation of the substrate and provides excellent stereo control when chiral catalysts are employed.[6–9] The field of Brønsted acid catalysis was first introduced by Akiyama[10,11] and has evolved quickly based on studies by Rueping, List, MacMillan, and others.[5,12–15] A key advantage of the new Brønsted acid catalysts over transition metal catalysts is that they are metal-free and therefore not sensitive to air or moisture.[5,11] However, they require relatively high catalyst loadings to work efficiently.[9,16] Even though, there is a lot of progress in the field of Brønsted acid organocatalysts, there are still many unsolved questions.

The catalytically active sites of organocatalysts are functional groups, for example phosphoric acid groups.[9] The use of acids results in the protonation of basic substrates. An example is the use of organo phosphate catalysts with imine substrates in nonpolar solvents. Here, the imine is protonated and an ion-pair (i.e. doubly ionic hydrogen bond[17]) is formed.[6–8,18] The protonation of the base by the acid and the continued strong interaction of the ion-pair results in the activation of the substrate and enables excellent stereo control.[7–9] However, the precise nature of the catalyst substrate interaction and how it governs the catalysis, especially in stereoselective reactions, is not fully understood.[18] Nevertheless, it is known that the interaction is based on the protonation of the substrate and the formation of non-covalent bonds, which leads to the catalytic activation of the substrate.[12] Unsurprisingly, with the protonation as a key element, it was further found that the rate constant increases with increasing catalyst acidity. It is, however, important to avoid too strong interactions, which can lead to catalyst inhibition.[9] Consequently, it was found that the solvent, which affects the acid-base

interaction,[19] also strongly influences Brønsted organo phosphate catalysis. The yield and selectivity of the hydrogenation of imines strongly depend on the solvent.[20] Even though, reaction mechanisms for organocatalytic processes,[9,12] such as the hydrogen transfer reaction have been proposed,[6] it remains a major challenge to come up with a rational design for catalyst development. Although, this challenge has been approached and there have been attempts to provide a pathway to rational design for the development of new catalysts, it is challenging to predict the stereoselectivity of the catalysis, for unknown combinations of chiral catalysts and substrates.[9,21] Milo et al. used vibrational spectroscopy of the catalyst in order to predict the stereoselectivity of the reaction product,[22,23] while the group of Akiyama used nuclear magnetic resonance (NMR) spectroscopy.[24] However, no clear approach to a rational design could yet be presented.[9]

The correlation of acidity and catalyst performance[9] suggests that the hydrogen bond of the organocatalyst to the substrate and the proton within are key elements to the catalytic process. Thus, they need to be fundamentally understood in order to achieve a rational design. With NMR the splitting of the proton peak upon cooling was found[25] and the peaks have been assigned to neutral hydrogen bonds coexisting with ion-pairs,[25] which is in contrast to more recent findings, that ion-pairs are the dominant species for catalysis[18]. The origin of those NMR peaks and some surprising chemical shift changes with concentrations have not been explained, this finding, however, suggested that more than one species is present.[18,25] Other approaches used vibrational resonances, however the molecular origin of the resulting changes to the vibrational spectrum remain somewhat unclear.[22,23] Furthermore, the influence of solvent effects on the catalyst-substrate interaction is poorly understood.[18] To address these challenges I studied the organocatalyst-substrate interaction, which is the topic of this thesis. Therefore, I will discuss the influence of different solvents and concentrations on the catalyst-substrate interaction. Here, I will unravel which species are formed in solution and determine the charge distribution by means of a combined approach using NMR and dielectric relaxation spectroscopy (DRS). Further, I will use infrared spectroscopy and DFT calculations in order to elucidate the molecular origins of the infrared absorptions. Here, I will focus on organo phosphate Brønsted acid catalysts, as they belong to the most versatile organocatalysts[9] and therefore might allow to draw general conclusions about the nature of the catalyst substrate interaction. The organo phosphate based Brønsted acid catalysts range from simple achiral diphenyl phosphate[16] to advanced 1,1'-Bi-2-naphthol (BINOL) phosphoric acids and beyond.[9] The organocatalytic transfer hydrogenation of quinoline derivates is of special interest,[6] as this stereoselective reaction to 1,2,3,4-tetrahydroquinoline derivatives (see Figure 1.1a) can be used as a pathway to alkaloids which are potential antimalarial drugs (see Figure 1.1b).[26]

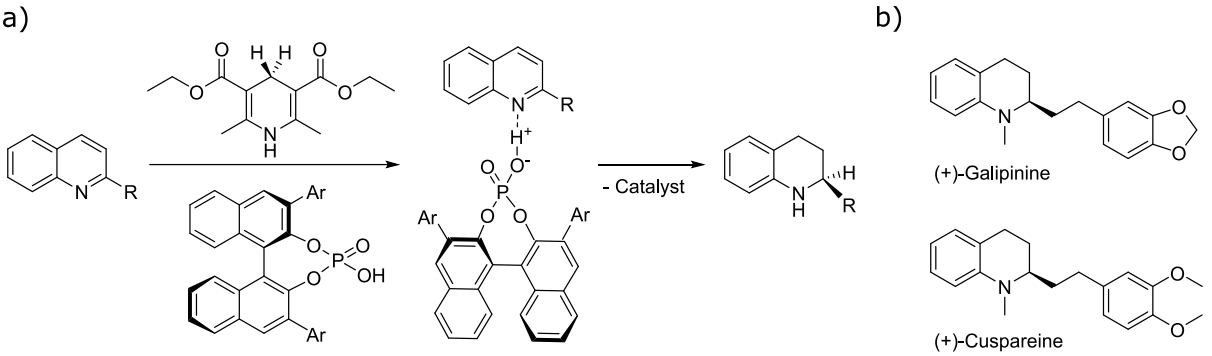

Figure 1.1 a) shows the organocatalytic transfer hydrogenation of a quinoline derivate to a 1,2,3,4-tetrahydroquinoline derivate. A Hantzsch ester is used as hydride donor and BINOL-phosphate as chiral Brønsted catalyst, which ensures high stereoselectivities.[6,9] In b) the alkaloids Galipinine and Cuspareine are shown, both of them are potential antimalarial drugs,[26] which can be synthesized using the organocatalytic reaction shown in a).[6]

In this thesis, I employed physico-chemical methods to study the catalyst-substrate interaction of Brønsted acid organocatalysts and quinoline derivatives. NMR and dielectric relaxation spectroscopy were used to study the aggregation and interaction of catalyst and substrate. Further, I determined the species contributing to the catalysis using NMR and DRS as these methods may give insights into the aggregation processes in solutions of organo phosphates and quinolone derivatives in nonpolar solvents. I used linear and non-linear infrared spectroscopy in order to investigate the proton within the hydrogen bond and unravel its energy potential.

1.2 Hydrogen bonds

Hydrogen bonds are one of the most fundamental molecular interactions.[27] They exist in nature, where they not only cause the extremely high melting and freezing points of water[28], but also define the structure of DNA double helix[29] to just name two very prominent examples. Thus, without hydrogen-bonding, there would not be life as we know it.[30] A hydrogen bond can generally be described as the attractive interaction of a hydrogen bond donor A-H and a hydrogen bond acceptor group B. The interactions are governed by Coulomb interactions as well as van der Waals and dispersion forces. This results in binding energies between 4 and 50 kJ mol^{-1}, which are much smaller than those of covalent bonds.[31] The relatively low binding energies allow hydrogen bonds being broken and formed at ambient temperatures,[31] which makes them a versatile binding motif in the field of supramolecular chemistry.[32] The dynamics of the hydrogen bond formation and breaking in liquids usually occur on ps timescales, while small structural fluctuations in water were found on a much faster (sub 100 fs) timescale.[33,34]

Infrared spectroscopy of the A-H stretch vibration has proven to be a convenient probe to study hydrogen-bonded systems. This vibration is very sensitive to the formation of hydrogen bonds and exhibits a significant shift to lower frequencies upon hydrogen bond

formation as well as an enhanced anharmonicity of the proton transfer energy potential.[31,35]

In general, hydrogen bond strengths are classified as weak, medium-strong, or strong. The most prominent example of a weak hydrogen bond is a water-water bond as in liquid water, where water molecules form a hydrogen-bonded network. Thus, the frequency of the OH stretch vibration, in hydrogen-bonded water, exhibits a red-shift in the frequency[30] (Figure 1.2b), as compared to free OH vibrations at 3700 cm^{-1} (Figure 1.2a).[36] A hydrogen bond is defined as weak when the distance between A and B ($R_{AH...B}$) is between 3.0-2.8 Å. If the distance is longer than that, it is considered as free A-H (O-H in the case of water).[30]

If $R_{AH...B}$ is between 2.6 and 2.8 Å, the hydrogen bond is considered medium-strong (Figure 1.2c).[30] The strength of a medium-strong hydrogen bond can be up to 35 kJ mol^{-1}.[31] The A-H stretch vibration experiences a red-shift of 300-1000 cm^{-1} accompanied by an increase in the integrated intensity of the band. The bands of the A-H stretch vibration are usually broad (~500 cm^{-1}) and also show irregular structures. Such structures are usually assigned to overtones and combination bands.[30,37] An example of a medium-strong hydrogen bond is the formic acid homodimer.[30]

The last category of hydrogen bonds is that of strong hydrogen bonds. These are divided into two groups, one with asymmetric energy potentials and one with symmetric energy potentials along the proton transfer coordinate. Systems with a strong hydrogen bond between charged atoms of two different molecules ($A^- \cdots H\text{-}B^+$) belong to the first group with asymmetric potentials. Such hydrogen bonds are called doubly ionic hydrogen bonds[17], in order to make clear that such ion-pairs are hydrogen-bonded and to also distinguish those species from regular neutral hydrogen bonds. Such doubly ionic hydrogen bonds usually belong to the last category of hydrogen bonds that is, strong hydrogen bonds (Figure 1.2d-e). The red-shift and the broadness of their A-H stretching band increase with decreasing A to B distance $R_{AH...B}$. Examples for hydrogen bonds with asymmetric energy potentials are heterodimers or ion-pairs. Their infrared stretching spectra are similar to the spectrum shown in Figure 1.2d. Their spectra usually show a pattern consisting of three peaks, often called A,B,C-type spectra. The origin of the A,B,C-type pattern has been assigned to Fermi resonances of the A-H stretching mode with in- and out-of-plane A-H bending modes.[30] The A-H stretching mode has a very intense band at frequencies of 1500-2000 cm^{-1}. The behaviour of this A-H stretch band upon deuteration is surprising, as little to no detectable shifts in the frequency of the AH band can be found.[30] The diphenyl phosphoric acid and quinaldine ion-pair system, which is studied in this thesis belongs to the category of strongly hydrogen-bonded systems, as it contains a doubly ionic hydrogen bond.

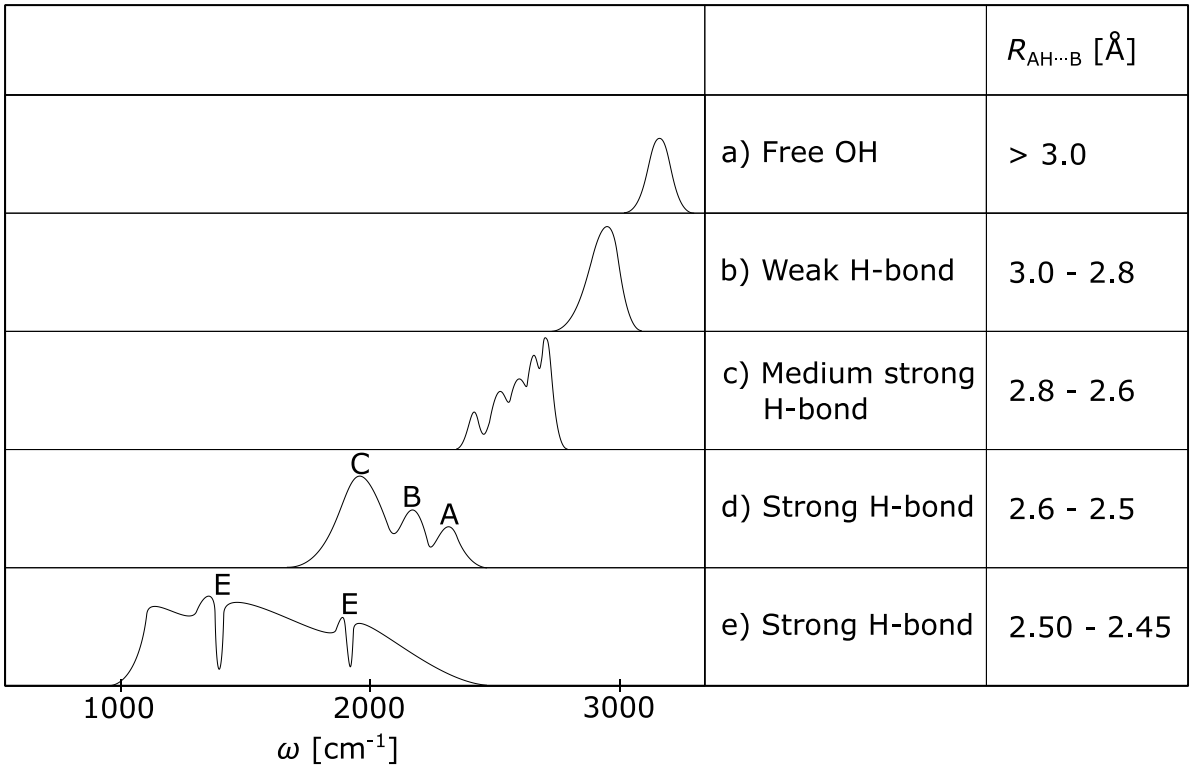

Figure 1.2 shows the peak positions and shapes for the A-H stretch bands for hydrogen bonds of different strength and with different A to B bond length $R_{AH\cdots B}$.[30]

For even stronger hydrogen bonds, with A···B distances as short as 2.50-2-45 Å, the energy potential is a symmetric, or almost symmetric, double-well potential.[30] The corresponding infrared signal is a continuous band which contains sharp transmission windows, the so called Evans holes (marked with E in Figure 1.2e).[30,38,39] The Evans hole describes the dip in the absorption spectrum, which is caused by a Fermi resonance of the A-H stretch and the A-H deformation modes.[30]

It can in general be stated that hydrogen-bonded species result in a broad variety of spectral features in the infrared frequency range, which are not trivial to understand completely.[30] Here, non-linear spectroscopy has proven to be a well-suited tool to study hydrogen-bonded systems, as it can unravel the dynamics as well as couplings for example to lower frequency modes.[31] Non-linear IR spectroscopy was used, for example, to show the presence of anharmonic coupling to low-frequency modes in acetic acid homodimers.[37] Therefore, I also used non-linear IR spectroscopy to study hydrogen-bonded systems. However, the focus of this thesis is not on homodimers, but on strongly bond, doubly ionic hydrogen bonds. In the following I will discuss the used experimental techniques in detail.

2 Theory

2.1 Overview

In order to study the catalyst-substrate interaction of Brønsted acid organocatalysts with quinoline derivatives, several techniques are applied. In this chapter those techniques will be discussed: First, the optical spectroscopies, which are Fourier-transform infrared spectroscopy and non-linear infrared spectroscopy, followed by dielectric relaxation and nuclear resonance spectroscopy.

2.2 Linear infrared spectroscopy

The vibrations of molecules can be investigated by means of infrared (IR) spectroscopy. IR spectroscopy allows studying molecules on the time scale of nuclear motion. To this end, the oscillations of chemical bonds within molecules are studied. In a simplified approach, they can be described as harmonic oscillators.[40]

$$\nu = \frac{1}{2\pi} \cdot \sqrt{\frac{k_f}{m^*}} \tag{2.1}$$

The frequency ν is a function of the force constant k_f and the reduced mass m^*.[40] The potential V of a harmonic oscillator as a function of the displacement r also depends on the force constant.[41]

$$V(r) = \frac{1}{2} k_f r^2 \tag{2.2}$$

However, in the case of molecular vibrations, only certain energies of the oscillator are possible. The system is quantized, and its energy E depends on the Planck constant h and the quantum number υ, which must be a positive integer.[42]

$$E = h\nu \left(\upsilon + \frac{1}{2}\right) \tag{2.3}$$

Classically, a particle can be described by its position r and its velocity v. In quantum mechanics, the state of a particle is described by a wave function Ψ. The square of the

absolute value of the wave function (the probability density function) $|\Psi|^2$ of a particle is a measure for the probability to find the particle at a given position.[41,43]

When electromagnetic radiation, such as light or infrared light shines on molecules, the oscillators interact with the electromagnetic waves of the radiation. The energy of the radiation can, for example, excite the system from the ground state with the quantum number $\upsilon = 0$ to the first excited state $\upsilon = 1$. Here, the energy of the electromagnetic wave is defined by its frequency ω. Therefore, the time dependence of the electric field $\vec{E}(t)$ of a monochromatic electromagnetic wave can be described with the following expression:[42,43]

$$\vec{E}(t) = \vec{E}_0 \cos(\omega t) \tag{2.4}$$

The field is a function of time t, the frequency of the wave ω and the amplitude of the electric field $\vec{E}_0$. The interaction of light and matter can be described as an electromagnetic wave $\vec{E}$ (light) putting a force on the nuclei and the electron cloud of atoms and molecules (matter). The displacement of the electrons and nuclei induces a polarization $\vec{P}$ in the matter, which can macroscopically be described as the mean electric dipole moment $\langle\mu\rangle$ of the molecules multiplied with the number density $\mathcal{N}$.[1,42]

$$\vec{P} = \langle\mu\rangle\mathcal{N} \tag{2.5}$$

For weak electric fields, a linear correlation between the induced polarization and the electric field strength is found, which can be described with the following equation.[42]

$$\vec{P} = \varepsilon_0 \chi^{(1)} \vec{E} \tag{2.6}$$

Here the material-dependent constant $\chi^{(1)}$ is the linear susceptibility and ε_0 is the permittivity of free space. Interactions governed by the 1st order susceptibility are the basis of linear infrared spectroscopy.[42] A transition in a harmonic oscillator is IR active if it fulfills the following selection rules: The vibrational quantum number υ changes by 1.[43]

$$\Delta\upsilon = \pm 1 \tag{2.7}$$

Further, the transition dipole moment $\vec{R}_v$ has to change upon the transition. The transition dipole moment describes the transition from one state Ψ_v' to another state Ψ_v''.[43]

$$\vec{R}_v = \int \Psi_v'^* \hat{\mu} \Psi_v'' \mathrm{d}r \tag{2.8}$$

The transition dipole moment depends on the coordinate r, which is the displacement from the internuclear equilibrium position, and the dipole moment operator. This can be expressed as shown below using the first non-zero term of a Taylor series.[43]

$$\vec{R}_v = \left(\frac{\mathrm{d}\mu}{\mathrm{d}r}\right)_\mathrm{e} \int \Psi_v'^* r \Psi_v'' \mathrm{d}r \tag{2.9}$$

However, most systems are not purely harmonic, but contain a certain anharmonicity, as the potential V is not infinitely high at infinite displacement r of the oscillator from the equilibrium position r_e. Instead, there is a finite energy at which the bond breaks. This energy is the dissociation energy D_e. Close to the dissociation energy, the potential increases less steeply with r. This behaviour can be described by the Morse-potential:[1,43]

$$V = D_e\left(1 - e^{-a(r-r_e}\right) \tag{2.10}$$

Here, the potential V is given by the depth of the potential minimum D_e, which is the dissociation energy. It is a function of the distance r from the equilibrium distance r_e and the stiffness of the potential a. The vibrational energy E for the harmonic oscillator (see eq. (2.3)) can be expressed by its vibrational term (the eigenenergy) $G(v)$ in wavenumbers ω.[1,43]

$$G(v) = \frac{E}{hc} = \omega\left(v + \frac{1}{2}\right) \tag{2.11}$$

In case of an anharmonic oscillator, the vibrational term follows a power series, governed by the anharmonic constants $k_a = \omega_e a$, $k_b = \omega_e b$, and higher orders, based on the perturbative approach. The constants k_a and k_b depend on the frequency of the oscillator close to equilibrium ω_e and can be written as the product of ω_e and a constant, as it is used in the following. [1,42,43]

$$G(v) = \omega_e \left(v + \frac{1}{2}\right) - \omega_e a \left(v + \frac{1}{2}\right)^2 + \omega_e b \left(v + \frac{1}{2}\right)^3 + \ldots \tag{2.12}$$

The dissociation energy D_e can be approximated by solving the Schrödinger equation for the Morse potential, while only taking the first two terms into account (up to $\omega_e a$).[1,43]

$$D_e \cong \frac{\omega_e^2}{4\omega_e a} \tag{2.13}$$

In Figure 2.1 the potential energy as function of the internuclear distance is shown. The harmonic energy potential has equally spaced states and transition energies (Figure 2.1a). In the case of an anharmonic potential, the spacing of the states is not uniform anymore and thus the transition energies decrease with increasing energy (Figure 2.1b). The vibrational transitions of such potentials can be probed by infrared radiation. Here, linear infrared spectroscopy can be used to study the transition from the ground to the first vibrationally excited state. In order to study the anharmonicity of a vibrational energy potential, non-linear infrared spectroscopy can be applied, which will be discussed in the next section.[43]

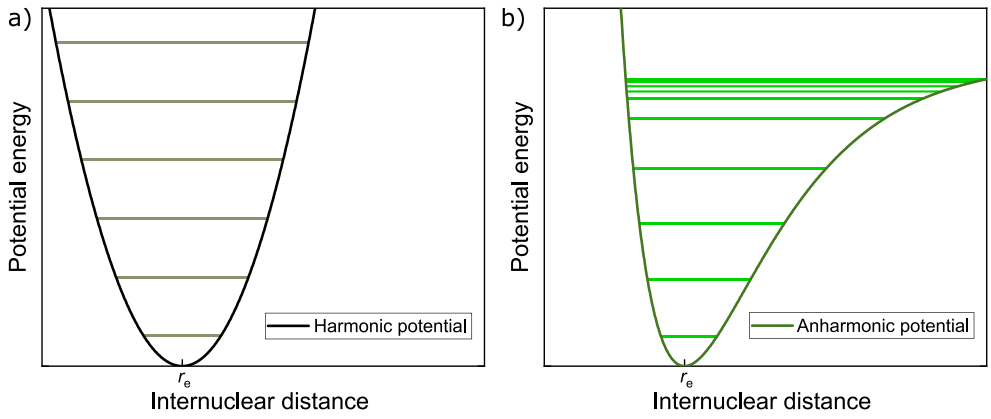

Figure 2.1 a) shows a harmonic potential around the equilibrium position of the oscillator r_e. The harmonic potential has equally spaced energy levels in contrast to the anharmonic Morse-potential b).

2.3 Non-linear infrared spectroscopy

When strong electric fields are applied, which can be induced by using a laser, nonlinear effects occur. In this case, the polarization has to be described by additional higher-order terms, since eq. (2.6) is not sufficient anymore.[42]

$$\vec{P} = \varepsilon_0\left(\chi^{(1)}\vec{E} + \chi^{(2)}\vec{E}^2 + \chi^{(3)}\vec{E}^3 + \ldots\right) = \vec{P}^1 + \vec{P}^2 + \vec{P}^3 + \ldots \tag{2.14}$$

The higher-order terms here are $\chi^{(2)}$, the second-order susceptibility and $\chi^{(3)}$ the third-order susceptibility. Those susceptibilities are second- and third-rank tensors, respectively. The contributions can be summarized as the first, second, and third-order nonlinear polarizations (see eq. (2.14)). The third-order processes can be used to observe processes in bulk and are relevant to pump-probe and 2D-IR spectroscopy.[42]

In the following, the interaction of an isolated molecule with a laser pulse is described. It is assumed that the molecule has two vibrational states, the ground state $|0\rangle$ and the excited state $|1\rangle$. The wave function $|\psi\rangle$ of the molecule is defined by the time-dependent Schrödinger equation. $\hbar$ is the reduced Planck constant and t the time.[42,44]

$$i\hbar\frac{\partial}{\partial t}|\psi\rangle = \hat{H}|\psi\rangle \tag{2.15}$$

The Hamiltonian $\hat{H}$ consists of a time-independent Hamiltonian $\hat{H}_0$ for the molecule and $\hat{W}(t)$ is a perturbation, representing the energy of the molecule-laser pulse interaction.[44]

$$\hat{H} = \hat{H}_0 + \hat{W}(t) \tag{2.16}$$

To describe the interaction of the molecule with the laser, the perturbation is a function of the external electric field $\vec{E}(t)$ and the dipole operator of the molecule $\hat{\mu}$.[44]

$$\hat{W}(t) = -\hat{\mu}\,\vec{E}(t) \tag{2.17}$$

When there is no laser pulse present, and thus no external electrical field, the interaction term is zero $\hat{W}(t) = 0$. Therefore, the wave function for the two-state system of our molecule is given by the following expression.[44]

$$|\psi(t)\rangle = c_0 e^{-\frac{iE_0 t}{\hbar}}|0\rangle + ic_1 e^{-\frac{iE_1 t}{\hbar}}|1\rangle \tag{2.18}$$

Without interaction of the laser pulse with the molecule, it is usually in the vibrational ground state $|0\rangle$. Upon the interaction with the laser pulse, the system is in a linear

combination of the vibrational ground state $|0\rangle$ and the vibrational excited state $|1\rangle$. Therefore, the wave function is altered, which is described by changes in the coefficients c_0 and c_1, which change over time. In order to simplify the equation, we define the energy difference between both states of our molecule as $\omega_{01} \equiv (E_1 - E_0)/\hbar$.[44]

$$\begin{aligned} \frac{\partial}{\partial \mathrm{t}} c_1(\mathrm{t}) &= +\frac{i}{\hbar} c_0(t) e^{-i\omega_{01}t} \langle 1|\hat{\mu}|0\rangle E(t) \\ \frac{\partial}{\partial \mathrm{t}} c_0(\mathrm{t}) &= +\frac{i}{\hbar} c_1(t) e^{+i\omega_{01}t} \langle 0|\hat{\mu}|1\rangle E(t) \end{aligned} \tag{2.19}$$

The expressions for the change of the coefficients over time depend on the transition dipole moments $\langle 1|\hat{\mu}|0\rangle$ and $\langle 0|\hat{\mu}|1\rangle$. The transition dipole moment is introduced in equation (2.8) and written here in the bra-ket notation. The coefficients can also be used to write a density matrix ρ, where the coefficients are related to the elements of the matrix.[44]

$$\rho = \begin{pmatrix} \rho_{00} & \rho_{01} \\ \rho_{10} & \rho_{11} \end{pmatrix} \tag{2.20}$$

In the density matrix, the diagonal elements ρ_{00} and ρ_{11} are populations, while the off-diagonal elements ρ_{01} and ρ_{10} correspond to coherences. Ultimately it is the coherences which result in a signal, as they are emitting the electrical field $E_{\mathrm{Sig}}(t)$, as they are oscillating with the frequency of ω_{01}. This oscillation, however, is damped, with a homogenous dephasing time T_2. Therefore, the off-diagonal elements can be written as the following.[44]

$$\begin{aligned} \rho_{01}(t) &= -c_0 c_1 e^{+i\omega_{01}t} e^{-t/T_2} \\ \rho_{10}(t) &= i\, c_0 c_1 e^{-i\omega_{01}t} e^{-t/T_2} \end{aligned} \tag{2.21}$$

There is not only a time dependence in the coherences, but also in the populations. The population of the excited state $|1\rangle$, which corresponds to the density matrix element ρ_{11} decays with a time constant T_1 back to the vibrational ground state ρ_{00}.[44]

$$\begin{aligned} \rho_{11}(t) &= \rho_{11}(0) e^{-t/T_1} \\ \rho_{00} &= 1 - \rho_{11}(t) \end{aligned} \tag{2.22}$$

However, the homogeneous dephasing T_2 and the population relaxation T_1 are not independent of each other. The homogeneous dephasing time contains the population relaxation as well as a pure dephasing time T_2^*, which is due to environment fluctuations.[44]

$$\frac{1}{T_2} = \frac{1}{2\,T_1} + \frac{1}{T_2^*} \tag{2.23}$$

In order to probe the coherences and population relaxations, non-linear spectroscopy is used.

2.4 Pump-probe infrared spectroscopy

In the case of transient IR spectroscopy, the coherences of the first vibrationally excited state and the ground state as well as of the first and the second vibrationally excited state are usually observed. Further, the population relaxation from the first vibrationally excited state can be monitored. Experimentally this is done by exciting (pumping) a molecular vibration with a short IR pump pulse. At ambient temperature the vibrational ground state is populated (Figure 2.2a). Therefore, upon the resonant interaction with the pump pulse (i.e. two interactions of the electric field with the sample), a population in the first vibrationally excited state is created (Figure 2.2b). This population of the excited state decays in time. A weak probe pulse can now probe the population of the excitation as function of delay time τ and the following relaxation back to the ground state. Usually, the data is visualized as a transient spectrum, which compares a pumped with an unpumped spectrum. The resulting transmission difference between the pumped and the unpumped case is determined as a function of the probe frequency. The transient signal $\Delta\alpha$ is calculated[45] by the following expression.[34,40,43,44,46,47]

$$\Delta\alpha = -\ln\left(\frac{T(\omega)}{T_0(\omega)}\right) \tag{2.24}$$

Here, the bleach in the transient signal has a negative sign, since more light is transmitted when the system is pumped $T(\omega)$ compared to the unpumped $T_0(\omega)$ system. An excited state absorption (ESA) on the other hand has a positive transient signal (Figure 2.2c), as more light is absorbed in the pumped case, compared to the unpumped. In case of an anharmonic oscillator, the different transitions (bleach and ESA) from the first vibrational state have different transition frequencies, giving rise to two transient signals at different frequencies. The ESA is shifted to lower frequencies compared to the bleach signal, as the $|1\rangle$ to $|2\rangle$ transition requires less energy than the $|1\rangle$ to $|0\rangle$ transition.[34,40,43,46,47]

By changing the path length of the pump pulse with a delay stage, the delay time between the pump and the probe pulse can be altered with an accuracy in the range of tens of femtoseconds. The time at which the pump and probe pulse overlap is called time zero. While this method has a good time and probe frequency resolution, it only allows for

studying the response of the system upon a broadband excitation. In order to also study vibrational coupling and line-shapes, two-dimensional infrared (2D-IR) spectroscopy needs to be applied.[34,40,43,46,48]

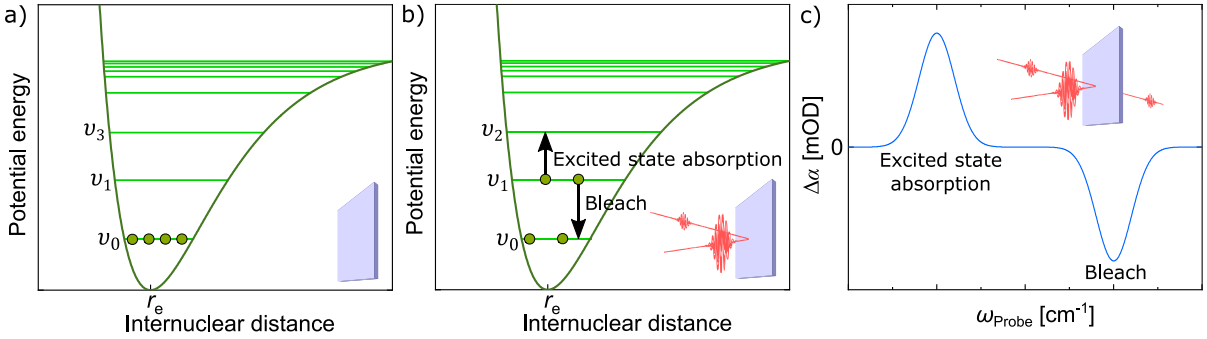

Figure 2.2 shows the basics of pump-probe spectroscopy. In a) the anharmonic potential in the vibrational ground state is shown. After interaction with a pump pulse, the first vibrationally excited state is partially populated b). The interaction with the weaker probe pulse can now either result in excited state absorption or bleach. In c) the resulting spectra showing the modulation as function of frequency is shown. The insets in a), b), and c) show a schematic of the pump and probe pulse interacting with the sample.

2.5 Two-dimensional infrared spectroscopy

The advantage of 2D-IR spectroscopy is the additional resolution along the pump frequency. This allows to study the response of the system, and thus the correlation amongst the vibrational modes when such modes are selectively excited. Thus, the gained resolution along the pump frequency axis can be envisioned as a collection of several pump-probe scans, with a narrow frequency pump, at different pump frequencies. For each of the narrow pump frequencies, the whole probe bandwidth is monitored. By variation of the delay time between the pump and the probe pulse, the response of the system upon excitation at selected pump frequencies can be studied. The spectrum is divided by a diagonal, at which the pump and the probe frequency are equal. Peaks on the diagonal correspond to the peaks which are caused by excitation at their resonance frequency.[44,47,48]

There are two ways to resolve the pump frequency in a 2D-IR spectrum. One is measuring the pump axis in the frequency-domain, the other is measuring it in the time-domain. In the frequency-domain case a scan over all excitation frequencies with excitation pulses, narrow in frequency, is performed. Whenever an excitation frequency is equal to a resonance frequency of the oscillator, the oscillator is excited, and a signal is detected. In the case of time-domain experiments, pulses, which are short in time but broad in frequency, are used. Here, all resonance frequencies of the sample are contained in the excitation pulse. The detected response will be a linear superposition of all the excited frequencies. A simple approach to resolve the linear superposition of the excited frequencies is to change the pump spectrum periodically, in order to change the excited frequencies periodically. This is done by creating several narrow, equally spaced pump pulses, which form a ‘comb’ of pump frequencies. When the spacing between the narrow

pulses is changed, it corresponds to a change in the period of a sinusoidal wave. This can be done experimentally by applying two temporally separated femtosecond pulses in time-domain, which correspond to a sinusoidal frequency-domain spectrum. The period of the sinusoidal spectrum in the frequency-domain is inversely proportional to the time delay of the two fs pulses. A scan over the time delays of the fs pulses, therefore, corresponds to bringing always different sets of frequencies in resonance. A Fourier transformation can be used to transform the time-domain response in a frequency-domain spectrum, in which the excited oscillators give rise to a signal.[44]

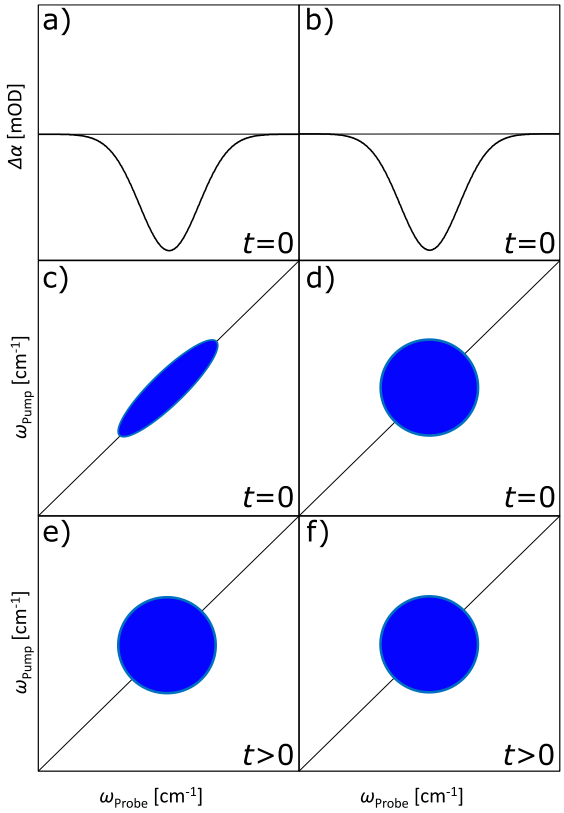

Figure 2.3 is a schematic showing the differences between an inhomogeneously a) ,c) ,e) and a homogeneously c), d), f) broadened peak. In both cases, a bleach signal is shown. The one-dimensional transient spectra of the homogeneously a) and the inhomogeneously broadened spectra b) cannot be distinguished. This, however, is possible in the corresponding 2D-IR spectra. Here, at early times $\boldsymbol{t = 0}$, the homogeneously broadened peak is elongated along the diagonal c), while the homogeneously broadened peak already has a circular shape d). At later delay times, both peaks become circular in shape again e), f).

Even for simple, on-diagonal peaks, 2D-IR spectroscopy has an advantage over one-dimensional spectroscopy, as it provides insights on the broadening of the peak and on spectral diffusion of the studied oscillator. If a system consists of only one kind of oscillators, which all have the same local environment, a circular peak is observed in the 2D-IR spectrum at early delay times (Figure 2.3d). However, if one kind of oscillator is present in various local environments, the frequency of each oscillator is slightly altered. In that case, the observed band is not homogeneous but consists of several bands, representing the populations in different environments. Here, at early delay times, the

peak in the 2D-spectrum is inhomogeneously broadened, which means elongated along the diagonal (Figure 2.3c). At longer delay times the peak becomes round (Figure 2.3e). This effect is called spectral diffusion and is caused by the excited oscillators moving into different local environments, which results in a shift in their resonance frequency.[44,47–49]

Similar to the one-dimensional transient IR spectra, the excited state absorption (ESA) can also be observed in 2D-IR spectra. The ESA appears at the same pump frequency as the bleach peak, but is shifted to lower probe frequencies due to the anharmonicity of the energy potential (Figure 2.4a).[44,47,48]

Another advantage of 2D-IR spectroscopy over one-dimensional transient IR spectroscopy is the fact that crosspeaks between two on-diagonal peaks can be observed (Figure 2.4b). When one oscillator (A) is excited by a pump pulse at its resonance frequency ω_A, a peak at a probe frequency equal to its resonance frequency ω_A is observed. A crosspeak appears, when this excitation at the resonance frequency of one oscillator (A), ω_A, results in the appearance of a second peak at the resonance frequency of another oscillator (B), ω_B. This crosspeak is located at the probe frequency of the resonance of the second oscillator ω_B, while it is at the same pump frequency as the resonance of the first oscillator ω_A. The presence of crosspeaks may have various origins. When two oscillators are coupled, their crosspeaks in the 2D spectrum are already visible at time zero. If the crosspeaks appear with some time delay, they might result from energy transfer or chemical exchange. During energy transfer, one oscillator loses energy while another oscillator in close proximity and with a different resonance frequency receives energy. In the case of chemical exchange, the environment of the excited oscillator changes (e.g. change from bound to unbound) which results in a change in the resonance energy.[44,47–50]

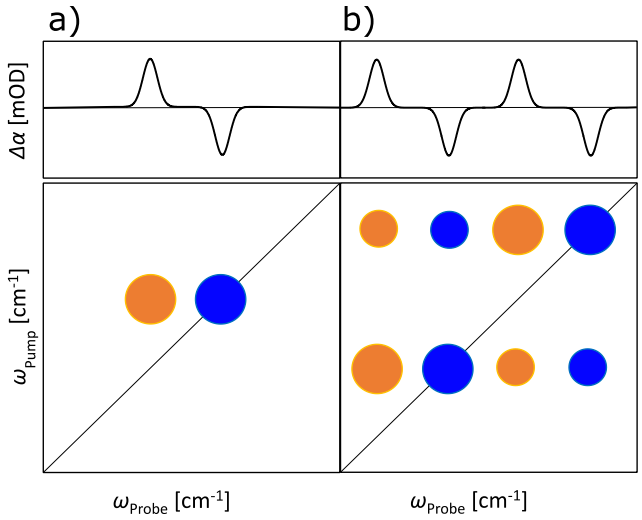

Figure 2.4 a) shows the bleach (negative peak, blue circle) at higher and the excited state absorption (ESA, positive peak, orange circle) at lower probe frequencies. Bleach and ESA are both generated by the same pump frequency, which is resonant with the transition from the vibrational ground state to the first vibrationally excited state. In b) two on-diagonal peaks (big, blue circles), their corresponding excited state absorptions (big, orange circles) and the off-diagonal crosspeaks (small circles) are shown. The existence of crosspeaks cannot be detected in the one-dimensional transient spectra, but only in the 2D-IR spectrum.

2.6 Dielectric relaxation spectroscopy

In order to study the dynamics of dipolar species, dielectric relaxation spectroscopy (DRS) is applied. It allows studying dipoles, such as ion-pairs, the time scale of their relaxation processes, and retrieving the permittivity of the solution. The permittivity of a dielectric can be measured by applying an electrical field.[51] The resulting polarization $\vec{P}$ of non-conducting molecular liquids was previously discussed (see chapter 2.2). It is given by the permittivity $\hat{\varepsilon}$, the vacuum permittivity ε_0 and the field strength $\vec{E}$.[52]

$$\vec{P} = \varepsilon_0(\hat{\varepsilon} - 1)\vec{E} \tag{2.25}$$

$\vec{P}$ can be macroscopically described as the sum of the orientational (or dipolar) polarization $\vec{P}_\mu$, arising from the alignment of permanent dipoles, and the induced polarization $\vec{P}_\alpha$. The latter describes the relative displacement of atoms or electrons under the influence of the applied electric field (e.g., the displacement of electrons relative to the positively charged nucleus).[51]

$$\vec{P} = \vec{P}_\alpha + \vec{P}_\mu \tag{2.26}$$

The induced polarization depends on the number density $\mathcal{N}$, the polarizability α_k and the average electric field strength $\left(\vec{E}\right)_k$ over all k species.[51] The corresponding transitions, representing the intramolecular charge separation, appear as well-defined resonances at frequencies above the microwave frequency range. Therefore, the contribution of the induced polarization in the microwave frequency range is independent of frequency.[52]

$$\vec{P}_\alpha = \sum_k \mathcal{N}_k \alpha_k \left(\vec{E}\right)_k \tag{2.27}$$

The orientational polarization and its dynamics, is the type of polarization studied in this thesis by means of dielectric relaxation spectroscopy.[52] The orientational polarization is described by the alignment of the dipolar species k with a dipole moment $\vec{\mu}_k$ to the external field. The fact that more aligned dipolar species result in more orientational polarization is taken into account by the dependence on the number density $\mathcal{N}$.[51]

$$\vec{P}_\mu = \sum_k \mathcal{N}_k \langle \vec{\mu}_k \rangle \tag{2.28}$$

As orientational and induced polarizations occur on different time scales, they can be separated. To do that, the permittivity at infinite frequencies ε_∞ is introduced. Here ε_∞ contains all components that contribute to the induced polarization.[53] The contribution at lower frequencies, e.g. the orientational polarization can, therefore, be described using the following equation for systems in equilibrium.[52,54]

$$\vec{P}_\mu = \varepsilon_0(\hat{\varepsilon} - \varepsilon_\infty)\vec{E} \tag{2.29}$$

The contributions at higher frequencies, which are described by the induced polarization, are given by the following equation.[52]

$$\vec{P}_\alpha = \varepsilon_0(\varepsilon_\infty - 1)\vec{E} \tag{2.30}$$

2.6.1 Step response function

The dynamics of a system can be studied by measuring the orientational relaxation times.[51] These can be measured via the changes in the orientational polarization with time or frequency. In the following, the response of the polarization after turning off the applied electric field is discussed. Turning the field off results in an instantaneous change in the electric field (a field jump) at time $t = 0$. Given the difference in the characteristic time scales/frequencies, the induced polarization $\vec{P}_\alpha$ responds to the field jump quasi-instantaneously, whereas the orientational polarization $\vec{P}_\mu$ changes in a slower manner. This time dependent change of the orientational polarization $\vec{P}_\mu(t)$ as response to the field jump can be described with a step response function $F_P(t)$.[52]

$$\vec{P}_\mu(t) = \vec{P}_\mu(0) \cdot F_P(t) \tag{2.31}$$

Here, $\vec{P}_\mu(0)$ is the orientational polarization at the time of the field jump.[52] The step response function is defined in such a way that the induced polarization decreases with the following boundary conditions $F_P(0) = 1$ and $F_P(\infty) = 0$.[51] Therefore, the step response function is given by the following autocorrelation function:[52,55]

$$F_P(t) = \frac{\langle \vec{P}_\mu(0) \cdot \vec{P}_\mu(t) \rangle}{\langle \vec{P}_\mu(0) \cdot \vec{P}_\mu(0) \rangle} \tag{2.32}$$

Equations (2.25) and (2.29) show the dependence of the polarization on a static electric field. Now the response of the polarization to a harmonically oscillating field $\vec{E}(\mathrm{t})$, defined in the following equation, is discussed. It depends on the time t and the angular frequency ω ($\omega = 2\pi\nu$), where ν is the field frequency.[56]

$$\vec{E}(t) = \vec{E}_0 \exp(-\mathrm{i}\omega t) \tag{2.33}$$

The frequency-dependent orientational polarization at any time t can be expressed by substituting eq. (2.33) in the expression for the orientational polarization, eq. (2.29), and Laplace transforming the response function as shown below.[56]

$$\vec{P}_\mu(\omega, t) = \varepsilon_0(\varepsilon - \varepsilon_\infty)\, \vec{E}(t)\, \mathcal{L}_{i\omega}[f_P(t')] \tag{2.34}$$

Here, $\mathcal{L}_{i\omega}[f_P(t')]$ is the Laplace transformed pulse response function for the orientational polarization, with[51,55,56]

$$\int_0^\infty \exp(-\mathrm{i}\omega t')\ f_P(t')\, \mathrm{d}t' = \mathcal{L}_{i\omega}[f_P(t')] \tag{2.35}$$

The pulse response function $f_P(t')$ of the orientational polarization is the negative time-derivative of the step response function defined in equation (2.32) above.[51,55,56]

$$f_P(t) = -\frac{\partial F_P(t)}{\partial t} \tag{2.36}$$

By rearranging eq. (2.29), for $\hat{\varepsilon}$ and introducing eq. (2.34) in the integral form, as expression for the polarization, the following equation[57] is derived:

$$\hat{\varepsilon}(\omega) = \varepsilon_\infty + \frac{\vec{P}}{\vec{E}\,\varepsilon_0} = \varepsilon_\infty + (\varepsilon - \varepsilon_\infty) \int_0^\infty \exp(-\mathrm{i}\omega t)\ f_P(t)\, \mathrm{d}t \tag{2.37}$$

This expression can now be used to describe relaxation processes.

2.6.2 The Debye equation

A very simple approach to describe the time-dependent dielectric behaviour of a system is assuming a direct proportionality of the rate of change of the polarization to its actual value.[57]

$$\frac{\partial \vec{P}(t)}{\partial t} = -\frac{1}{\tau}\vec{P}(t) \tag{2.38}$$

A relaxation describes the process of the polarization following the change in the field with some delay. The orientational relaxation time is the time in which the polarization P is reduced by $1/e \cdot P(0)$. For liquids at room temperature, the orientational relaxation times are usually in the nano- to picosecond range, corresponding to microwave frequencies. The behaviour described in the equation (2.38) above can be fulfilled by an exponential decay of the correlation function $F_P(t)$.[51,57]

$$F_P(t) = \exp(-\frac{t}{\tau}) \tag{2.39}$$

Therefore, the corresponding pulse response function is written as:

$$f_P(t) = -\frac{1}{\tau}\exp(-\frac{t}{\tau}) \tag{2.40}$$

Applying the Laplace transformation converts the pulse response function from the time-domain to the frequency-domain.[56]

$$\mathcal{L}_{i\omega}[f_P(t')] = \frac{1}{1 + \mathrm{i}\omega t} \tag{2.41}$$

Now the expression (eq. (2.41)) can be used, to apply the assumption of an exponential decay of the correlation function (2.39) to eq. (2.37). This results in the Debye equation in its complex representation, where ε_S is the static permittivity.[56]

$$\hat{\varepsilon}(\omega) = \varepsilon_\infty + \frac{(\varepsilon_S - \varepsilon_\infty)}{1 + \mathrm{i}\omega t} \tag{2.42}$$

The complex permittivity $\hat{\varepsilon}$, consists of a real ε' and an imaginary ε'' component.[55]

$$\hat{\varepsilon} = \varepsilon' - \mathrm{i}\varepsilon'' \tag{2.43}$$

Therefore, eq. (2.42) can also be separated into its real and imaginary parts. The corresponding real and imaginary expressions are given below.[56]

$$\varepsilon' = \varepsilon_\infty + \frac{(\varepsilon_S - \varepsilon_\infty)}{1 + \omega^2 t^2} \tag{2.44}$$

$$\varepsilon'' = \frac{(\varepsilon_S - \varepsilon_\infty)\omega t}{1 + \omega^2 t^2} \tag{2.45}$$

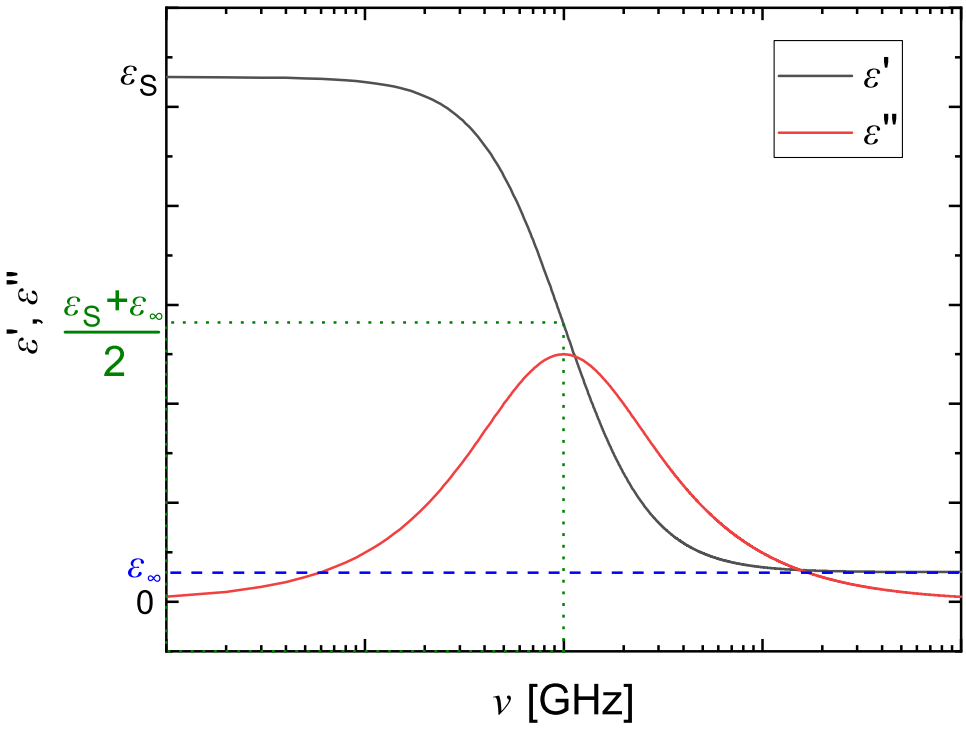

Figure 2.5 shows the permittivity as a function of frequency of a typical Debye relaxation. The real part of the permittivity ε' is decaying from the static permittivity ε_S to ε_∞. The amplitude S of the decay is the dielectric strength, here it is the difference of $\varepsilon_S - \varepsilon_\infty$. The frequency at the inflection point of the ε' decay corresponds to the relaxation time ($\tau = 1/2\pi\nu$). At this frequency, the imaginary part of the permittivity ε'' reaches its maximum.

The real and imaginary part of the Debye function is shown in Figure 2.5 above. The relaxation time defines the corresponding frequency, where the imaginary part peaks and the real part has its inflection point. The real part of the permittivity decays with frequency from the initial static permittivity ε_S to the infinity frequency permittivity ε_∞. The inflection point of the curve is given by the relaxation time. The relaxation time corresponds to the reorientation time of the molecular dipoles investigated.[52,57]

2.6.3 The Cavell equation

To extract quantitative information from the DRS spectra, the Cavell equation can be used. It was developed by Cavell[58] and relates the amplitude S_j of the species j to the concentration c and the effective dipole moment $\mu_{\mathrm{eff},j}$. The amplitude S_j is the difference between the low frequency and the high frequency permittivity value, also referred to as dielectric strength.[59]

$$\frac{2\varepsilon_S' + 1}{\varepsilon_S'} \cdot S_j = \frac{N_\mathrm{A} c}{k_\mathrm{B} T \varepsilon_0} \cdot \mu_{\mathrm{eff},j}^2 \tag{2.46}$$

Here, ε_0 is the vacuum permittivity, N_A the Avogadro constant, k_B the Boltzmann constant, and T the temperature. The effective dipole moment μ_eff is related to the dipole moment of an isolated molecule μ by the following relationship.[59]

$$\mu_\mathrm{eff} = \sqrt{g} \cdot \mu_\mathrm{ap} \tag{2.47}$$

Here, g is the correlation factor describing the orientational dipole-dipole correlation, and is assumed to be 1 for nonpolar solvents at low to moderate concentrations[54]. Therefore, in this thesis, the effective dipole moment μ_eff is equal to the measured apparent dipole moment μ_ap.[57,59,60] Thus using the Cavell equation a relation between the spectral amplitude and concentration can be established, which allows quantifying the dipolar species present in solution.

2.7 Nuclear magnetic resonance spectroscopy

Nuclear magnetic resonance (NMR) spectroscopy is a technique, which probes the spin of nuclei in an external magnetic field. It takes advantage of the fact that nuclei in different electronic environments are differently shielded from the external magnetic field. This allows one to draw conclusions about the electron density around the corresponding nuclei. By taking the different electron densities of different chemical bonds into account,

it ultimately enables the determination of the chemical structure of an observed molecule.[1,61] The basic principles of NMR spectroscopy are explained in the following paragraphs. The angular momentum $\vec{L}$ (spin) of a nucleus is quantized. It can be described by the following equation:[61]

$$|\vec{L}| = \frac{h}{2\pi} m \tag{2.48}$$

$\vec{L}$ depends on the Planck constant h and the magnetic quantum number m. For a proton, the magnetic quantum numbers are ±½.[61] All nuclei that have an angular momentum also have a magnetic moment μ_{M}.[62]

$$\vec{\mu}_{\mathrm{M}} = \gamma \vec{L} \tag{2.49}$$

The strength of the magnetic moment depends on the gyromagnetic ratio γ, which is a nuclei-specific constant.[61] When for example a proton is placed in an external static magnetic field, some nuclei spins will align parallel to the external field, while some will align in the opposite direction. As a result, the two degenerate spin states split into a high and a low energy state, the so-called Zeeman-effect.[1] The potential energies of those states are defined by the static magnetic field $\vec{H}_0$ and the magnetic dipole of the nuclei.[61]

$$E = \vec{\mu}_{\mathrm{M}} \vec{H}_0 \tag{2.50}$$

This can be rewritten, by taking equations (2.48) and (2.49) into account.[61]

$$E = \frac{\gamma h \vec{H}_0}{2\pi} m \tag{2.51}$$

In the case of the proton, where m = ±½, the energy difference ΔE between the high and the low energy state is given as:[61]

$$\Delta E = \frac{\gamma h \vec{H}_0}{2\pi} \tag{2.52}$$

Based on the energy difference, the population of the high and the low energy states differ. The ratio of the number of nuclei in the spin state α (N_α) to the number of nuclei in the spin state β (N_β) follows the Boltzmann distribution.[61]

$$\frac{N_\alpha}{N_\beta} = e^{-\Delta E/k_B T} \tag{2.53}$$

Here, the distribution of the populations depends on the temperature (T), the Boltzmann constant (k_B) and the energy difference between both states (ΔE). As a result of the small energy difference between the states, there is only a very small population difference ($N_\alpha - N_\beta$).[1,61] For example, the resulting population difference, for a sample containing $N = 1$ million protons ($\gamma = 2.678 \cdot 10^8 \ \frac{1}{\mathrm{T\,s}}$) at $\vec{H}_0 = 7$ T at 20 °C, is 25.

$$N_\alpha - N_\beta = \frac{N\gamma h\vec{H}_0}{k_B T} \tag{2.54}$$

A stronger magnetic field results in a stronger splitting of the states and thus increases the energy difference. A transition frequency between both states is governed by the following relationship:[62]

$$\nu_0 = \frac{\omega_0}{2\pi} = -\frac{\gamma\vec{H}_0}{2\pi} \tag{2.55}$$

Here ν_0 is the frequency of the transition, which is given by the angular velocity ω_0, or the gyromagnetic ratio γ and the static magnetic field $\vec{H}_0$.[62] This indicates that an electromagnetic wave with the frequency of ν_0 is required to excite the nucleus from the lower in the higher spin state. Therefore, the resonance frequency of the transition depends on the magnetic field.[61] The resonance frequency contains information about the environment of the nuclei. The electron density of the environment surrounding a nucleus affects the magnetic field at the nucleus, as the moving electrons introduce a secondary magnetic field. The secondary magnetic field shields the nucleus from the external magnetic field and thus changes the resonance frequency of the nucleus. However, as this quantity depends on the magnetic field strength of the spectrometer used, the chemical shift δ as a setup independent scale for the shielding was introduced.[63] This scale is normalized to tetramethylsilane (TMS), the standard substance for ^{1}H-NMR, having a peak at δ = 0 ppm. The chemical shift of this substance is defined to be at a chemical shift of 0 ppm (parts per million). Therefore, the chemical shift is defined as the difference between the frequency of the sample ν_{Sample} and that of the TMS ν_{TMS}, as shown in equation (2.56).[1,63]

$$\delta = \frac{\nu_{Sample} - \nu_{TMS}}{\nu_{TMS}} \cdot 10^6 \qquad (2.56)$$

In this thesis, ^{1}H-NMR is used to probe the electronic environment of protons. Different Brønsted acid catalyst concentrations result in a variation in the observed chemical shift. However, two-dimensional NMR techniques, which will be briefly discussed in the following, are also applied.

In order to observe intermolecular coupling of nuclear spins, the nuclear Overhauser effect (NOE) can be exploited. In two-dimensional NOE spectroscopy (NOESY), cross-peak originate from dipolar ('through space') coupling of spatially close nuclear spins. Thus, the spatial proximity of nuclei can be measured, as the intensity of the crosspeaks scales as $1/r_{\mathrm{n}}^6$ on the internuclear distance r_{n}.[1,64] Usually, this effect is used to study proton-proton distances.[65] In this thesis, however, the NOE is used to observe the correlation of protons with phosphorous nuclei. This two-dimensional spectroscopy, called heteronuclear Overhauser effect spectroscopy (HOESY), observes the magnetization exchange from the proton to the phosphorous nuclei of DPP/phosphate.[66] The intensity of the crosspeaks is correlated with the distance between both nuclei.[65]

In addition to that, it is also possible to correlate an NMR spectrum to a distribution of diffusion coefficients using diffusion-ordered spectroscopy (DOSY). Here, several NMRs following a magnetic field gradient, are measured. Those field gradients are correlated to diffusion coefficients. The diffusion coefficients corresponding to the field gradients are calculated and usually plotted as a 2D-plot. In the 2D-plot the chemical shift is the x-axis and the diffusion coefficient is plotted on the y-axis. This two-dimensional method divides NMR spectra of several components in sets of components with the same diffusion coefficients. DOSY can be used to separate the NMR spectra of molecules with different diffusion coefficients and therefore enable the analysis of otherwise very congested one-dimensional spectra.[67] In this thesis it is used to confirm the formation of aggregates of different sizes (ion-pairs and trimers).

3 Methods

This chapter introduces the equipment used for the experiments presented in this thesis. First for dielectric relaxation and nuclear magnetic resonance spectroscopies, later for the infrared spectroscopies.

3.1 Dielectric relaxation spectrometer

To study the formation of dipolar aggregates in solution, I use DRS,[57,68] which measures the polarization of these samples in an externally applied oscillating electric field with field frequency, ν. The induced polarization is experimentally measured and can be expressed in terms of the complex permittivity $\hat{\varepsilon}(\nu)$, see eq. (2.43). Here, the real part, ε', is the frequency dependent permittivity and the imaginary part, ε'', represents the dielectric loss (i.e. absorption).[57,69]

To measure the permittivity of a sample, a Vector Network Analyser (VNA) is used. Here, the VNA is used to create and detect reflected waves in the microwave range, which are sent to the sample through a coaxial cable. At the end of the coaxial cable, there is a probe head which is in contact with the sample.[70] The reflected signal is analysed and it yields the parameter $\hat{S}_{11}$ of the scattering matrix, which is related to the normalized impedance $\hat{Y}$ of the sample at the end of the coaxial cable. Here, $\hat{Y}$ is normalized to the impedance of the coaxial cable (50 Ω).[71]

$$\hat{S}_{11}(\omega) = \frac{1 - \hat{Y}(\omega)}{1 + \hat{Y}(\omega)} \tag{3.1}$$

The impedance step at the interface between the coaxial cable and the sample dominates the scattering parameter. For probe heads based on the open-ended probe geometry, the normalized impedance can be calculated using the following expression.[71,72]

$$\begin{aligned} \hat{Y} \; = & \frac{\hat{k}_m^2(\omega)}{\pi \hat{k}_c(\omega) \ln\left(\frac{D}{d}\right)} \times \\ & \left(\mathrm{i} \left(\frac{I_1}{0!} - \frac{\hat{k}_m^2(\omega) I_3}{2!} + \frac{\hat{k}_m^4(\omega) I_5}{4!} - \cdots \right) \right. \\ & \left. + \left(\frac{\hat{k}_m(\omega) I_2}{1!} - \frac{\hat{k}_m^3(\omega) I_4}{3!} + \frac{\hat{k}_m^5(\omega) I_6}{5!} - \cdots \right) \right) \end{aligned} \tag{3.2}$$

The normalized impedance $\hat{Y}$ is a function of the propagation constant $\hat{k}_m(\omega)$ of the sample at the frequency ω. Further, the normalized impedance depends on the propagation constant in the probe head $\hat{k}_c(\omega)$, the inside diameter of the outer conductor D, and the outside diameter of the inner conductor d. Both propagation constants are functions of the vacuum permeability μ_0, the respective complex permittivity of the sample $\hat{\varepsilon}$, the probe head $\hat{\varepsilon}_c$, and the vacuum permittivity ε_0.[71,72]

$$\hat{k}_m(\omega) = \omega\sqrt{\hat{\varepsilon}(\omega)\varepsilon_0\mu_0} \tag{3.3}$$

$$\hat{k}_c(\omega) = \omega\sqrt{\hat{\varepsilon}_c\varepsilon_0\mu_0} \tag{3.4}$$

The coefficients I_n (for n ranging from 1 up to 40 for the calculations used in this thesis), are resulting from a Taylor expansion of the normalized impedance (see eq. (3.2)) and have been calculated by numerical integration of the following equation, for the given geometry of the probe head (r, θ).[71,72]

$$I'_n = \int_d^D \int_d^D \int_0^\pi \left(\sqrt{r^2 + r'^2 - 2rr'\cos(\theta)}\right)^{n-2} \cos(\theta)\, d\theta\, dr\, dr' \tag{3.5}$$

The optimization of I'_n is based on measurements of reference samples with known permittivities.[71,72] In order to measure unknown samples using the VNA, the instrument has to be calibrated. This is done by relating the measured relative scattering parameters $S_{11}^m(\omega)$ to the scattering parameters at the interface between sample and coaxial probe head $S_{11}^a(\omega)$. For that purpose, three reference samples with known scattering parameters are measured for each measurement of an unknown sample. Thus, the errors in directivity $e_d(\omega)$, frequency response $e_r(\omega)$ and source match $e_s(\omega)$ can be derived for each reference sample at every frequency. Based on the errors derived from calibration and the scattering parameter of the unknown sample the complex permittivity $\hat{\varepsilon}$ of the sample can be determined.[71,72]

$$S_{11}^m(\omega) = e_d(\omega) + \frac{e_r(\omega)S_{11}^a(\omega)}{1 - e_s(\omega)S_{11}^a(\omega)} \tag{3.6}$$

In this thesis, an Anritsu MS4647A Vector Network Analyser was used. The measured permittivities were measured at ambient temperature (295 ± 2 K) and investigated over the frequency range from 10 MHz up to 125 GHz. In order to cover such a broad frequency range, three experimental reflectometer geometries were used. High frequencies from

~50-110 GHz were measured using a coaxial reflectometer, which is based on an external frequency converter module. In this thesis the Anritsu 3744A mmW module with an open-ended coaxial probe was used, which was based on a 1 mm coaxial connector.[70,73,74] The intermediate frequencies were covered using an open-ended coaxial cell with 1.85 mm connectors.[71,72,74] The actual frequency ranges are adjusted for each spectrum in such a way, that the noise is minimized. A cut-off type coaxial cell[75,76] is used for the low frequencies from ~10-1000 MHz. In the cut-off type coaxial cell the measured impedance is related to the permittivity by the following expression instead of eq. (3.2). Here Z_0 is the characteristic impedance of the coaxial cable, c_0 is the speed of light in vacuum and l is the length of the cut-off cell.[75]

$$\hat{Y} = \frac{1}{Z_0}\sqrt{\hat{\varepsilon}(\omega)}\tanh\left(\frac{i\omega}{c_0}\sqrt{\hat{\varepsilon}(\omega)}l\right) \tag{3.7}$$

3.2 Nuclear magnetic resonance spectrometer

To obtain information on the chemical environment of Qu, a set of NMR experiments was performed. ^{1}H-NMR spectra of the solutions were recorded on a Bruker 300, 500, and 850 MHz AVANCE III spectrometer. For selected samples, ^{1}H- and ^{31}P-NMR spectra were recorded, using a 5 mm BBFO z-gradient probe on the 500 MHz Bruker AVANCE III system (TOPSPIN 3.2 software version). The spectra were obtained with π/2-pulse lengths of 14.7 µs for proton (128 number of scans, spectra width 12500 Hz) and 12 µs for ^{31}P and a relaxation delay of 3 s for ^{1}H-NMR and 10 s for ^{31}P-NMR. The proton spectra were referenced using the residual $CDHCl_2$ at 5.37 ppm ($\delta(^{1}H)$). The ^{31}P spectra were referenced using Triphenylphosphine at -6 ppm.

To extract information on the intermolecular interaction between catalyst and substrate, I complemented our analysis with two-dimensional (2D) ^{31}P-^{1}H HOESY[66] (heteronuclear Overhauser enhancement spectroscopy) methods. The spectroscopic widths of the heteronuclear 2D-HOESY experiments were typically 1600 Hz in the detected dimension (F1 (^{1}H: 10000 Hz) and F2 (^{31}P: 1600 Hz)) using a relaxation delay of 2 s. The mixing time for the HOESY experiment was set to 1500 ms. Information on the hydrodynamic size of the molecular aggregates in solution was studied using diffusion ordered NMR spectroscopy (DOSY-NMR). These spectra were recorded using a 5 mm TXI ^{1}H/^{13}C/^{15}N z-gradient probe with a gradient strength of 5.350 G/mm on a Bruker Avance-III 850 NMR Spectrometer. The gradient strength of the probes was calibrated by analysis of a sample of $^{2}H_2O$/$^{1}H_2O$ and compared to the reported diffusion coefficient of $^{2}H_2O$/$^{1}H_2O$ (values taken from Bruker diffusion manual) at 298.3 K. In this work, the gradient was varied using 32 steps from 2 % to 100 % and the diffusion time was set to 40 ms.

3.3 Infrared setups

Fourier transform infrared spectra (FTIR) were measured using a Bruker VERTEX 70 spectrometer with 4 cm^{-1} resolution in transmission geometry. To obtain information on vibrational dynamics I used broadband infrared pump-probe experiments. A schematic of the setup is shown in Figure 3.1. Here an infrared pulse is generated from an 800 nm pulse (~50 fs duration, 1.5 mJ pulse energy, 1 kHz repetition rate) from a Ti:sapphire regenerative amplifier (Spitfire Ace, Spectra-Physics) in an optical parametric amplifier (OPA) together with a non-collinear difference frequency generation stage (TOPAS Prime & NDFG, Light Conversion, Spectra-Physics). The infrared pulse (centred at 2000 cm^{-1}, FWHM ~300 cm^{-1}) excites infrared modes in the sample. The IR (~12 µJ pulse energy and ~100 fs duration) pulse generated in the Topas Prime (GaSe crystal) with non-collinear difference frequency generation (NDFG) is passing through two dichroic and one long-wave pass filter in order to remove any light with shorter wavelength. It is then split between a pump, a probe, and a reference path, with the help of a wedged CaF_2 window. The probe pulse and the reference pulse are the two reflections from the wedged CaF_2 window. The reference path is directly detected after passing the spectrometer. It is used to cancel out pulse to pulse intensity fluctuations. The probe pulse, however, is focused in the sample by a parabolic mirror and re-collimated afterwards. A polarizer, which can be automatically rotated by 90° is used to measure the modulation with parallel ($\Delta\alpha_{||}$) and perpendicular ($\Delta\alpha_{\perp}$) polarization of the probe pulse relative to the pump pulse polarization. Finally, the probe is focused into the spectrograph and detected. Most of the IR energy is used for the pump pulse. In order to detect the pump-induced modulation of the infrared absorption, $\Delta\alpha$, every second IR pulse is blocked by a chopper. Therefore only every second time a probe pulse passes the sample, the sample is pumped. After the sample the pump beam is blocked. The modulation of the infrared absorption, $\Delta\alpha$, is detected with a weak, variably delayed infrared probe pulse as a function of delay time, t. The isotropic (rotation free) modulation, which is sensitive to vibrational population dynamics, is constructed accordingly: $\Delta\alpha_{iso} = (\Delta\alpha_{||} + 2\Delta\alpha_{\perp})/3$. A similar experimental setup is described in the literature.[45] The probe and reference beam are spectrally dispersed with a Triax 180 spectrograph (Horiba, 100 l/mm grating) onto a 2 x 32 pixel mercury cadmium telluride (MCT) detector.

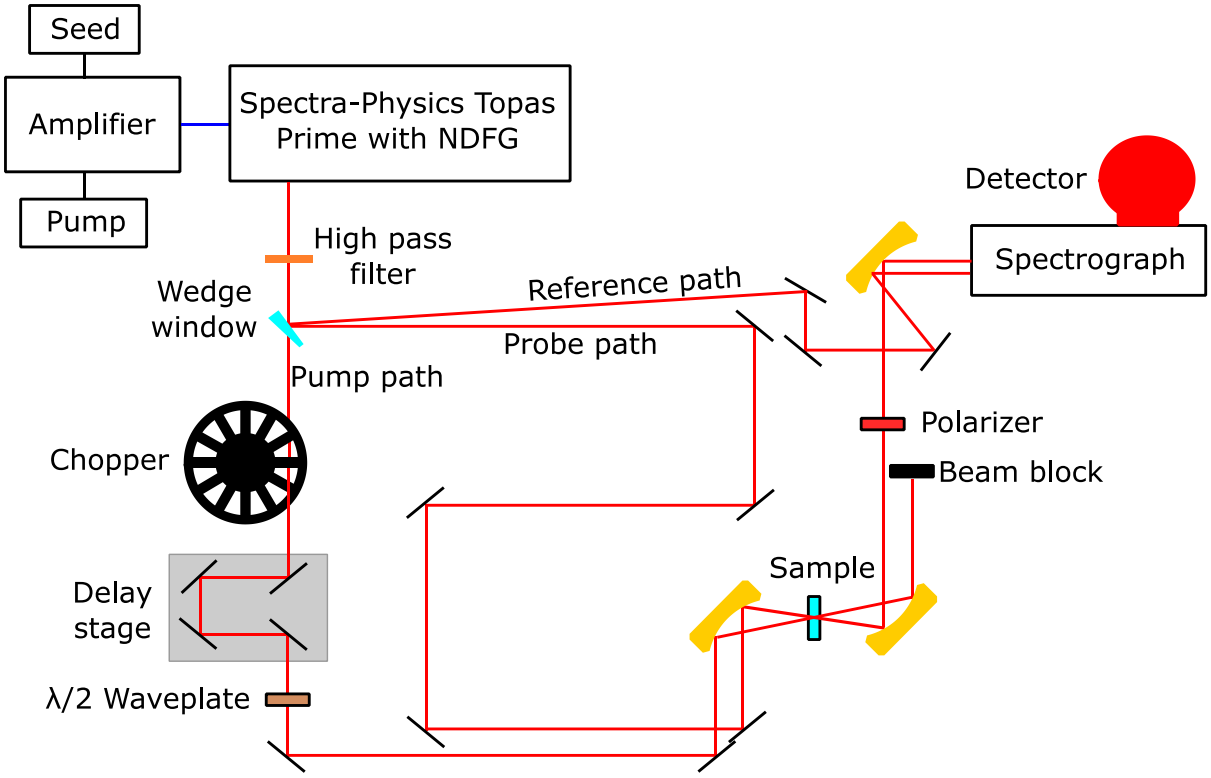

Figure 3.1 shows a schematic of the pump-probe setup. 800 nm LASER radiation is created and amplified. A Spectra-Physics Topas Prime with non-colinear difference frequency generation (NDFG) is used to generate infrared radiation. A chopper is used to block every second pump pulse. The time delay between pump and probe is adjusted by the delay stage in the pump path. Pump and probe are focused on the sample and overlapped in time and space. A MCT detector and a spectrograph are used to detect the probe and reference pulse intensities.

To resolve the spectral modulation for different pump frequencies, I performed two-dimensional infrared (2D-IR) spectroscopy experiments. The setup is schematically shown in Figure 3.2. Here, the sample is excited using two temporally separated pump pulses. Variation of the coherence time (t_1) between the two pump pulses and subsequent Fourier transformation of the transient signals at different probing frequencies provides spectral resolution along the pump axis.[44,48,77–79] The 2D-IR experiment is based on a regenerative amplifier (Astrella, Coherent) providing 800 nm pulses (35 fs pulse duration) at a 1 kHz repetition rate. Pulses with an energy of 2.7 mJ are used to pump an OPA with difference frequency generation to generate IR pulses (pulse energy ~30 µJ) centred at 2000 cm^{-1} with a 150 fs pulse duration. The infrared pulses are guided to a commercial 2D-IR spectrometer (2DQuick-IR, Phasetech Spectroscopy Inc.). Pump pulse pairs are generated using an infrared pulse-shaper, based on spectrally dispersed diffraction from a Ge-based acousto-optic modulator.[80–82] The pump and the probe beams are overlapped and focused into the sample. The probe beam is then detected together with a reference beam, by dispersing both beams (using a SP2156 spectrograph, Princeton instruments, 30 l/mm grating) onto a 128x128 pixel MCT array detector. 2D-IR spectra are recorded as a function of delay time.

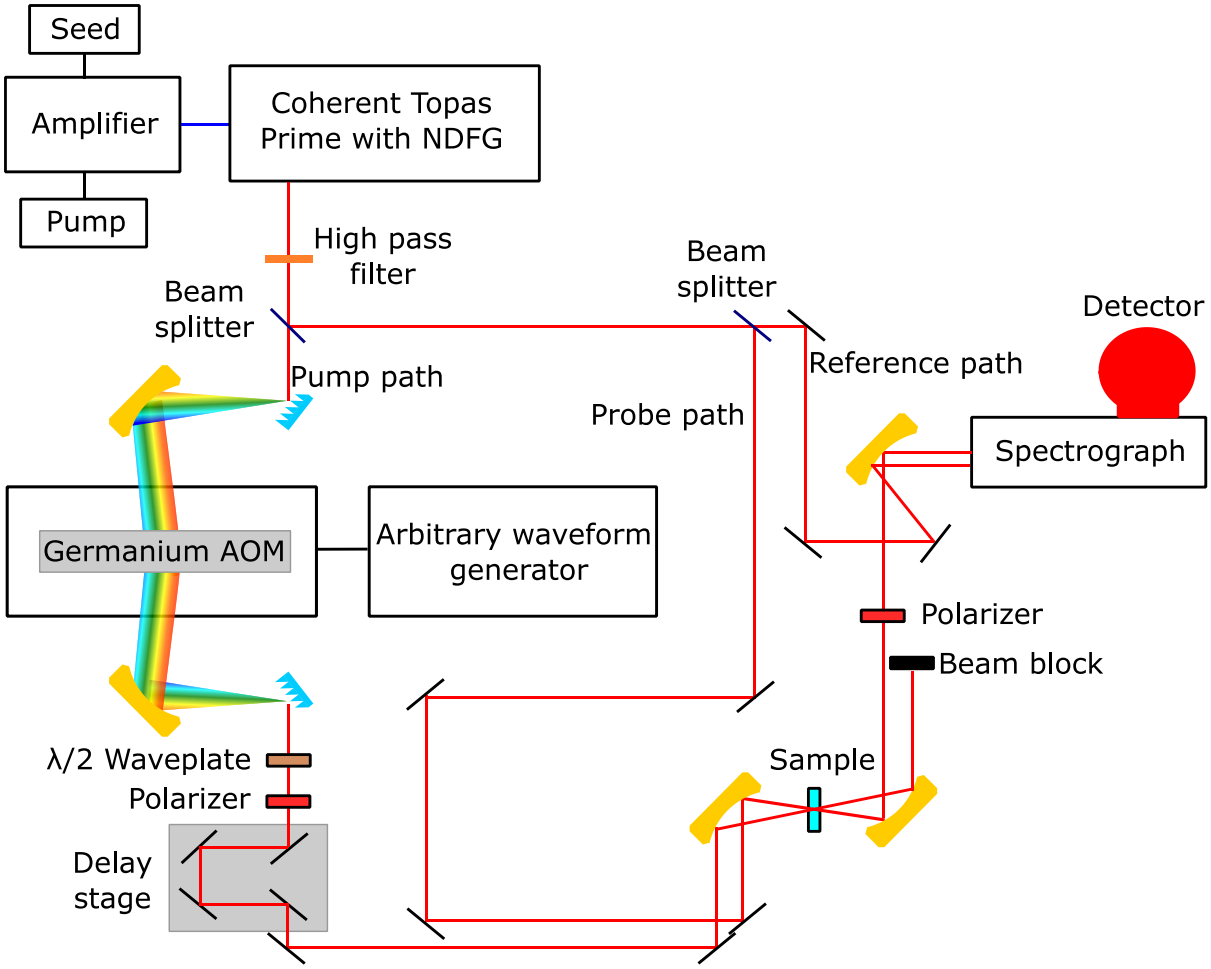

Figure 3.2 shows a schematic of the 2D-IR setup. 800 nm LASER radiation is created and amplified. A Coherent Topas Prime with NDFG is used to generate infrared radiation. The acousto-optic modulator (AOM) is used to shape the pump pulses as desired. A MCT detector and a spectrograph are used to detect the probe and reference spectra.

In order to analyse the data and plot it as a 2D-frequency against frequency plot, a Fourier transformation has to be applied on the free induction decay (FID) (see Figure 3.3) of the third-order response, which is measured in time-domain.[44,83] The information along the probe frequency axis is measured in the frequency-domain. All information about the pump-frequency dependence is detected in the time-domain and can be Fourier transformed to the frequency-domain (see eq. (3.8)).[44,83]

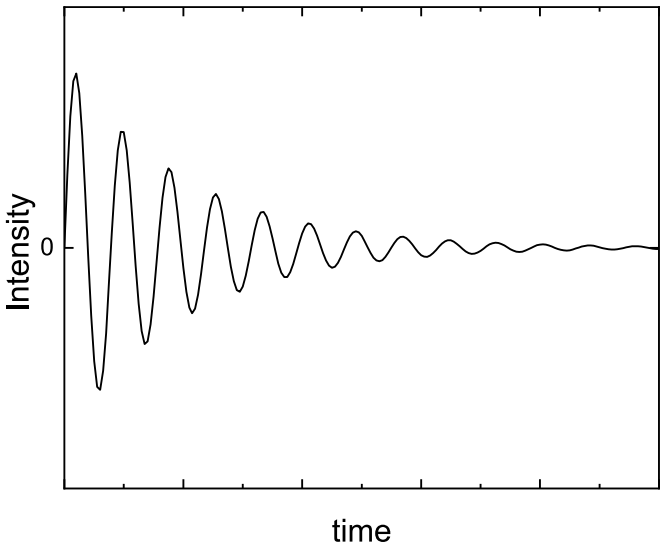

Figure 3.3 shows a free induction decay (FID). It is the response of a sample at one probe frequency for a scan over the time delay between both pump pulses.

$$f(\omega) = \mathrm{FT}(f(t)) \equiv \frac{1}{\sqrt{2\pi}} \int_{-\infty}^{\infty} f(t) e^{i\omega t} \mathrm{d}t \tag{3.8}$$

In order to enhance the resolution of our spectra in the frequency-domain, which are retrieved by Fourier transformation from the time-domain data, zero-padding can be used. Here, the amount of data points in the time-domain is enhanced by adding zeros to the data set. This results in a higher frequency resolution after Fourier transformation. Further, the influence of truncation artefacts are reduced by applying a Hamming windowing function. Truncation artefacts are caused by the Fourier transformation of FIDs which did not completely decay to zero. In such cases an artificial step in the time-domain can be introduced to the data by extending such a not fully decayed FID by zero-padding. Mathematically, such a step can be described as the multiplication of the data with a square function. The Fourier transform of the square function in time to the frequency-domain is the sinc function. The oscillations of the sinc function can easily be misinterpreted as additional peaks in the spectrum. In order to prevent a step in the time-domain data, a function which smoothens the transition from the measured FID to the zero-padded extension can be used. Therefore, in this work the Hamming windowing function $s(t_\mathrm{W})$, which is shown below, is applied to the FID before Fourier transformation.[44]

$$s(t_\mathrm{W}) = 0.54 + 0.46 \cos\left(\pi \frac{t_\mathrm{W}}{t_\mathrm{W,max}}\right) \tag{3.9}$$

Here, t_W is the time delay between the two pump pulses and $t_\mathrm{W,max}$ the maximal time delay between both pump pulses measured.[44] In order to obtain pump frequency resolution, a germanium (Ge) acousto-optic modulator (AOM) is used (Figure 3.4a). The

AOM shapes the incoming mid-IR pulses, by choosing amplitude and phase as desired (for each frequency). In order to do so, the IR pulse is first dispersed at a grating, separating all frequencies of the pulse in space. The beams are collimated by a parabolic mirror and focused in the Fourier plane into the AOM at the Bragg angle of ~2°. An arbitrary waveform generator is used to create an acoustic wave, which propagates along the long side of the Germanium crystal of the AOM (roughly perpendicular to the pathway of the IR). Due to the difference in velocity of the acoustic wave and the IR pulse, the acoustic wave appears as static to the IR pulse. It can be applied as a mask which means, the acoustic wave acts as a modulated grating on the IR pulse, allowing to individually tune the amplitude and phase of each frequency. This allows altering the IR spectrum after the AOM as desired by creating two pulses out of one original pulse and changing the time delay τ between both pulses. The interference of both pulses leads to the desired spectrum. The phase of the mask allows to shift the two pulses created in the AOM in time. This is used to keep the later one of the two pump pulses at a constant time relative to the probe pump. Hence, a scan over different τ does not affect the time difference between pump and probe pulse (the waiting time t_W). Figure 3.4b shows the pulse sequence and the different delay times between the pump pulses and the probe pulse. Both generated pump pulses are then focused on a second grating by a parabolic mirror in order to realign all frequencies. One major advantage of the AOM is that it can apply a different modulated grating to each pump pulse (at a rate of 1 kHz) and therefore, the sample can be excited at different frequencies for each individual probe pulse.[78,80,84]

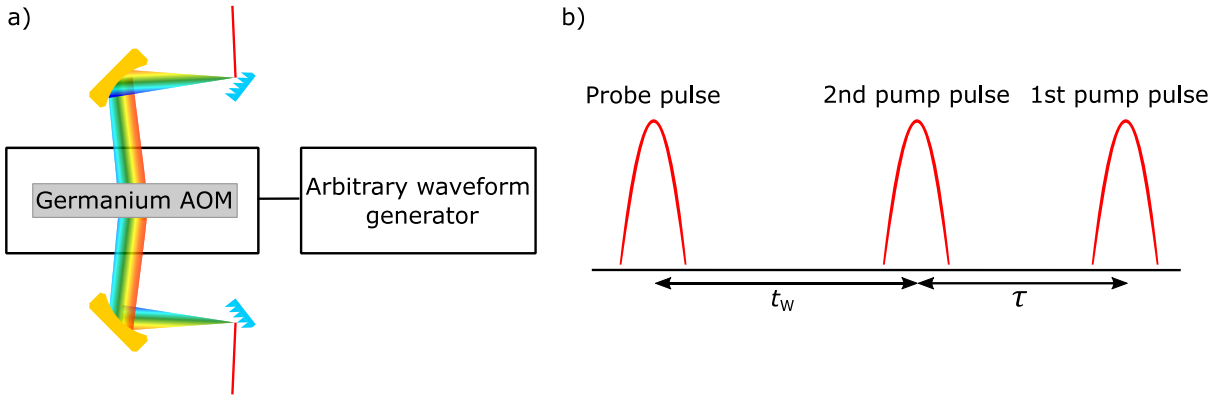

Figure 3.4 a) setup of an AOM (Germanium acousto-optic modulator). An ultra-short IR pulse is diffracted at a grating and collimated by a parabolic silver mirror. Within the AOM the pulse is split into two pulses. This way the phase and amplitude for each frequency of the interference pattern of both pump pulses can be chosen as desired. The AOM uses a longitudinal sound wave traveling through the Ge crystal as a modulated grating which allows setting a different grating for each laser pulse. This way a different pump spectrum for each laser pulse can be chosen. b) shows the pulse sequence at the sample. First the two pump pulses arrive. By adjusting the time difference τ between them, all or only selected frequencies can be pumped. After the second pump pulse and the waiting time t_W the probe pulse passes the sample.

One advantage of the pulse shaper in the pump path is the control of the phase of the pump pulses. It allows not only chopping the pump and thus measuring one-dimensional pump-probe spectra, but also to subtract scatter or apply a rotating frame. In order to remove scatter or a transient absorption background, phase cycling can be used.[44]

Phase cycling takes advantage of the fact that the phase of the transient third-order peak depends on the phase shift between both pump pulses $\Delta\phi$. The transient absorption background is, however, independent of the phase of the pump pulses ϕ. Therefore, measuring two times, once with a phase shift of $\Delta\phi = 0$ and once with a phase shift of $\Delta\phi = \pi$ between both pump pulses and subtracting them, results in a spectrum where the transient absorption background is removed. The wanted signal, however, is added together and therefore enhanced by the factor of two. In order to also remove pump scatter, the more complex phase cycling sequence shown below has to be applied.[44]

$$S_{\mathrm{PC}} = S(\phi_1 = 0, \phi_2 = 0) - S(\phi_1 = 0, \phi_2 = \pi) + S(\phi_1 = \pi, \phi_2 = \pi) - S(\phi_1 = \pi, \phi_2 = 0) \tag{3.10}$$

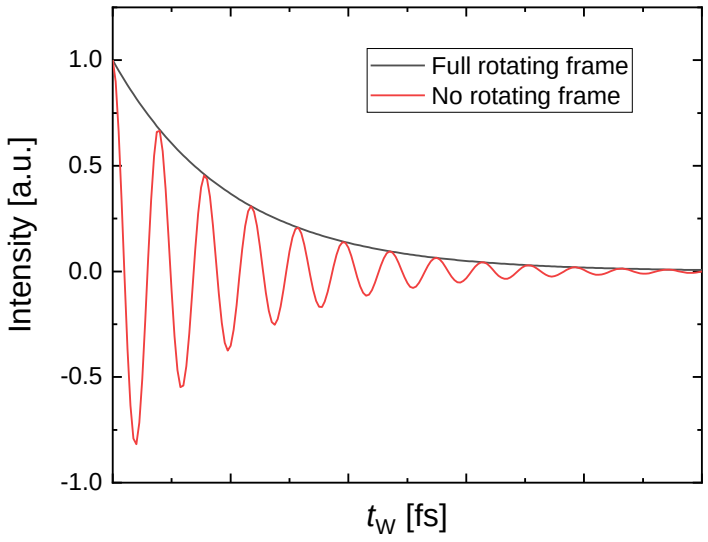

Figure 3.5 shows the effect of a rotating frame. In red, a FID without an applied rotating frame is shown. In black an FID with an applied rotating frame is shown. One can intuitively understand that far fewer data points in time are needed to resolve the black curve, compared to the red one.

Thus, the transient absorption background as well as any scatter from the pump pulse is subtracted. Further, the signal S_{PC} is enhanced by summation of the signals of the four measurements.[44] Another advantage of the pulse shaper and the resulting phase control is that one can acquire data in a so-called 'rotating frame'. This allows reducing the number of data points which have to be acquired to resolve the FID. If the oscillation of a molecule is at around $\omega_{os} = 2000$ cm^{-1}, the FID contains this fundamental frequency. However, the desired information (lineshape, broadening, frequency fluctuations) is contained within the envelope of the oscillation. Therefore, working in a rotating frame, removes the oscillation and only leaves the envelope (see Figure 3.5). This is done experimentally by simultaneously changing the time delay τ between both pump pulses

while also adjusting the phase difference $\Delta\phi$ between them. Usually, not a full but a partial rotating frame is applied, which means that the rotating frame is set to a frequency below the frequency of interest (e.g. $\omega_r = 1820$ cm^{-1}). For the oscillation of interest, this results in a reduced frequency of the FID ($\omega_{os} - \omega_r = 180$ cm^{-1}). This reduced FID frequency can then be sampled with fewer data points and, thus, brings the advantage of a faster data acquisition.[44]

4 Complexity in acid-base titrations: Multimer formation between phosphoric acids and imines

Reproduced with permission and minor changes from "C. Malm, H. Kim, M. Wagner and J. Hunger, Complexity in Acid-Base Titrations: Multimer Formation Between Phosphoric Acids and Imines, *Chem. - A Eur. J.*, 2017, **23**, 10853–10860."

This project has received funding from the European ResearchCouncil (ERC) under the European Union's Horizon 2020 research and innovation programme (grant agreement n8 714691) and H.K. acknowledges funding within grant agreement n8 658467.

4.1 Introduction

Solutions of Brønsted acids with bases have been intensively studied as model systems to understand the fundamentals of e.g. strong hydrogen-bonding,[85–89] proton transfer pathways,[90–92] Brønsted acid organocatalysis,[18,25,93–95] or mechanisms of enzymatic activity.[96] In general, upon association of an acid and a base, the proton is shared between the two molecules and the quantum nature of the light proton results in substantial delocalization of the proton between the acidic and the basic group.[19] This delocalization also limits the experimental and computational methods that are suitable to study such interaction. Experimentally, valuable insight into the location of the proton and as such the nature of the bond between the acids and bases has been obtained from nuclear magnetic resonance (NMR) experiments at reduced temperatures.[25,90,96] For specific acids and bases the information obtained using NMR has been complemented by optical or vibrational spectroscopies.[88,90,91] To date many studies have focused on carboxylic acids and it has been concluded that the nature of this strong bond varies between a hydrogen-bonded complex with the proton located in the proximity of the acid and an ion-pair (full proton transfer), depending on the chemical nature of the acid and the base.[90]

The interaction of phosphoric acid derivatives with organic imine bases in aprotic solvents has only in recent years received increasing attention, as these acid-base combinations are highly relevant to the emerging field of (asymmetric) organocatalysis.[5,9,10,14] Analogously to carboxylic acids, the interaction of such phosphoric acids with various imines has been studied using both computational[97–100] and experimental[18,25,93,94,97,99] methods. It has remained challenging, however, to study complexes formed between phosphoric acids and imines at conditions that are relevant to the catalytic process: For instance, with computational approaches the solvent is typically approximated by a continuum[98] and NMR experiments are mostly performed at temperatures below the reaction temperature.[25,93,95] We have recently shown using a combination of dielectric relaxation spectroscopy (DRS), NMR spectroscopy, and *ab initio* calculations that the nature of catalyst-substrate interaction can be elucidated at catalytically relevant temperatures and in a range of molecular solvents.[18] By studying

equimolar solutions of a substituted phosphoric acid and quinaldine, an aromatic heterocycle, we could show that the interaction is dominated by proton transfer from the acid to the base and subsequent formation of an ion-pair. The dissociation of these ion-pairs into free ions is correlated with a reduced enantioselectivity in the catalytic process. In contrast to some earlier reports,[25] the dominant formation of ion-pairs as intermediates has been recently confirmed using NMR experiments.[95]

While these recent studies[18,25,93,95] have advanced our understanding of the interaction between phosphoric acids and imine bases, these studies were limited to equimolar solutions of acids and bases. Under realistic catalytic conditions, however, only a few mole percent of acid is added as catalyst.[9] Also computational approaches typically consider only one substrate and one catalyst molecule,[101] which limits such studies to a single bimolecular reaction pathway. Experimentally however, there is evidence for the formation of more than one intermediate between the acid and the base.[25] In order to understand the catalytic mechanism it is vital to explore which intermediates are formed at compositions comparable to the catalytic process. Correlating the properties of the formed intermediates to the catalytic activity has the potential to improve prediction of catalyst performance,[23,94] as current approaches rely on the average properties of all acids and/or bases in solution (e.g. the averaged NMR chemical shift[23,94] or vibrational frequencies[23]).

In order to investigate the intermediate that is the dominant species at compositions relevant to catalysis, we herein report a detailed study on the interaction between a substituted phosphoric acid (diphenyl phosphoric acid, DPP) and an aromatic imine (quinaldine, Qu) dissolved in dichloromethane at ambient temperature, which is relevant to the transfer hydrogenation reaction catalysed by phosphoric acids (see Figure 4.1).[16] By using a combination of dielectric relaxation and NMR spectroscopy, we particularly focus on the effect of the ratio between the DPP and Qu dissolved in dichloromethane. We find that at low concentrations of acid, Qu and DPP predominantly aggregate to bimolecular QuH^+-DPP^- ion-pairs. With increasing concentration of DPP, multimers (e.g. QuH^+-DPP^--DPP) are formed to a significant extent and at the commonly studied equimolar samples these multimers constitute more than 30% of the observed molecular aggregates between DPP and Qu.

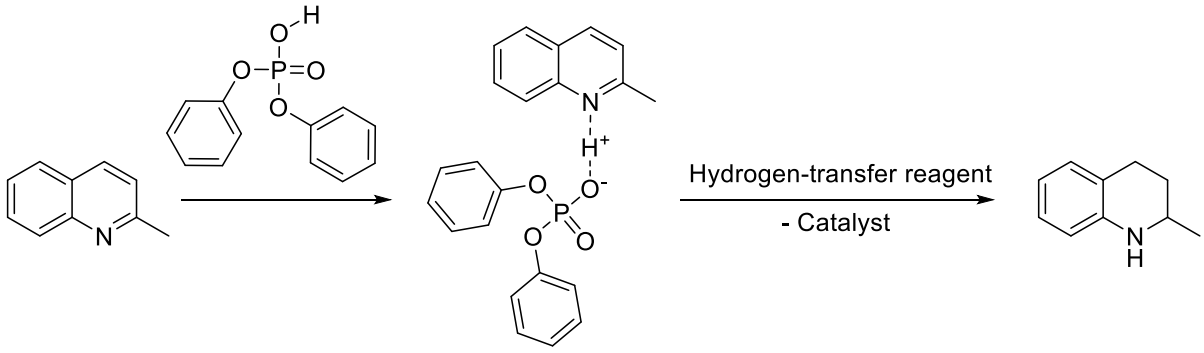

Figure 4.1 Reaction scheme of the Brønsted acid catalysed transfer hydrogenation. The catalyst (diphenyl phosphoric acid) activates the imine (quinaldine), followed by hydrogenation yielding the tetrahydroquinaldien derivate.

4.2 Experimental section

Diphenyl phosphoric acid (DPP) was purchased from Sigma-Aldrich and dried in vacuo (<$2 \cdot 10^{-2}$ mbar) for at least 8 hours. Quinaldine (Qu) was obtained from Sigma-Aldrich and used without further purification. The solvents dichloromethane (CH_2Cl_2, ACS reagent grade, Sigma-Aldrich) and deuterated dichloromethane (CD_2Cl_2, Carl Roth) were stored over molecular sieve (4 Å) and filtered using a 0.2 µm Omnipore membrane filter prior to use. Stock solutions of DPP and Qu were prepared by weighing the appropriate amount DPP or Qu into a volumetric flask and dissolving the solute in dichloromethane. Samples with different stoichiometric ratios between Qu and DPP were prepared, by mixing the corresponding volume of both stock solutions and the solvent using graduated glass pipettes. For NMR experiments a total sample volume of 1 mL was prepared for each sample using CD_2Cl_2. For DRS experiments we prepared samples with a total volume of 4 mL using CH_2Cl_2.

4.3 Results and discussion

4.3.1 NMR titration experiments

To study the interaction between Qu and DPP as a function of their molar ratio in dichloromethane, we performed a titration experiment: In all samples the concentration of Qu was kept constant at $c_{\mathrm{Qu}} = 0.1$ mol L^{-1}, while the concentration of DPP was varied such that we cover both, samples with an excess of Qu and an excess of DPP. As we have shown previously, the ^{1}H-NMR chemical shift of protons of Qu is very sensitive to protonation of Qu by DPP.[18] Hence, to monitor the proton transfer in the titration experiment, we recorded the ^{1}H-NMR spectra of Qu with simultaneously increasing c_{DPP} from 0.01 mol L^{-1} to 0.5 mol L^{-1}. As can be seen from the chemical shift of the H4 proton of Qu, δ_{H4}, (located opposite to the nitrogen atom in the six-membered heterocycle, see inset of Figure 4.2a), the variation of the chemical shift is in accordance to what one would expect for titration of a base with an acid (Figure 4.2a): At $c_{\mathrm{DPP}} \leq c_{\mathrm{Qu}}$ the value of δ_{H4} increases with increasing concentration of acid, in line with a partial protonation of some Qu molecules and δ_{H4} representing the (motionally) averaged chemical shift of Qu and QuH^+. The increase of δ_{H4} therefore reflects a reduction of the shielding of this specific proton, which can be readily related to a reduction of the average electron density in the vicinity of the H4 proton upon protonation of Qu. For samples with an excess of DPP $c_{\mathrm{DPP}} > 0.1$ mol L^{-1} the δ_{H4} values reach a plateau, which suggests that an excess of DPP does hardly affect the electronic environment of H4 (i.e. quantitative protonation of all Qu). In analogy to the observations for H4, also the chemical shifts for protons H3-H7 exhibit similar trends (see Supporting Information, SI, Figure 4.6). The magnitude of the variation amongst H3-H7 is however largest for H4 (Figure 4.6), which is in line with this

position being the initial reactive centre for the hydride transfer in the hydrogenation reaction (Figure 4.1).[6]

Conversely, the chemical shift of H8 varies markedly different with increasing concentration of DPP: At $c_{DPP} \leq c_{Qu}$ the value of δ_{H8} increases – similar to our findings for H3-H7. However, at $c_{DPP} > 0.1$ mol L^{-1} the value for δ_{H8} shows a pronounced decrease with increasing concentration of DPP. At $c_{DPP} = 0.5$ mol L^{-1} the value of δ_{H8} nearly assumes the values close to neat solution of Qu (in the absence of any acid). We note that we find a similar behaviour for the chemical shift of the methyl group δ_{H9} (see Figure 4.7, SI). Our results thus show that an excess of DPP increasingly shields the protons H8 and H9, relative to the equimolar mixture of DPP and Qu.

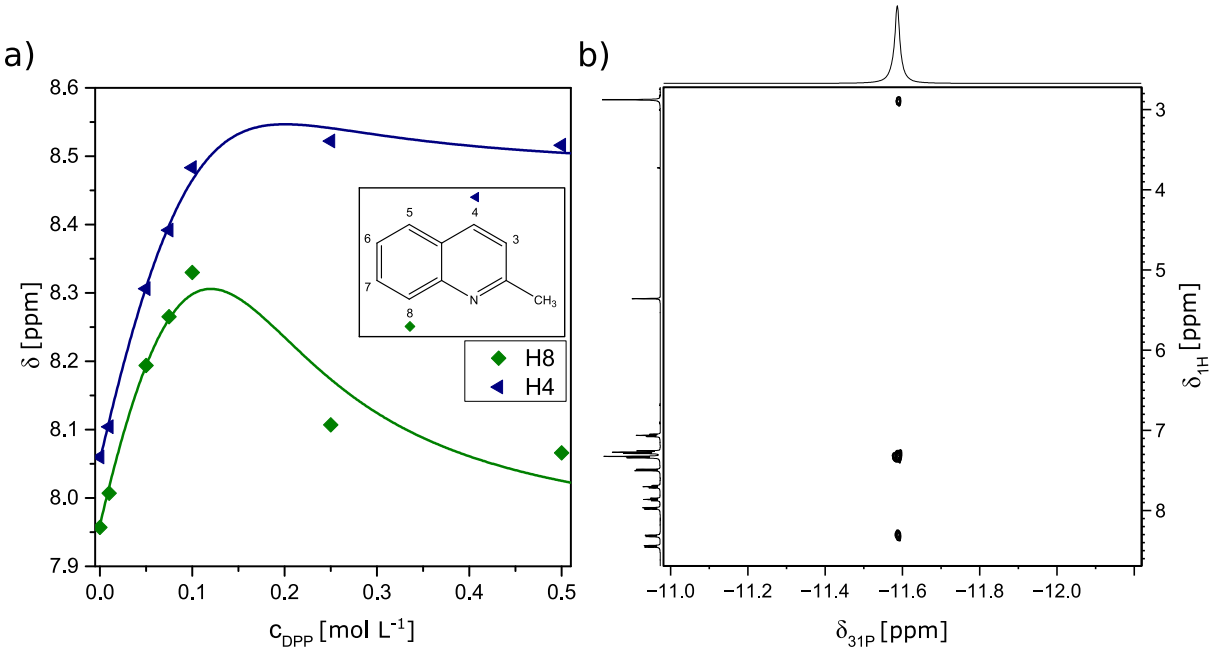

Figure 4.2 a) Chemical shift of the protons H4 and H8 of Qu as a function of DPP concentration at a constant Qu concentration of 0.1 mol L^{-1}: the proton in close proximity to the nitrogen (H8) shows an increased shielding with increasing excess of acid, while the chemical shift of H4 nearly exhibits the sigmoidal behaviour that would be expected for acid-base titrations. Symbols correspond to experimental data and solid lines show the description with the association model (eq. (4.4). b) HOESY spectrum of an equimolar (0.1 mol L^{-1}) solution of DPP and Qu. Cross-peaks evidence proximity of the phosphor not only to the phenyl groups (~7.3 ppm) of the DPP but also to H8 (~8.3 ppm) and the methyl group H9 (2.9 ppm) of Qu. Note, that small signals in the ^{1}H spectra at 6.9, 6.7 and 3.7 ppm originate from a minor impurity, presumably p-anisidine, which does not affect our conclusions.

Hence, the NMR titration experiment demonstrates that only at $c_{DPP} \ll c_{Qu}$, the observed chemical shift is dominated by deprotonation of DPP and the corresponding partial protonation of Qu. With increasing concentration of DPP the shielding of protons of Qu in the direct vicinity of the aromatic nitrogen (H8 and methyl group H9) however deviates from what one would expect for quantitative, bimolecular proton transfer between Qu and DPP.

To explore the origin of the counterintuitive shielding of H8 and H9 we use HOESY. This technique is sensitive to through space interactions (~<5 Å) between phosphor and protons (also in absence of coupling through a chemical bond). Such a two-dimensional ^{31}P-^{1}H HOESY spectrum (Figure 4.2b) shows three pronounced cross-peaks: The most intense cross-peak is due to the intramolecular interaction between the ^{31}P ($\delta_{^{31}\mathrm{P}} = -11.6$ ppm) and the phenyl groups of the DPP ($\delta_{^{1}\mathrm{H,phenyl}} \approx 7.3$ ppm). More importantly, we find two additional intermolecular cross-peaks evidencing interaction with Qu: The HOESY spectrum for an equimolar solution of DPP and Qu show interaction of the ^{31}P nuclei with protons located at $\delta_{\mathrm{H8}} = 8.3$ ppm and $\delta_{\mathrm{H9}} = 2.9$ ppm for Qu, the two signals that show the decrease in chemical shift upon adding an excess of DPP. Thus, the HOESY spectrum provides strong evidence that the peculiar behaviour of H8 and H9 for an excess of DPP in the titration experiment can be traced back to DPP in the direct proximity of these protons, i.e. the formation of molecular aggregates between QuH^+ and DPP^-. This observation is in line with our previous study,[18] where we could show that the dielectric spectra of equimolar solutions are dominated by QuH^+–DPP^- ion-pairs.

4.3.2 Dielectric relaxation spectroscopy

Accordingly, to obtain further insight into the species that are formed in solution as a function of the molar ratio between Qu and DPP, we perform DRS experiments with varying sample composition. In general, DRS spectra are dominated by the rotation of molecular level dipoles. As ion-pairs (e.g. QuH^+-DPP^- ion-pairs[18]) have an intrinsically large electrical dipole moment, DRS is particularly sensitive to the formation of ion-pairs.[102] In Figure 4.3a we show the complex permittivity spectra for solutions containing 0.1 mol L^{-1} Qu with varying concentration of DPP. All spectra show a relaxation process, which is characterized by a dispersion in the dielectric permittivity, $\varepsilon'(\nu)$, and a peak in the dielectric loss, $\varepsilon''(\nu)$, centered at ~70 GHz. This relaxation mode can be readily assigned to the rotational diffusion of the dipolar solvent dichloromethane (see also black solid lines in Figure 4.3a).[59] Besides a minor reduction in relaxation amplitude of this mode due to the decreasing volume concentration of dichloromethane with increasing solute concentration, the relaxation of dichloromethane is nearly unaffected by the addition of DPP, which indicates that the added solute does not bind dichloromethane strongly in its solvation shell. The addition of DPP to the quinaldine solution leads to the appearance of at least one broad relaxation in the range centred at about 2 GHz.

Thus, this relaxation can be assigned to be due to the solutes and its amplitude is increasing with increasing DPP concentration. The increasing amplitude goes along with an increase in the limiting permittivity at low frequencies ($\varepsilon_s = \lim_{\nu \to 0} \varepsilon'(\nu)$), i.e. the static dielectric constant. As can be seen in Figure 4.3b, the static permittivity of the samples is monotonically increasing with increasing concentration of DPP (black symbols in Figure 4.3b). This observation is in stark contrast to solutions of only DPP in dichloromethane (in the absence of Qu), where the static permittivity decreases with increasing concentration of acid (red symbols in Figure 4.3b), see also SI Figure 4.8). In general, the static dielectric constant is a measure of the volume concentration of electrical dipoles (multiplied by their squared electrical dipole moment, see also

below).[51] Thus, the increase of ε_s with increasing c_{DPP} for solutions containing Qu indicates the formation of dipolar aggregates upon addition of DPP over the entire concentration range of the present study. Contrarily, our data suggest that addition of DPP does not go along with the formation of dipolar species in the absence of quinaldine. Notably, ε_s exhibits a steep increase at low concentrations of DPP ($c_{DPP} < 0.1$ mol L^{-1}), while the slope of ε_s vs c_{DPP} is reduced for an excess of DPP ($c_{DPP} > 0.1$ mol L^{-1}). Hence, in line with the interaction of DPP and Qu at all studied concentrations as concluded from Figure 4.2, the values of ε_s indicate that dipolar species are formed and/or the electrical dipole moment of these species is increased upon adding DPP over the entire concentration range of the present study.

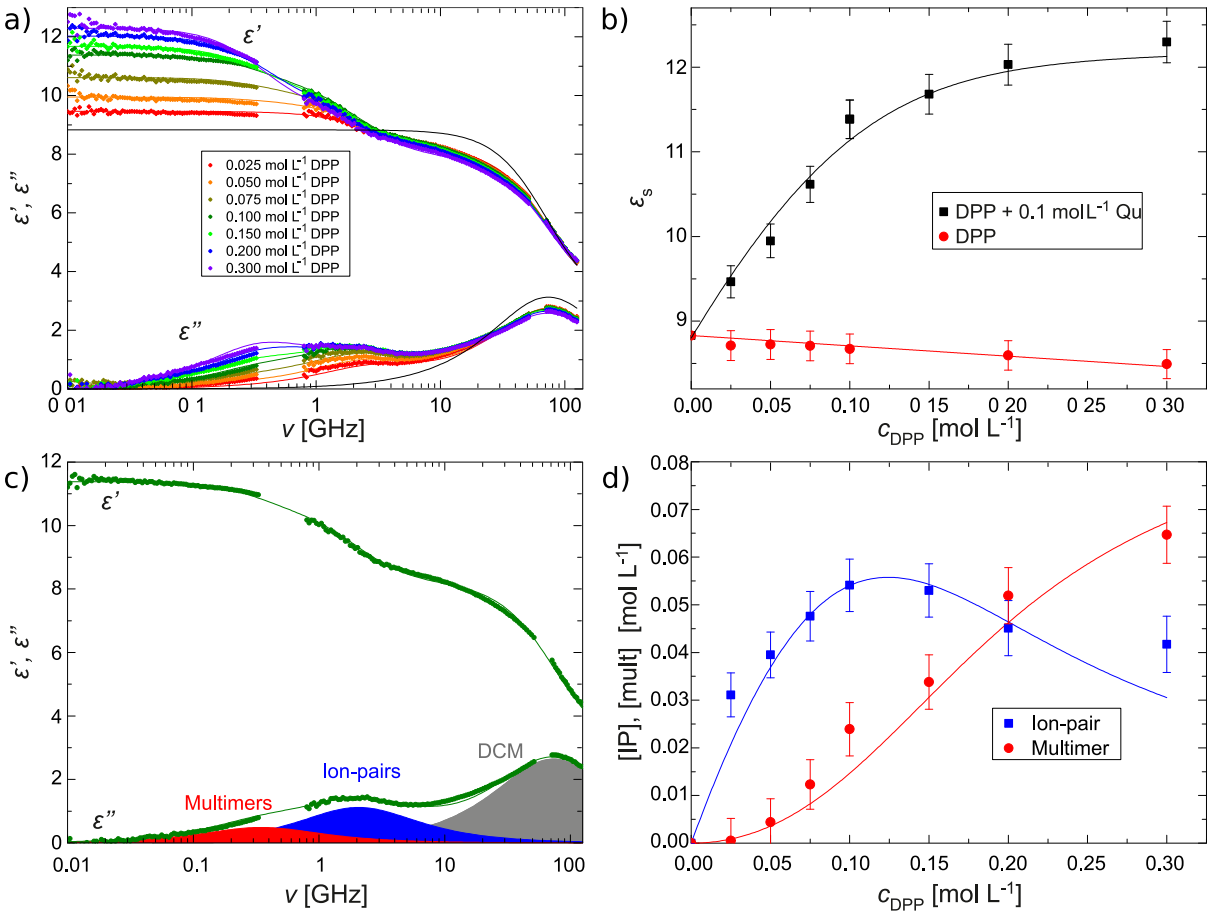

Figure 4.3 a) Dielectric permittivity, $\boldsymbol{\varepsilon'(\nu)}$, and dielectric loss spectra, $\boldsymbol{\varepsilon''(\nu)}$, for solutions of 0.1 mol L^{-1} Qu with varying concentration of DPP. Symbols show experimental data and lines show the fit of eq. (4.1) to the spectra. The black solid line shows the dielectric spectrum of the solvent, dichloromethane, which was taken from literature.[59] Note that for visual clarity the contribution due to the Ohmic loss (last term of eq. (4.1) has been subtracted. b) Extrapolated static permittivity, $\boldsymbol{\varepsilon_s}$, vs concentration of DPP for solution of neat DPP (red symbols) and solutions containing 0.1 mol L^{-1} Qu (black symbols). Error bars are estimated to 0.02 $\boldsymbol{\varepsilon_s}$.[102] Solid lines are a visual aid. c) Dielectric spectrum of an equimolar mixture of DPP and Qu. Symbols show experimental data and the solid lines show the fits using eq. (4.1). Shaded areas indicate the contribution of the three relaxation modes (multimer, ion-pair, and solvent) to the dielectric loss (see eq. (4.1) d) Calculated concentrations of ion-pairs (blue squares) and multimers (red circles) as extracted from the dielectric relaxation amplitudes (for details see text and SI). Error bars were estimated assuming an uncertainty of 0.02 $\boldsymbol{\varepsilon_s}$[102] in the relaxation strength. Solid lines show fits of the association model (eq. (4.2) & (4.3)) to the data. Note that the deviations of the fit from that data at c_{DPP} = 0.3 mol L^{-1} can be explained neglecting aggregates larger than trimers in eq. (4.2) & (4.3).

In order to quantitatively analyse the dielectric spectra, we fit a relaxation model to the spectra consisting of multiple relaxation modes to the spectra. This model obviously contains contributions due to the solvent at 70 GHz (2 ps).[59] The relaxation of the solute between 0.1 and 5 GHz has an asymmetric shape and its symmetry varies with concentration of DPP: while the maximum in ε'' is located at ~ 2 GHz for low concentrations of DPP, a pronounced shoulder appears at ~ 0.4 GHz at high concentrations of DPP. This asymmetry provides evidence for the presence of at least two relaxation modes due to the solutes. Due to the prevalence of the 2 GHz relaxation mode at low c_{DPP} (see also below), we assign this relaxation mode to the smallest conceivable aggregate between Qu and DPP: QuH^+-DPP^- ion-pairs (see also Ref[18]).* As the peak position in dielectric spectra is determined by the molecular volume of the rotating dipoles (and the sample's viscosity),[51,59] the location of the second relaxation mode at 0.4 GHz suggests that these dipolar species have a larger molecular volume (compared to the ion-pairs). We therefore assign this lower frequency relaxation to the rotation of multimers (at least QuH^+-DPP^--DPP trimers) formed between DPP and Qu. Hence, we use a combination of three (Debye-type) relaxation modes† to describe the experimental spectra, which is the model with the least number of parameters that gave a consistent description of the experimental data:

$$\hat{\varepsilon}(\nu) = \frac{S_{\mathrm{mult}}}{1 + 2\pi \boldsymbol{i} \nu \tau_{\mathrm{mult}}} + \frac{S_{\mathrm{IP}}}{1 + 2\pi \boldsymbol{i} \nu \tau_{\mathrm{IP}}} + \frac{S_{\mathrm{DCM}}}{1 + 2\pi \boldsymbol{i} \nu \tau_{\mathrm{DCM}}} + \varepsilon_\infty + \frac{\kappa}{2\pi \boldsymbol{i} \nu \varepsilon_0} \qquad (4.1)$$

where S_j and τ_j are the relaxation amplitudes (relaxation strengths) and relaxation times, respectively, with $j =$ mult (multimer), IP (ion-pair), or DCM (dichloromethane). ε_∞ is the limiting permittivity at infinite frequencies, which accounts for all polarization components that are resonant at frequencies above the frequency range of the present study (e.g. due to electronic polarization or vibrational resonances). The last term of eq. (4.1) accounts for Ohmic losses resulting from the electrical conductivity, κ, and ε_0 is the permittivity of free space. Here, we assume κ, which is rather small for the present samples ($\kappa < 0.02$ S/m, see Table 4.3), to be real and independent of frequency (i.e. the dc conductivity of the sample).

As can be seen from Figure 4.3a, eq. (4.1) excellently describes the experimental spectra over the entire frequency range at all studied concentrations. The contribution of the three relaxation modes to the dielectric loss spectrum are shown as shaded areas in Figure 4.3c and the obtained fit parameters are summarized in the SI (Table 4.3 and Figure 4.9). From these fits we find the relaxation time of DCM, $\tau_{\mathrm{DCM}} \approx 2.1$ ps is largely

* Note that the formation of H-bonded Qu-DPP aggregates (without proton transfer) can be excluded based on our earlier experiments and ab initio calculations.[18]

† We note that in our previous study of equimolar mixtures of DPP and Qu,[18] we used a symmetrically broadened Cole–Cole function (broadened with respect to the Debye function), which subsumed the multimer and the ion pair relaxation in equation (4.1). In the present study, the variation of the DPP concentration allows for a separation of both contributions.

unaffected by the presence of solute molecules. The relaxation amplitude S_{DCM} is slightly decreasing with increasing c_{DPP}, which can be related to the reduction (dilution) of the molar concentration of DCM upon adding DPP. Similar to τ_{DCM}, the ion-pair relaxation time τ_{IP} does not vary substantially with varying c_{DPP}. Despite the multimer relaxation is detectable at all studied concentrations, the parameters associated with the multimers (τ_{mult}, S_{mult}) are due to the weak contribution of multimers at $c_{\mathrm{DPP}} < 0.1$ mol L^{-1} somewhat scattered (see Figure 4.9). To reduce the scatter in the data at $c_{\mathrm{DPP}} \leq 0.1$ mol L^{-1}, we fix τ_{mult} to 458 ps, which is the average value obtained at $c_{\mathrm{DPP}} > 0.1$ mol L^{-1}, where S_{mult} is the dominant solute relaxation. This constraint has however little effect on the obtained values of S_{mult} (see Figure 4.9).

The relaxation amplitudes S_{IP} and S_{mult} can be directly related to the concentration of dipolar species, $[j]$ and their squared dipole moment ($S_j \sim [j]\,\mu_j{}^2$, $j = \mathrm{mult, IP}$).[18] To extract the molar concentrations of ion-pairs, [IP], and multimers, [mult], we obtain the electrical dipole moments (μ_j) by assuming that at $c_{\mathrm{DPP}} > 0.1$ mol L^{-1} all Qu molecules form either ion-pairs or multimers and at $c_{\mathrm{DPP}} < 0.1$ mol L^{-1} all DPP molecules from either QuH$^+$-DPP$^-$ ion-pairs or QuH$^+$-DPP$^-$-*n*DPP multimers (see SI). With these boundary conditions we find the electrical dipole moments of the ion-pair and of multimers to be very similar: μ_{mult}=21.4 D and μ_{IP} = 21.5 D (for details see SI, Figure 4.10). The notion that the dipole moment of a QuH$^+$-DPP$^-$ ion-pair is virtually unaffected upon association of an additional DPP molecule to the ion-pair (formation of a QuH$^+$-DPP$^-$-DPP trimer) is also supported by *ab initio* calculations (see SI, Figure 4.11). As can be seen from Figure 4.3d, the thus obtained values for [IP] increase at low c_{DPP} and reach a maximum at $c_{\mathrm{DPP}} \approx 0.1$ mol L^{-1} after which they decrease. The concentration of multimers, [mult], shows a sigmoidal shape with an inflection point at $c_{\mathrm{DPP}} \approx 0.15$ mol L^{-1}. Notably, these results indicate that multimers are present at all concentrations and for an equimolar concentration about ~30 % of all aggregates in solution are multimers. Hence, despite at low DPP concentrations a substantial amount of the base Qu is available, added acid (DPP) does not quantitatively protonate the base, but some fraction of DPP is bound in multimers.

4.3.3 Association model

To quantitatively describe the concentration dependence of ion-pairs and multimers as shown in Figure 4.3d, we use an association model. For convenience we take only the formation of ion-pairs (IP, QuH$^+$-DPP$^-$) and association of one additional DPP molecule to an ion-pair resulting in a trimer (QuH$^+$-DPP$^-$-DPP) into account:

$$\mathrm{Qu} + \mathrm{DPP} \leftrightharpoons \{\mathrm{QuH^+\text{-}DPP^-}\}$$

$$\{\mathrm{QuH^+\text{-}DPP^-}\} + \mathrm{DPP} \leftrightharpoons \{\mathrm{QuH^+\text{-}DPP^-\text{-}DPP}\}$$

Here we neglect dissociation of ion-pairs into free ions, as the number of free ions is very small in dichloromethane.[18] Accordingly, the relevant apparent association equilibria, which are based on concentrations rather than thermodynamic activity, are defined as:

$$K_1 = \frac{[\mathrm{IP}]}{[\mathrm{Qu}][\mathrm{DPP}]} \tag{4.2}$$

$$K_2 = \frac{[\mathrm{mult}]}{[\mathrm{IP}][\mathrm{DPP}]} \tag{4.3}$$

where [Qu] and [DPP] are the concentrations of free quinaldine and free DPP, respectively. K_1 and K_2 are the corresponding apparent association constants. Together with mass conservation ($c_{\mathrm{DPP}} = [\mathrm{DPP}] + [\mathrm{IP}] + 2[\mathrm{mult}]$, and $c_{\mathrm{Qu}} = [\mathrm{Qu}] + [\mathrm{IP}] + [\mathrm{mult}]$), this model can describe the observed concentration dependence of [IP], and [mult] very well (see solid lines in Figure 4.3d with association constants $K_1 = 104$ L mol^{-1} and $K_2 = 16$ L mol^{-1}. Remarkably, these equilibrium constants can also describe the NMR chemical shifts as shown in Figure 4.2: assuming that the observed chemical shift δ is the concentration weighted average of all three species in solution:

$$\delta = \delta_{\mathrm{Qu}} \frac{[\mathrm{Qu}]}{c_{\mathrm{Qu}}} + \delta_{\mathrm{IP}} \frac{[\mathrm{IP}]}{c_{\mathrm{Qu}}} + \delta_{\mathrm{mult}} \frac{[\mathrm{mult}]}{c_{\mathrm{Qu}}} \tag{4.4}$$

where δ_{Qu}, δ_{IP}, and δ_{mult} are the chemical shifts of free Qu, the ion-pair, and the multimer, respectively. As can be seen from the solid lines in Figure 4.2a, also the chemical shifts of δ_{H4} and δ_{H8} (for other protons see SI) can be described by this association models with $K_1 = 104$ L mol^{-1} and $K_2 = 16$ L mol^{-1}, hence confirming that the two equilibria can describe the interaction of DPP and Qu at all studied concentrations. Only for a large excess of DPP ($c_{\mathrm{DPP}} \geq 0.3$ mol L^{-1}) the model somewhat deviates from the experimental data (see Figure 4.2a and 4.3d), which can be explained from the model being limited to formation of ion-pairs and trimers (i.e. it does not account for other multimers). The chemical shifts for neat Qu, ion-pairs and trimers, calculated by fitting the NMR titration data using eq. (4.4) can be found in Table 4.1 (see SI).

4.3.4 Diffusion ordered NMR experiments

To confirm this association behaviour we perform diffusion ordered NMR spectroscopy (DOSY) for solutions containing 0.1 mol L^{-1} Qu at different concentrations of DPP. With DOSY we can relate the (motionally averaged) signals in the ^{1}H-NMR spectra to the diffusivity of these protons (averaged over all species that are present in solution). As the diffusivity of the proton (i.e. the molecule or intermolecular aggregate) scales with the hydrodynamic volume, DOSY provides information on the average size of the aggregates in solution. In general, the signals at 7 to 7.5 ppm can be related to DPP, while protons

with chemical shifts ranging from 7.5 to 9 ppm stem from Qu (Figure 4.4a). For mixtures with $c_{DPP} = 0.1$ mol L^{-1} and $c_{DPP} = 0.05$ mol L^{-1} the average diffusivity of DPP-containing species is lower than the average diffusivity of Qu containing species. This difference is consistent with the association model (eq. (4.4)), where we find that at these concentrations all DPP molecules are incorporated in intermolecular aggregates (ion-pairs or multimers) with large molecular volumes (slow diffusion rates). Simultaneously a significant fraction of free Qu molecules is present for these compositions. As these free Qu molecules have a low hydrodynamic volume, compared to ion-pairs or multimers, the presence of free Qu molecules reduces the average diffusivity of all Qu species at these concentrations. Only for an excess of DPP ($c_{DPP} = 0.5$ mol L^{-1}) all Qu molecules form aggregates with DPP and thus similar diffusivities of protons related to Qu and DPP are observed (Figure 4.4b).

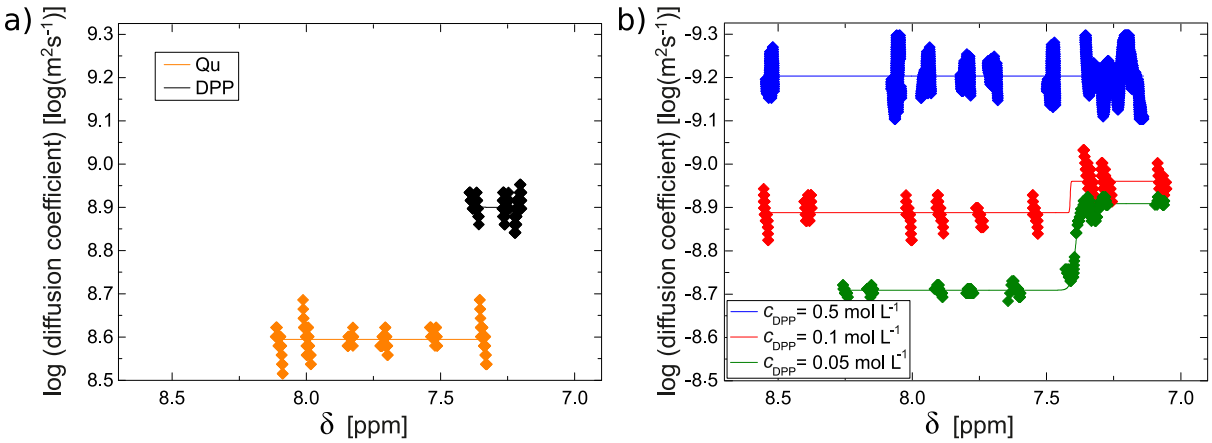

Figure 4.4 a) DOSY experiments for solutions of only Qu and only DPP. b) DOSY experiments for mixtures containing 0.1 mol L^{-1} Qu with varying concentrations of DPP at 298 K: Signals at > 7.5 ppm correspond to Qu, while signals <7.5 ppm originate from the phenyl groups of DPP. The diffusion coefficient of Qu is decreased in the presence of small amounts of DPP. With increasing DPP concentration the diffusion coefficients of Qu and DPP become equal. Symbols show experimental data and solid lines are a visual aid.

4.4 Conclusions

Using a combination of dielectric relaxation and NMR experiments, we show that in solutions of Qu and DPP different intermolecular aggregates are formed, depending on the ratio between the base Qu and the acid DPP. In our titration experiment, multimers containing one QuH^+ cation, one DPP^- anion, and at least one more DPP molecule are formed. We find such multimers – similar to what has been suggested for carboxylic acids[87] – even for solutions containing an excess of Qu. Our results indicate that the electrical dipole moment of these multimers is very similar to that of QuH^+-DPP^- ion-pairs, thus providing evidence for the average location of the negative charge being not affected by the additional DPP molecule. As the NMR experiments show that the additional DPP molecule in the multimers is close to the positively charged NH^+ group of QuH^+, we propose that in the simplest multimer – the trimer – the negative charge is delocalized

between the two hydrogen-bonded DPP molecules (Figure 4.5). Such intermolecular interaction between two DPP molecules in fact closely resembles the dimers of Brønsted acid that have been reported to prevail in weakly polar solvents.[87,103]

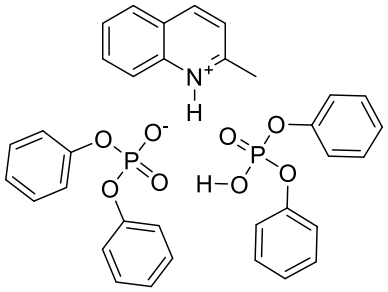

Figure 4.5 Proposed structure of the trimer, consisting of a quinaldinium cation, a diphenyl phosphate anion, and a diphenyl phosphoric acid.

Two association equilibria accounting for formation of Qu^+-DPP^- ion-pairs and Qu^+-DPP^--DPP trimers can describe the interaction of DPP and Qu at all studied concentrations. Remarkably, the association constant for DPP associating with a free quinaldine molecule ($K_1 = 104$ L mol^{-1}) to form a Qu^+-DPP^- ion-pair is only ~6 times lower than the association of DPP to a Qu^+-DPP^- ion-pair ($K_2 = 16$ L mol^{-1}) to form a multimer. This interplay between the two competing association paths is likely very sensitive to the solvent, and thus may explain the very different formation of intermolecular aggregates for other polar, aprotic solvents.[18] We observe these species (ion-pairs and multimers) as separate relaxations in DRS, while their formation leads to motionally averaged signals in NMR. Thus, our results indicate that the lifetime of these aggregates (i.e. the time they exist before the intermolecular bond is broken) is shorter than a few milliseconds (NMR timescale) but longer than a few hundreds of picoseconds (the rotation time in DRS). As the formation of multimers is detected at all concentrations, our results imply that the ratio between the catalyst and the substrate is crucial in order to study reactive intermediates in organocatalysis. The simultaneous presence of different intermediates reported for equimolar mixtures [25] is very likely related to the presence of ion-pairs and multimers in equimolar solutions. Moreover, our results show that in the catalytic process where typically a few mole percent of the phosphoric acid are added to the imine base,[16] ion-pairs are the prevailing intermediates and thus ion-pairs are very likely the active species ion catalysis.[9] Our results also show that trimers are formed at all concentrations even for an excess of base. Based on our association model, these trimers constitute about 1.5 % and 0.7 % of all aggregates at molar ratios of 1:10 and 1:20 (DPP:Qu), which are typical catalyst loadings in organocatalysis. Since a minor species can be decisive for catalysis (Curtin-Hammet principle),[23] these multimers may nevertheless have catalytic significance. In fact, the few mole percent of phosphoric acid that is typically added to the substrate in the organocatalytic process is significantly more than what is used in transition metal catalysis.[104,105] Indeed, The is evidence for strong non-linear effects in phosphoric acid catalysis when ~10 % of catalyst is added, which could only be explained by the activation of the substrate by more than one acid molecule.[106] Similarly, the association of two phosphoric acid molecules at a Ca^{2+} ion has

been suggested to be of catalytic relevance[107] and in recent years catalysts that bear two phosphoric acid moieties on the same molecule[108–110] have been shown to provide superior catalytic activity. In this work we provide a route to identify the different intermediates that are formed in solution and to extract their respective properties: we obtained separately the electronic structure of the ion-pairs and of the multimers from their extracted NMR chemical shifts and the DRS detected electrical dipole moment. Direct correlation of such electronic properties of these intermediates to the catalytic activity can provide mechanistic insight and thus improve prediction of catalytic activity based on their isolated electronic properties.[23,94]

4.5 Supporting information

4.5.1 ^{1}H-NMR titration

In Figure 4.6 we show the variation of the chemical shifts of all aromatic protons (H3-H7, see inset of Figure 4.2a of chapter 4.3.1) of quinaldine with concentration of DPP. The protons H3-H7 show a similar dependence on the acid concentration as H4 (Figure 4.2a): the values of δ increase with increasing c_{DPP} up to c_{DPP} = 0.1 mol L^{-1} and plateau for an excess of DPP. The variation of the chemical shift of H8 (Figures 4.2a and 4.6) is markedly different and the dependence on concentration of acid is similar to that of the methyl group (Figure 4.7).

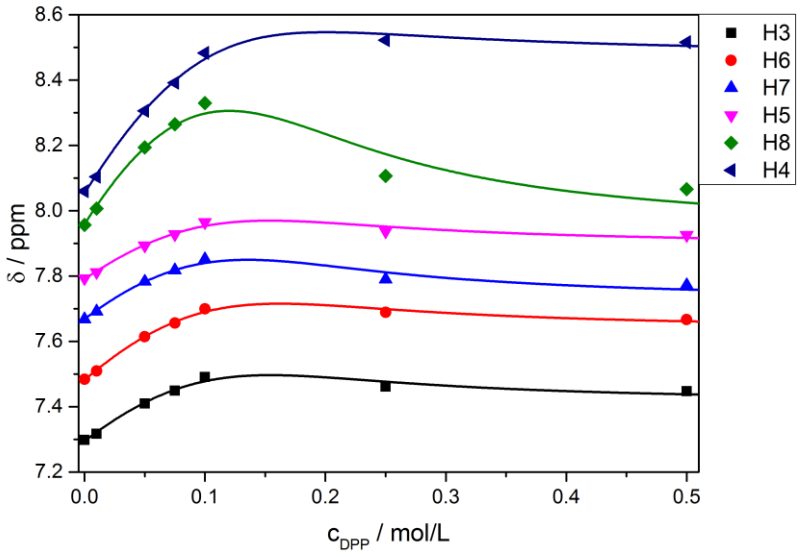

Figure 4.6: Chemical shift of the aromatic protons of quinaldine H3-H8 for solutions contained 0.1 mol L^{-1} quinaldine in dichloromethane as a function of DPP concentration. Symbols show experimental data and the solid lines show fits of eq. (4.3) (see above) with the association constants (eq. (4.2) & (4.3)) obtained from the DRS experiments.

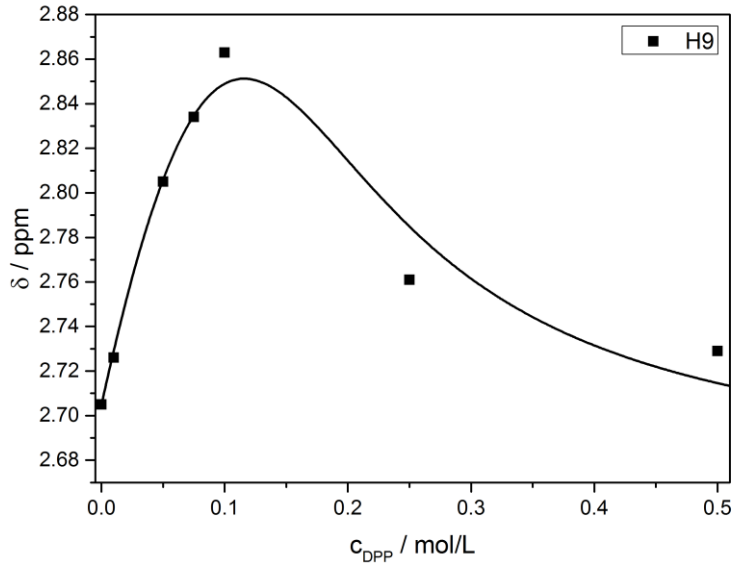

Figure 4.7: Chemical shift of the methyl group of quinaldine (H9) for solutions contained 0.1 mol L^{-1} quinaldine in dichloromethane as a function of DPP concentration. Symbols show experimental data and the solid line shows the fit of eq. (4.4) (see above) with the association constants (eq. (4.2) & (4.3)) obtained from the DRS experiments.

As discussed above we fit eq. (4.4) to the measured chemical shifts of all protons of quinaldine. Here we use the association model as elaborated in eq. (4.2) & (4.3) and the association constants obtained from the DRS experiments ($K_1 = 104$ L mol^{-1}, $K_2 = 16$ L mol^{-1}) to model the concentrations [Qu], [IP], and [mult] at all concentrations of DPP. Thus, the only parameters to describe the data in Figures 3.2, 3.6 & 3.7 are the chemical shifts δ_{Qu}, δ_{IP}, and δ_{mult}. The shifts for the three species obtained from fitting eq. (4.4) to the data are listed in Table 4.1 and are compared to the measured chemical shift of a solution of only quinaldine.

Table 4.4.1: Experimentally determined chemical shifts for a 0.1 mol L^{-1} solution of quinaldine (δ(Qu)) in deuterated dichloromethane, together with the chemical shifts of quinaldine, $\boldsymbol{\delta_{Qu}}$, of the QuH^+-DPP^- ion-pair, $\boldsymbol{\delta_{IP}}$, and the multimers, $\boldsymbol{\delta_{mult}}$, obtained by fitting eq. 3.5 to the concentration dependent experimental chemical shifts.

Qu proton position	Experimental δ(Qu) [ppm]	δ_{Qu} [ppm]	δ_{IP} [ppm]	δ_{mult} [ppm]
H3	7.30	7.30	7.60	7.41
H4	8.06	8.05	8.70	8.47
H5	7.79	7.79	8.07	7.89
H6	7.48	7.48	7.83	7.63
H7	7.67	7.67	7.97	7.72
H8	7.96	7.96	8.60	7.92
H9 (methyl)	2.71	2.71	2.98	2.66

4.5.2 Dielectric spectra of DPP in dichloromethane

In chapter 4.3.2 (Figure 4.3b) we show the static permittivity for solutions of DPP in dichloromethane as a function of c_{DPP}. These values were determined from spectra measured at frequencies ranging from 800 MHz to 54 GHz (Figure 4.8) and are dominated by a relaxation mode centred at ~ 50 GHz, the rotational diffusion of the dipolar solvent dichloromethane.[59] The measured spectra for these solutions show little variation with increasing concentration of DPP. To extract the static permittivity of these solutions we fit – analogously to the relaxation model described above, eq. (4.1) – a relaxation model based on a single Debye relaxation to the spectra:

$$\hat{\varepsilon}(\nu) = \frac{S_{\mathrm{DCM}}}{1 + 2\pi \boldsymbol{i} \nu \tau_{\mathrm{DCM}}} + \varepsilon_{\infty} + \frac{\kappa}{2\pi \boldsymbol{i} \nu \varepsilon_0} \tag{4.5}$$

where S_{DCM} and τ_{DCM} correspond to the relaxation amplitude and the relaxation time of the solvent dichloromethane, respectively. ε_{∞} is the infinite frequency permittivity and κ the sample conductivity. The static permittivity, i.e. the limiting value of ε' at low frequency is defined as: $\varepsilon_s = \varepsilon_{\infty} + S_{\mathrm{DCM}}$. Such fits are shown as solid lines in Figure 4.8 and the parameters obtained from fitting eq. (4.5) to the spectra are listed in Table 4.2.

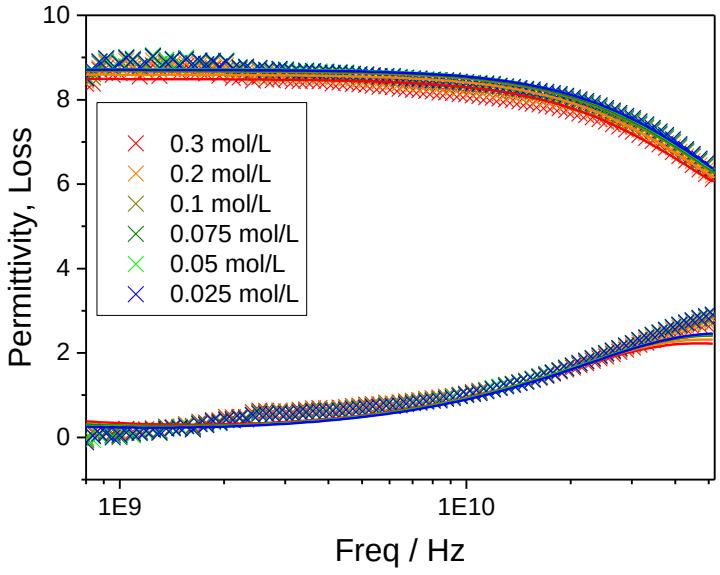

Figure 4.8 Complex permittivity spectra of solutions containing only DPP in dichloromethane. Symbols show experimental data and lines correspond to fits of eq. (4.5) to the spectra.

Table 4.2: Parameters obtained by fitting eq. (4.5) to the dielectric spectra for solutions of DPP in dichloromethane.

c_{DPP} [mol L^{-1}]	S_{DCM}	ε_∞	τ_{DCM} [ps]	κ [S m^{-1}]
0.025	4.44	4.05	3.4	0.00
0.05	4.63	3.96	3.3	0.00
0.075	5.53	3.86	3.1	0.00
0.1	5.68	3.86	3.1	0.00
0.2	5.69	3.83	3.0	0.00
0.3	4.41	3.8	3.0	0.00

4.5.3 Dielectric relaxation parameter for DPP + Qu mixtures

As discussed in chapter 4.3.2, we fit eq. (4.1) to the spectra for solutions of 0.1 mol L^{-1} Qu with varying DPP concentration in dichloromethane. The fits are shown together with the experimental spectra in Figure 4.3a. The parameters obtained from fitting eq. (4.1) to the spectra are listed in Table 4.3 and shown in Figure 4.9. Furthermore, we constrain τ_{mult} to 458 ps at $c_{DPP} \leq 0.1$ mol L^{-1}. As can be seen from the comparison of the parameters of the constraint fit to those obtained from a free fit in Figure 4.9, this constraint hardly affects the relaxations strengths, which are used to extract the concentration of ion-pairs and multimers.

Table 4.3: Relaxation amplitudes, $\boldsymbol{S_j}$, relaxation times, $\boldsymbol{\tau_j}$, limiting permittivity, $\boldsymbol{\varepsilon_\infty}$, and conductivity, $\boldsymbol{\kappa}$ for solutions containing 0.1 mol L^{-1} Qu and varying concentration of DPP in dichloromethane. These fit parameters were obtained by fitting eq. (4.1) to the experimental spectra.

c_{DPP} [mol L^{-1}]	S_{mult}	S_{IP}	S_{DCM}	ε_∞	τ_{mult} [ps]	τ_{IP} [ps]	τ_{DCM} [ps]	κ / S/m
0.025	0.02	1.27	5.41	2.76	458.2	58.4	2.1	0.00
0.05	0.18	1.62	5.37	2.78	458.2	65.3	2.1	0.00
0.075	0.50	1.96	5.33	2.82	458.2	71.2	2.1	0.00
0.1	0.97	2.24	5.29	2.89	458.2	77.2	2.2	0.01
0.15	1.38	2.19	5.22	2.89	501.5	76.0	2.2	0.02
0.2	2.13	1.87	5.14	2.89	420.6	65.6	2.1	0.02
0.3	2.65	1.73	5.01	2.91	452.5	58.9	2.1	0.02

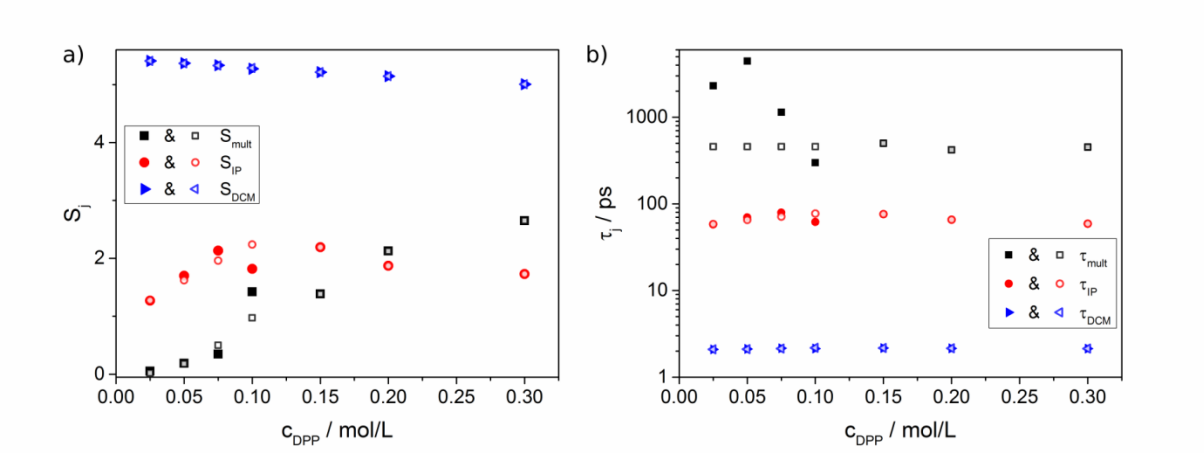

Figure 4.9: Comparison of the relaxation amplitude and relaxation time obtained using a free fit (filled symbols) based on eq. (4.1) to the spectra together with the results using the constraint fit (open symbols, see text).

4.5.4 Electrical dipole moments of the ion-pair and the multimer

To relate the dielectric relaxation amplitudes of the ion-pair, S_{IP}, and the multimer, S_{mult}, to their molar concentrations in solution, [IP] and [mult], we use the Cavell equation.[18,58] In general, the Cavell equation relates the relaxation amplitude S_j to the molar concentration, c_j, of a species j and its electrical the dipole moment μ_j:[18,58]

$$\frac{2\varepsilon_s + 1}{\varepsilon_s} \cdot S_j = \frac{N_A c_j}{k_B T \varepsilon_0} \cdot {\mu_j}^2 \tag{4.6}$$

with the Boltzmann constant k_B= 1.38065*10^{-23} A Vs/K,[1] the vacuum permittivity ε_0 =8.85419*10^{-12} As/Vm,[1] and the Avogadro number N_A= 6.02214 *10^{23} mol^{-1}.[1] T= 294.15 K is the thermodynamic temperature. For convenience we summarize all constants specific to each sample into W resulting in:

$$W \cdot S_j = c_j \cdot {\mu_j}^2 \tag{4.7}$$

As for our experiments, both the concentrations and the dipole moments of the ion-pairs and of the multimers are unknown, we use the following approach to determine the dipole moment of both species. We assume for an excess of DPP (c_{DPP} > 0.1 mol L^{-1}) that the concentration, c_{limit}, that limits the total number of formed intermolecular aggregates is given by the concentration of quinaldine (all quinaldine molecules form either ion-pairs or multimers):

$$c_{limit} = c_{Qu} \text{ for } c_{DPP} > 0.1 \text{ mol/L} \tag{4.8}$$

At low concentrations the limiting concentration is the DPP concentration (all DPP molecules from either ion-pairs or multimers)

$$c_{\mathrm{limit}} = c_{\mathrm{DPP}} \text{ for } c_{\mathrm{DPP}} \leq 0.1 \text{ mol/L} \tag{4.9}$$

Using mass conservation, the limiting concentration c_{limit} can be related to the concentration of ion-pairs, [IP], and multimers, [mult]:

$$c_{\mathrm{limit}} = [\mathrm{IP}] + z * [\mathrm{mult}] \tag{4.10}$$

where $z = 1$ for $c_{\mathrm{DPP}} > 0.1$ mol/L ($c_{\mathrm{limit}} = c_{\mathrm{Qu}}$). At low concentrations of acid, we assume that only ion-pairs and trimers are formed, hence mass conservation for DPP yields $z = 2$ for $c_{\mathrm{DPP}} \leq 0.1$ mol/L.

Based on eq. (4.7), the concentration of the multimer can be related to the dielectric relaxation strength:

$$W \cdot S_{\mathrm{mult}} = {\mu_{\mathrm{mult}}}^2 \cdot [\mathrm{mult}] \tag{4.11}$$

and analogously for the ion-pair:

$$W \cdot S_{\mathrm{IP}} = {\mu_{\mathrm{IP}}}^2 \cdot [\mathrm{IP}] \tag{4.12}$$

Inserting eq. (4.11) & (4.12) into eq. (4.10) gives:

$$c_{\mathrm{limit}} = z \cdot \frac{W \cdot S_{\mathrm{mult}}}{{\mu_{\mathrm{mult}}}^2} + \frac{W \cdot S_{\mathrm{IP}}}{{\mu_{\mathrm{IP}}}^2} \tag{4.13}$$

which can be rearranged to

$$\frac{c_{\mathrm{limit}}}{W \cdot S_{\mathrm{IP}}} = \frac{1}{{\mu_{\mathrm{mult}}}^2} \cdot z \cdot \frac{S_{\mathrm{mult}}}{S_{\mathrm{IP}}} + \frac{1}{{\mu_{\mathrm{IP}}}^2} \tag{4.14}$$

Eq. (4.14) can be used to determine the values for $\mu_{\mathrm{mult}} = 21.4$ D and $\mu_{\mathrm{IP}} = 21.5$ D using a linear regression (Figure 4.9) from the intercept $1/{\mu_{\mathrm{IP}}}^2$ and the slope $1/{\mu_{\mathrm{mult}}}^2$. We note that these values are in excellent agreement with the dipole moment that we determined in our previous study,[18] using only a single broad relaxation mode to describe the solute relaxation (i.e. which subsumed contributions from ion-pairs and multimers). Using these

values for the dipole moments eq. (4.11) & (4.12) can be used to determine the molar concentrations of ion-pairs and multimers for all samples, which are shown in Figure 4.3d.

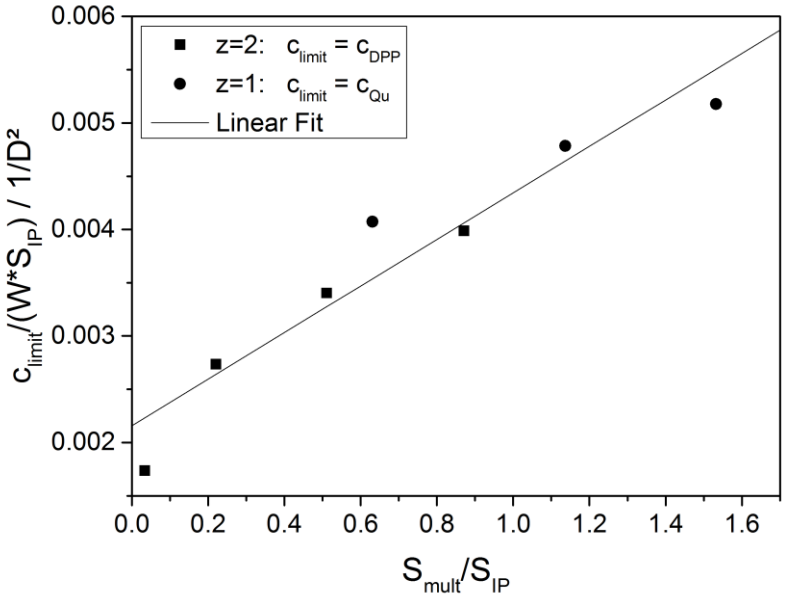

Figure 4.10: Linear regression according to eq. (4.14) to obtain the dipole moments of the ion-pair and the multimer.

4.5.5 Ab initio calculations

The values for the electrical dipole moments are supported by *ab initio* calculations. Geometries of a QuH^+-DPP^- ion-pair and a QuH^+-DPP^--DPP trimer were optimized using the ORCA program package[111] at the HF[112]/SVP[113] level of theory. The solvent was approximated by a continuum using the conductor-like screening model (COSMO, $\varepsilon = 8.83$).[114] The optimized geometries yielded similar electrical dipole moments for the trimer μ_{trimer}=15.2 D and for the ion-pair μ_{IP} = 16.2 D, in agreement with the approach using the experimental values (see above). We note that the *ab initio* values are somewhat lower than the values obtained using eq. (4.14). The lower values from the *ab initio* calculations can be explained from the fact that these were obtained from the energetically most stable structure. Thus, unlike the experimental values, the *ab initio* values do not account for conformational flexibility and deviations from the ideal geometry due to thermal fluctuations. The optimized geometry of the ion-pair and trimer are illustrated in Figure 4.11.

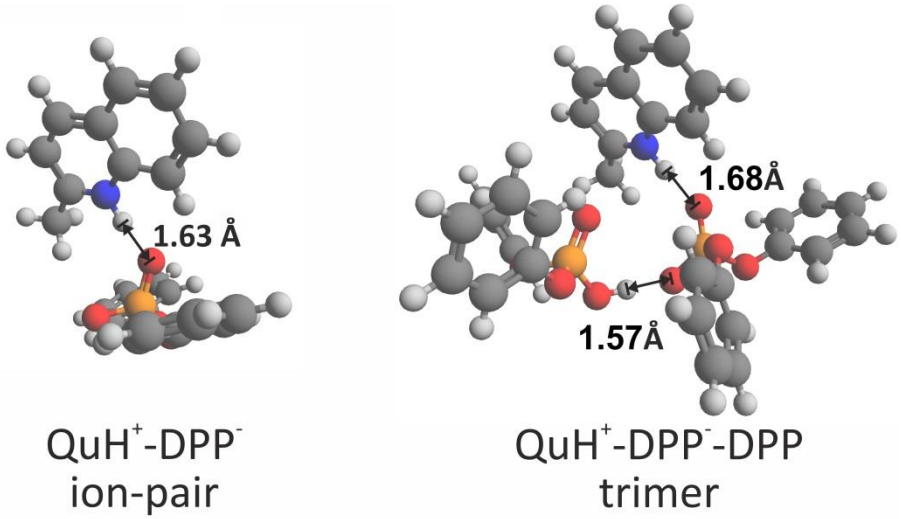

Figure 4.11: Optimized geometry of the QuH^+-DPP- ion-pair (left) and the QuH^+-DPP^--DPP trimer. For the trimer, the optimized geometry shows a bridging hydrogen bond connecting the two DPP molecules with a hydrogen-bonding distance of 1.57 Å. The hydrogen bond between the QuH^+ and the negatively charged DPP^- is 1.68 Å, which is comparable to the hydrogen-bonding distance in the ion-pair (1.63 Å).

5 Determining association equilibria of Brønsted acid organocatalysts with imines – a combined dielectric and nuclear magnetic resonance approach

Paper manuscript is in preparation.

This project has received funding from the European Research Council (ERC) under the European Union's Horizon 2020 research and innovation program (grant agreement no. 714691).

5.1 Introduction

Proton transfer is ubiquitous in nature and the equilibrium position of protons in acid-base aggregates is not only determined by the acidity and basicity of the proton donors and acceptors in e.g. acid-base chemistry, but also by the solvent.[19] One example demonstrating solvent effects is Brønsted acid organocatalysis,[9] in which an acid activates the basic reactants. Here the acidic group is the catalyst's active site. Indeed, for such catalysis the reaction rates have been demonstrated to correlate with the pKa value of the acid.[115] In turn, the enantioselectivities in asymmetric catalysis have been suggested to hardly scale with acidity.[115] However, the catalytic efficiencies have been shown to markedly vary with the solvent:[6,13,16,20] For the organophosphoric acid-catalysed transfer hydrogenation, which has been proven as an efficient pathway to chiral imines,[6,13,16,20,116] especially the solvents chloroform ($CHCl_3$) and dichloromethane (DCM) have been shown to provide high enantioselectivity and yields.[6,16,20] Despite good stereocontrol, yields have been reported to be lower when tetrahydrofuran (THF) is used as a solvent.[18,20,117] In highly polar acetonitrile also enantioselectivity is drastically reduced.[18,118] Despite progress in resolving the reaction mechanism based on experiments[95,119] and theory,[99,100,120] understanding solvent effects has remained challenging,[121] hampering a rational optimization of reaction conditions.[23,122]

The challenge in understanding such solvent effects arises from the complexity of the solutions relevant to catalysis, which consist of several components: solvent, reactants, and catalysts. As such, the molecular-level interaction between the different components and the subtle balance between the different homo- and hetero-aggregation strengths of all components leads to the formation of various aggregates in solution at catalytically relevant temperatures.[74,123–126] For the systems relevant to the phosphoric acid-catalysed transfer hydrogenation, we could recently show that not only heterodimers consisting of the acidic catalyst and the imine base form in solution, but also multimers composed of the imine and more than one phosphoric acid molecule are present.[74] The total number of aggregates in solution only loosely correlates with catalytic efficiency.[18] Yet, such catalyst-reactant intermediates are decisive for catalysis, which has been demonstrated

both computationally[127,128] and experimentally.[129] As such, knowledge of the nature of the aggregates and their abundance can help to understand catalytically active species and thus help to optimize catalytic conditions, e.g. via data-intensive prediction of enantioselectivities.[23]

Here, we study the formation of imine-acid aggregates in solution. In analogy to our previous study, we use diphenyl phosphoric acid (DPP) as a model for organo-phosphoric acid catalysts.[18,25,74,123] We study the interaction of DPP with the bases quinaldine (Qu) and 2-phenylquinoline (PhQu), as a function of the acid to base ratio. Both imines are common reactants in phosphoric acid-catalysed transfer hydrogenations.[9] To discern the role of the solvent, we study solutions in $CHCl_3$, DCM, and THF, which are commonly used solvents in catalysis. To disentangle different aggregates formed in solution, we further advance our previous approach using a combination of nuclear magnetic resonance (NMR) and dielectric relaxation spectroscopy (DRS):[74] We determine the association equilibria from a simultaneous analysis of the NMR chemical shifts of the imine base, which sensitively reports on the motionally averaged electronic density of all bases in solution, and the dielectric relaxation strength of acid-base aggregates, which allows for quantitative assessment of the acid-base dimers and multimers in solution via the rotational relaxation of these dipolar aggregates.

5.2 Experimental section

2-phenylquinoline (PhQu, Alfa Aesar 99 %) and diphenyl phosphoric acid (diphenyl phosphate, DPP, Sigma-Aldrich, 99 %) were used as received. Quinaldine (Qu, Sigma-Aldrich, 95 %) was dried over a 4 Å molecular sieves and filtered using a 0.2 µm Omnipore membrane filter prior to use. The solvents Chloroform ($CHCl_3$, Fisher Scientific, HPLC grade), dichloromethane (DCM, Fisher Scientific, HPLC grade), tetrahydrofuran (THF, Fisher Scientific, HPLC grade), deuterated chloroform ($CDCl_3$, Sigma Aldrich, 99.8 %), deuterated DCM (CD_2Cl_2, Deutero, 99.6 %), and deuterated THF (C_4D_8O, Carl-Roth, 99.5 %) were either taken from fresh bottles or dried over 4 Å molecular sieves and filtered using a 0.2 µm Omnipore membrane filter.

Stock solutions of imine (0.2 mol L^{-1}) and DPP (1.0 mol L^{-1}) were prepared gravimetrically using volumetric flasks. Samples were prepared by mixing the appropriate volumes of stock solutions of the imine and DPP with pure solvent using graduated glass pipettes, assuming ideal mixing volumes. All investigated solutions have a constant imine concentration of 0.1 mol L^{-1}, while c_{DPP} varies from 0.01-0.5 mol L^{-1}. For the NMR experiments, 1 mL of each sample was prepared using the deuterated solvents. For DRS experiments, only non-deuterated solvents were used to produce 2.5, 4 or 4.5 mL total sample volume.

5.3 Results and discussion

To determine the interaction of DPP with organic bases, NMR spectroscopy is a powerful tool to interrogate the electronic environment of the base. In general, as protonation of the base reduces the electron density at the base, a downfield field shift of the base's protons is indicative of proton transfer to the base. As such, NMR titration can be used to infer protonation equilibria[130,131] (and association strengths).[74,132,133]

In Figure 5.1 we show the variation of the chemical shift (δ) for two selected protons of Qu (c_{Qu} = 0.1 mol L^{-1}) in $CDCl_3$ as a function of acid concentration (c_{DPP}). At c_{DPP} < 0.1 mol L^{-1} the values of δ increase monotonically with increasing c_{DPP}, providing evidence for protonation of Qu by DPP (and formation of QuH^+-DPP^- ion-pairs[18,74]). At c_{DPP} > 0.1 mol L^{-1} the chemical shifts decrease with increasing c_{DPP}, which can be explained by the formation of multimers consisting of one Qu and more than one DPP molecules. In these multimers, an additional acid molecule donates a hydrogen bond to an already existing Qu-DPP complex. This decrease of δ is most pronounced for protons in the vicinity of the N atom of Qu, which we have ascribed to the association of the additional DPP molecules in the vicinity of the protonated N atom of Qu.[74]

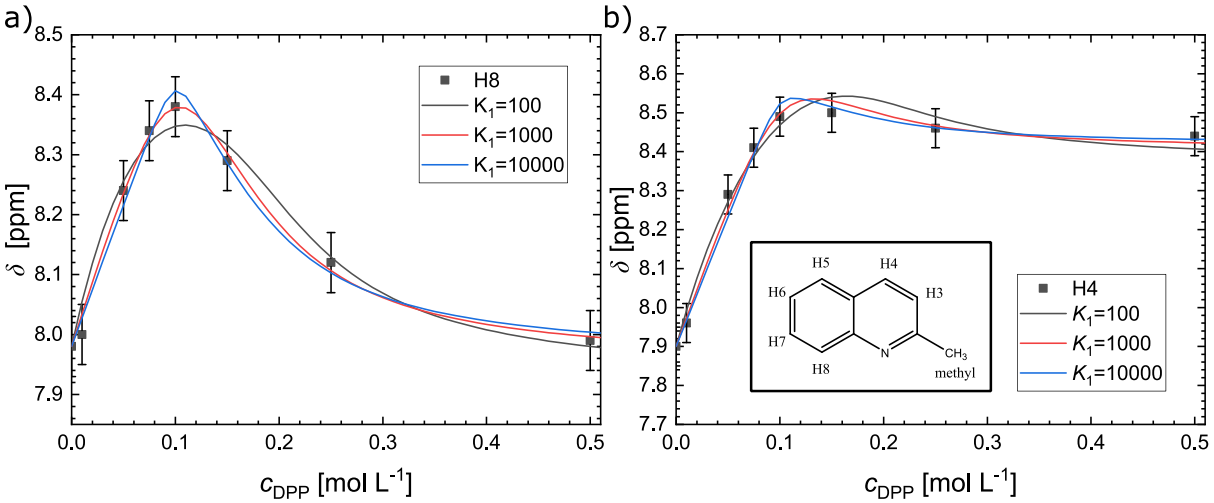

Figure 5.1 Chemical shift of proton H8 a) and H4 b) for a solution of 0.1 mol L^{-1} Qu in $CDCl_3$ as a function of c_{DPP}. Symbols show experimental data and error bars were estimated to ±0.05 ppm to account for systematic errors due to medium effects (see text). The molecular structure of Qu together with the proton labels are shown as inset in panel b). Solid lines show fits of eq. (5.3) to the data with a fixed value of K_1 = 100 L mol^{-1} (solid black line), 1000 L mol^{-1} (solid red line), and 10000 L mol^{-1} (solid blue line), demonstrating the correlation of K_1 with the other adjustable parameters when fitting eq. (5.3) to the data.

This variation of the chemical shift can be modelled by assuming two association equilibria, while neglecting other potential forms of aggregates: The association of DPP and Qu to form an ion-pair (IP) with equilibrium constant K_1 eq. (5.1) and the aggregation of an additional DPP molecule to an IP to form a multimer (M) with K_2 eq. (5.2):

$$K_1 = \frac{[\mathrm{IP}]}{[\mathrm{Qu}] \cdot [\mathrm{DPP}]} \tag{5.1}$$

$$K_2 = \frac{[\mathrm{M}]}{[\mathrm{IP}] \cdot [\mathrm{DPP}]} \tag{5.2}$$

here $[j]$ (j = Qu, DPP, IP, or M) are the equilibrium concentrations of the formed species. The observed motionally averaged chemical shift of Qu's protons can be expressed as:

$$\delta = \delta_{\mathrm{Qu}} \cdot \frac{[\mathrm{Qu}]}{c_{\mathrm{Qu}}} + \delta_{\mathrm{IP}} \cdot \frac{[\mathrm{IP}]}{c_{\mathrm{Qu}}} + \delta_{\mathrm{M}} \cdot \frac{[\mathrm{M}]}{c_{\mathrm{Qu}}} \tag{5.3}$$

with δ_j the chemical shift of each species j**.** Together with mass conservation, this model can describe the experimentally determined values of δ very well (see red solid lines in Figure 5.1). However, the thus obtained parameters are highly correlated (see also Supporting Information, Figure 5.5): For instance, the experimental data can be almost equally well modelled, with an equilibrium constant K_1 increased (decreased) by one order of magnitude (blue and black solid lines in Figure 5.1). Because only the average signal of all Qu species is experimentally accessible, the change in the equilibrium constant can be compensated in the fit by a decrease (increase) of the value of δ_{IP}. The experimentally measured variation of δ is however not solely due to molecular association, but may also contain a variation due to medium effects.[134] Such medium effects, due to progressive substitution of the pure solvent by the added acid, are inevitable in a titration experiment and thus result in a systematic error when describing the data in Figure 5.1 with eq. (5.3).

To lift this ambiguity in modelling the NMR chemical shifts we use a second method that allows discriminating between the different species. We use DRS, which is sensitive to the rotational relaxation of molecular dipoles.[102] For the sample in the present study, the solvent, IPs, and Ms are the predominant dipolar species that contribute to the dielectric spectra (Note that DRS peak amplitudes scale with concentration and the squared electrical dipole moment, see eq. (5.6) in the SI. As such, the contribution of the rotational relaxation of free DPP and Qu to the spectra is negligible.[18]). The contribution of the three predominant dipolar species to the spectra can be disentangled via their relaxation time (i.e. peak position) in the DRS spectra, as the relaxation time scales with viscosity and hydrodynamic volume: The larger the volume of the rotating dipolar species, the longer its relaxation time, i.e., the lower its relaxation frequency.[51] For uncorrelated molecular motion, each relaxation give rise to a dispersion in the frequency dependent permittivity $\varepsilon'(\nu)$ and a peak in the dielectric loss spectrum $\varepsilon''(\nu)$.

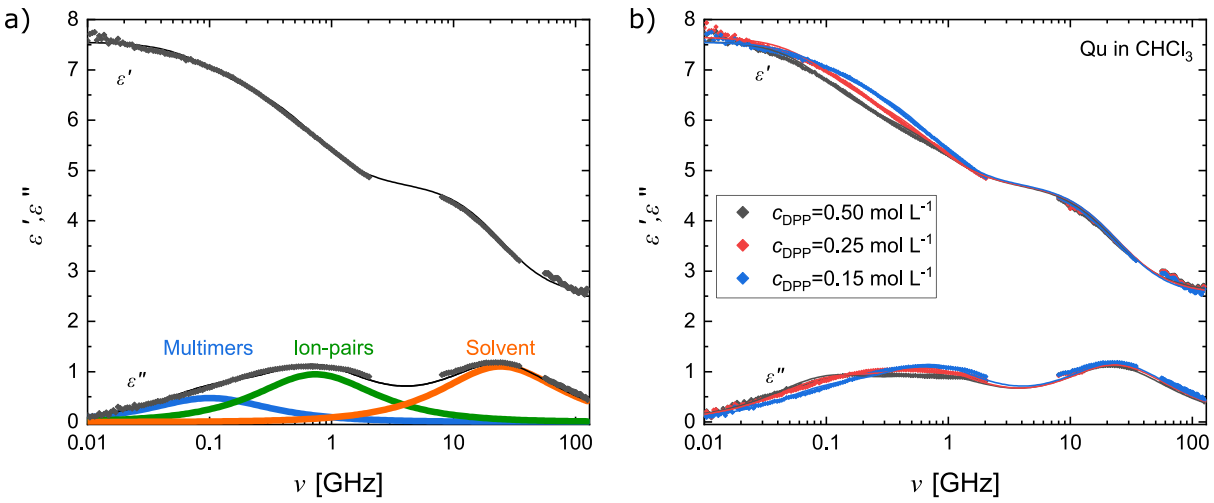

Figure 5.2 a) Dielectric permittivity, ε', and dielectric loss, ε'', spectra for a solution of c_{Qu}=0.1 mol L^{-1} and c_{DPP}=0.15 mol L^{-1} in $CHCl_3$. Symbols show experimental data and solid lines show the fit using three Debye-type relaxations. The contribution of the three Debye relaxations to the dielectric loss are shown as thick solid lines (blue: multimers, green: ion-pairs, orange: solvent). Panel b) shows the experimental spectra (symbols) together with the fits (solid lines) for solutions in $CHCl_3$ with different concentrations of DPP (c_{Qu}=0.1 mol L^{-1}): A gradual shift of the solute relaxations to lower frequencies with increasing c_{DPP} indicates multimer formation at the cost of ion-pairs.

In Figure 5.2a we show the dielectric permittivity spectrum for a solution of Qu (0.1 mol L^{-1}) and DPP (0.15 mol L^{-1}) in $CHCl_3$. The permittivity spectrum shows a pronounced dispersion within the studied frequency range, and the dielectric loss spectrum exhibits an asymmetric, broad peak at lower frequencies and a somewhat narrower peak at high frequencies. A combination of three Debye-type relaxations describes the experimental spectra very well (black solid line in Figure 5.2a, and we therefore use this model to decompose the spectra into three relaxations (see SI, eq. (5.4)). The contributions of the three individual relaxations to $\varepsilon''(\nu)$ are shown as blue, green and orange lines in Figure 5.1a. The high-frequency relaxation centred at ~20 GHz can be assigned to the solvent.[135] Similar to our previous work, we assign the two relaxations at lower frequencies to ion-pairs (700 MHz) and multimers (~100 MHz), which both give rise to a broad feature at low frequencies.[74] Upon increasing DPP concentration the solvent relaxation at ~20 GHz is rather unaffected (Figure 5.2b). Conversely, the dielectric loss at ~700 MHz decreases, while the loss at ~100 MHz increases. This shift of the loss peak to lower frequencies is indicative of the formation of multimers at the cost of ion-pairs.

The relaxation amplitudes, S_j, as extracted from the relaxation model are directly related to concentration $[j]$ and squared electrical dipole moment ${\mu_j}^2$ of the species in solution (see eq. (5.6)).[18,58,74] Thus, in order to quantify the equilibrium concentrations of all species, their electrical dipole moment μ_j is required. Here, we extract the value of μ_M and μ_{IP} from the relaxation amplitudes S_M and S_{IP} for the sample with the highest concentration of DPP. This is achieved by assuming that all Qu in solution form either IPs or Ms, which can be justified given the five-fold excess of acid. Further, we assume $\mu_M = \mu_{IP}$, which is supported by our previous experiments and *ab initio* calculations.[18,74]

Thus, we extract the equilibrium concentrations [*IP*] and [*M*] from the dielectric relaxation strengths (see SI for details).

Using these dipole moments, we obtain the values of [*IP*] and [*M*] (eq. (5.6)). These concentrations are used to constrain the fit of the NMR chemical shifts with eq. (5.3). To this end, we use the DRS determined IP and M concentrations at three DPP concentrations. The solutions with an excess of DPP were selected in order to get sufficiently high relaxation amplitudes, above the instrumental noise. The concentration of DPP is chosen such to aim at [*IP*]>[*M*], [*IP*]≈[*M*], and [*IP*]<[*M*] for the three studied concentrations. Here, in contrast to our earlier study on Qu+DPP mixtures in DCM,[74] we perform a global fit to both, NMR and DRS results to determine association equilibria. As can be seen in Figure 5.3, such constrained fits describe both the NMR chemical shifts and the DRS detected concentrations well.

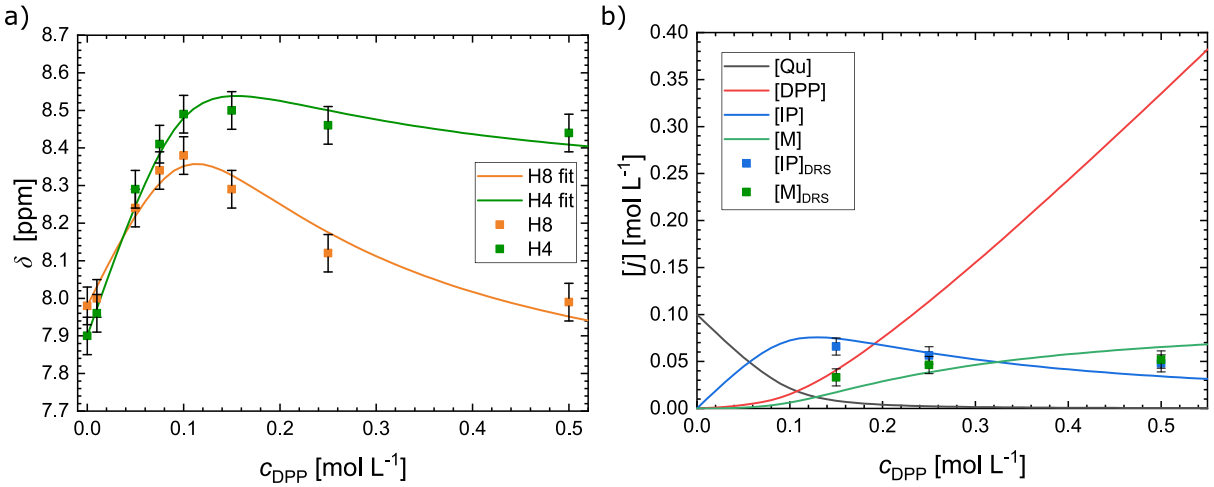

Figure 5.3 Combined fit of the NMR and DRS results in chloroform. All solutions contain 0.1 mol L^{-1} Qu. a) NMR chemical shift (symbols) of H4 and H8 and b) the concentrations of multimers and ion-pairs (symbols) as extracted from the DRS experiments. Solid lines in panel a) show the fit of the NMR chemical shifts according to eq. (5.3). Solid lines in panel b) show the concentration of all species according to the fitted equilibrium constants (eqs. (5.1) & (5.2)). Error bars in a) were estimated to ±0.05 ppm to account for the systematic error due to medium effects. The error bars in b) are calculated by propagation of error, based on an error in the DRS data of 2 % of ε_S.

5.3.1 Comparing different solvents

Using the methodology described above, we investigate the effect of the solvent on these equilibria for Qu and DPP (data for DCM are taken from ref. [74]). In Figure 5.4a-b we show the chemical shifts of H4 and H8 of Qu as a function of c_{DPP} in DCM, $CDCl_3$, and THF. These titration curves reveal already qualitative differences for the different solvents: The slope of the increase of δ for both protons at c_{DPP} <0.1 mol L^{-1}, where the formation of ion-pairs dominates, is highest for $CDCl_3$, while for the solvent THF the increase in δ is less steep. At high c_{DPP}, where multimers are formed to a significant extent, is the decrease of δ with increasing c_{DPP} is most pronounced for solutions in $CDCl_3$, while for solutions in THF the decrease of the shielding with increasing c_{DPP} is somewhat reduced.

To quantify the effect of the solvents on the association equilibria, we extract the values of K_1 and K_2 (see Figure 5.4), using the combined fit described above (solid lines in Figure 5.4, eq. (5.6), Figure 5.7 in the SI). We find the ion-pair formation constant (K_1) to be highest for chloroform, and similar, yet slightly lower for DCM. The here determined values in DCM are also in good agreement with our earlier study ($K_1^{\mathrm{DRS}} = 104$ L mol^{-1}, $K_2^{\mathrm{DRS}} = 16$ L mol^{-1}), where the association constants were determined using solely the DRS data.[74] In THF, we find the lowest value of K_1. Noteworthy, the variation of the K_1 values with solvent cannot be simply explained by the dielectric permittivity of the studied solvents. Based on the permittivity one would expect solvation of dipolar ion-pairs (and ionic species) to be most favourable in DCM, which has the highest dielectric constant, ε, of all three solvents (DCM: ε = 8.9, THF: ε = 7.4, $CHCl_3$: ε = 4.7)[136]. Hence, our results suggest that the stabilization of highly dipolar ion-pairs by the solvent is not the main factor determining solvent effects on the association equilibria. In turn, differences in the solvation of the reactants, Qu and DPP, may give rise to the observed trends. Indeed, we find that the values of K_1 are correlated with the hydrogen-bonding energy as determined by the Hansen solubility parameter, δ_h:[137] THF exhibits the highest value of δ_h = 3.9 cal.$^{-1/2}$ cm$^{3/2}$, while DCM and $CHCl_3$ exhibit lower δ_h values of 3.0 and 2.8 cal.$^{-1/2}$ cm$^{3/2}$, respectively.[137] Given that DPP can both accept and donate strong hydrogen bonds, our results indicate that solvent effects on the ion-pair formation equilibrium are governed by the solvation of DPP.

The thus determined values for K_2, for Qu as base, are less intuitive: we find K_2 to be largest in DCM, while the determined multimer formation constants are somewhat lower in THF and chloroform. We note that our model is only taking trimer formation into account (eq. (5.2)), while in solution different aggregates with possibly different conformation may be present. Within our model, all aggregates larger than ion-pairs are subsumed in extracted values of K_2. Within this model, our results suggest that apparently not only the solvation of DPP influences the formation of multimers, but also the solvation of the ion-pairs and multimers subtly affects K_2.

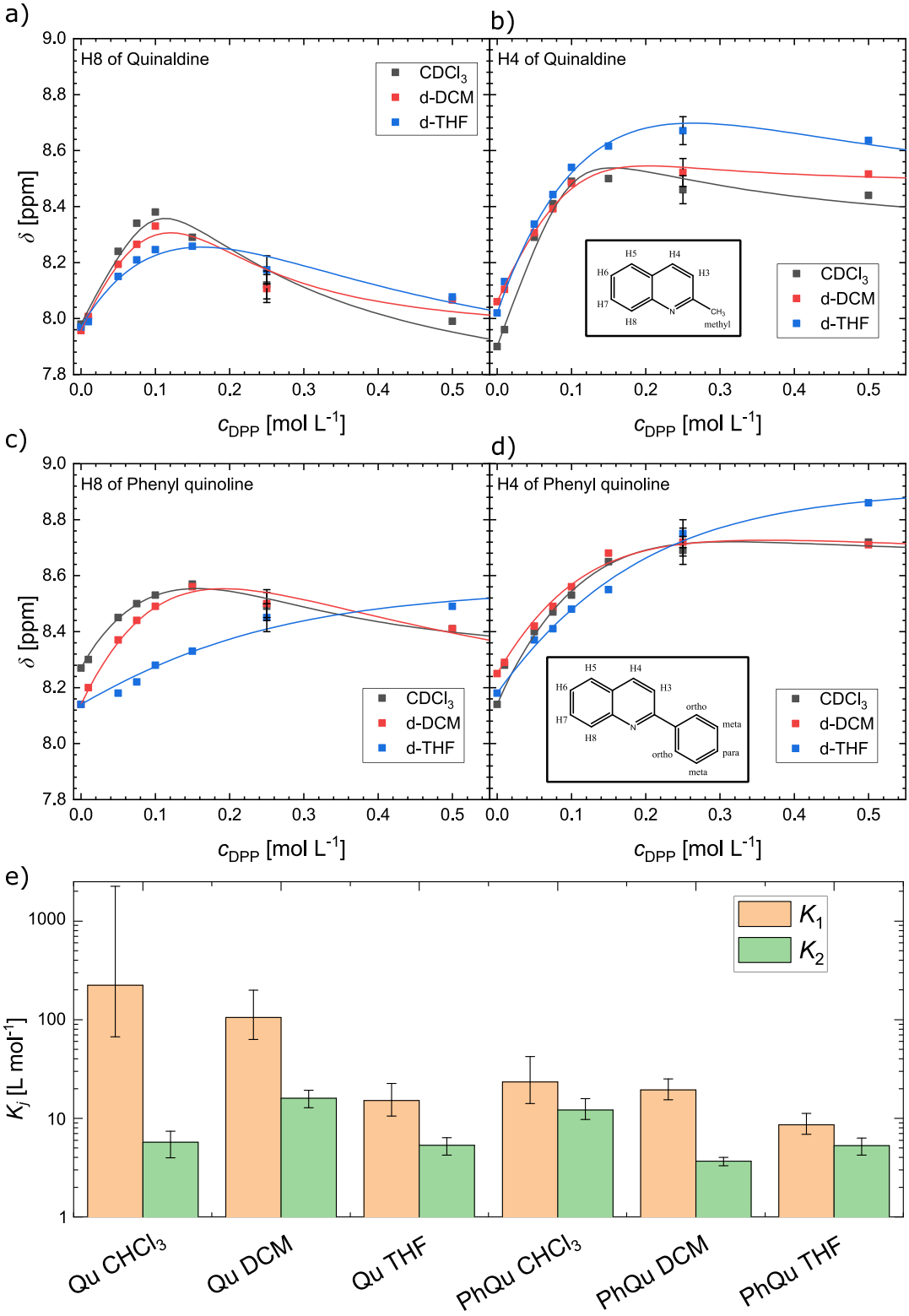

Figure 5.4 Chemical shifts of a) H8 of Qu, b) H4 of Qu , c) H8 of PhQu and d) H4 of PhQu for solutions of Qu or PhQu (0.1 mol L^{-1}) as a function of c_{DPP}. Symbols show experimental data. All errors in a)-d) were estimated to be ±0.05 ppm in order to account for systematic errors due to medium effects (see text). For sake of clarity, the error bars, which are equal for all data points, are only shown for one concentration. Data for DCM in panels a) & b) are taken from ref. [74]. Solid lines show the combined fit of the NMR data and the DRS data (eq. (5.6)). Insets of panel b) and d) display the molecular structures of Qu and PhQu, respectively. e) Equilibrium constants, K_1 and K_2, as obtained from the combined NMR and DRS fit. The error bars of the equilibrium constants represent a correlated error, based on an increase of the sum of the squared deviations from both DRS and NMR data by 10%.

5.3.2 Comparing different imines

To explore the effect of the imine base on the solution equilibria, we performed the same set of experiments with 2-phenylquinoline (PhQu, see inset in Figure 5.4c. With its additional phenyl group, PhQu as a substrate has been shown to give higher enantiomeric excess in asymmetric catalysis.[138]

The chemical shift changes of H4 and H8 with c_{DPP} for PhQu are shown in Figure 5.4c&d. As can be seen from this figure, the overall shapes of the titration curves in DCM and chloroform resemble our findings for Qu. Yet, compared to Qu, the absolute variation of δ within the studied concentration range is somewhat smaller. This less pronounced de-shielding (as compared to Qu) upon addition of DPP, can be explained by a reduced charge transfer from DPP to PhQu and/or a higher degree of delocalization of the positive charge upon interaction with DPP. In contrast to our findings for Qu, where the maximum δ values for H8 are observed for equimolar mixtures, the maximum in the chemical shift for H8 of PhQu in $CDCl_3$ and DCM is only reached for solutions with a slight excess of DPP. This shift of the maximum of the titration curve is indicative of different multimer formation equilibria relative to the ion-pair formation constants. For excess of DPP, we find the chemical shift of H4 to plateau, while the chemical shift of H8 decreases. This suggests, that formation of multimers predominantly affects the local chemical environment in the vicinity of PhQu's N atom. As opposed to Qu, more distant protons (e.g. H4) are rather insensitive to an excess of DPP (cf. multimer formation). As such, our results suggest that multimer formation does not alter the charge distribution of PhQu significantly and the electronic state of PhQu is similar in multimers and ion-pairs, in contrast to our observations for Qu.

Remarkably, the chemical shift of both H4 and H8 of PhQu in THF increases much less steeply as compared to DCM and $CDCl_3$ and the NMR titration experiment exhibits a monotonic increase (Figure 5.4c-d) with increasing acid concentration. In contrast to our findings for Qu, for PhQu the chemical shifts do not fully plateau, even for a 5 fold excess of DPP. Thus, our results suggest that the association behaviour of DPP and PhQu in THF differs from the other studied systems. Based on only the NMR data, for PhQu in THF only one association equilibrium could be inferred. Yet, the dielectric spectra exhibit the signatures of IP and M (see Figure 5.6, SI): With increasing c_{DPP} the intensity of the low-frequency relaxation increases. Hence, our results suggest that also for PhQu in THF both ion-pairs and multimers with DPP are formed. However, the concentrations of both species vary similarly with c_{DPP} (see Figure 5.8, SI).

Using the combined DRS and NMR analysis described above, we extract the association constants K_1 and K_2 for PhQu, which are shown in Figure 5.4e. In general, we find lower values of K_1 for PhQu as compared to Qu in all studied solvents. This trend is in line with the higher basicity of Qu relative to PhQu, as estimated from their aqueous pKb values.[139,140] The somewhat reduced interaction of PhQu with DPP, compared to Qu, is also broadly consistent with previous findings that a larger difference between the acidity of organo-phosphate Brønsted acid catalysts and the basicity of the imine results in higher reaction rates.[115] Similar to Qu, we find the lowest K_1 value for PhQu in THF and the effect of the solvent correlates with the solvent's hydrogen-bonding affinity δ_h. The K_2 values are similarly low for PhQu in all three solvents. Thus, K_2 is rather independent

of the solvent and of the ion-pair formation constant K_1. For PhQu in THF, K_1 and K_2 are thus rather similar, which leads to the rather featureless titration curves in the NMR experiments (Figure 5.4c-d).

Relating our findings to catalytic performance of organo-phosphate Brønsted acid, our results are in line with our previous notion that the ion-pair formation (K_1) is not decisive for enantioselectivity: In asymmetric catalysis the enantiomeric excess is similar in chloroform, DCM, and THF, despite the markedly reduced value of K_1 in THF.[18] As we have found previously,[18] dissociation of ion-pairs into free ions makes the enantioselectivity to diminish.[18] Our results show also no correlation between catalytic activity and multimer formation (K_2), which may be not surprising as in catalysis an excess of base is used and multimers will be a very minor species. Conversely, we find K_1 to scale with the yield obtained in catalysis: The observed lower yields in organo-phosphoric acid catalysed hydrogenations for PhQu in THF compared to DCM and $CHCl_3$,[117] correlate with the lower value of K_1 in THF, as compared to DCM and chloroform, for both Qu and PhQu. Hence, our results suggest that the ion-pair formation constant, which has been shown to determine the reaction rate,[115] plays an important role in the overall conversion. This suggests that a high ion-pair formation constant can help to prevent incomplete or undesired chemical conversion in these hydrogenation reactions.

5.4 Conclusion

We present a combined approach to obtain association equilibria of acids and bases from NMR and DRS data experiments. We use the NMR chemical shift, which is very sensitive to the variation of the chemical environment of the base, especially at low acid concentrations. DRS is used to discriminate different aggregates in solution, in particular at higher acid concentrations. Thus, we avoid a potential bias, which can be present when both experiments are used individually: Using only NMR data, the obtained equilibria may be biased due to medium effects, in particular at high solute concentrations.[134] Equilibria determined by using only DRS may suffer from low sensitivity at low concentrations, where relaxation amplitudes are generally weak (the accuracy of the determined relaxation strength is typically a few percent (~2%)[141] of the static dielectric constant).

We use this combined approach to study the association of organo-phosphoric acids and quinoline derivatives as bases in the solvents DCM, $CHCl_3$, and THF, which are relevant to organocatalysis. We find, in all studied solvents, the formation of ion-pairs, i.e. aggregates of a protonated imine base and a deprotonated phosphoric acid. The association constants for ion-pair formation are similar in DCM and $CHCl_3$ and markedly reduced in THF. The ion-pair formation constants correlate with the hydrogen-bonding properties of the solvents, suggesting that solvation of the phosphoric acid critically affects the association equilibria. These association equilibria also correlate with the yields of organocatalytic reactions, where THF has been reported to provide low yields,[20,117] while the solvents DCM and $CHCl_3$ provide excellent conversion.[6,13,16,20,117] Hence, our results

suggest that high ion-pair formation constants are necessary for efficient catalytic conversion.

At elevated acid concentrations, multimers consisting of one base and more than one acid molecule are formed. While there is no correlation of the multimer formation constant K_2 with catalytic conversion, it is important to take multimer formation into account in order to reliably determine ion-pair formation constant K_1, as both species coexist over a wide range of molar compositions.

5.5 Supporting information

5.5.1 Correlation of NMR chemical shift fit parameters

As described in the main manuscript, variation of the association constant K_1 can be – predominantly – compensated by a variation of the chemical shift of the ion pair, δ_{IP}, when fitting eq. (5.3) to the experimentally determined chemical shifts of Qu's protons. That is, K_1 and δ_{IP} are correlated. This is illustrated in Figure 5.5, where we show the variation of δ_{IP} when fitting eq. (5.3) to the data for Qu in $CDCl_3$ for different values of K_1.

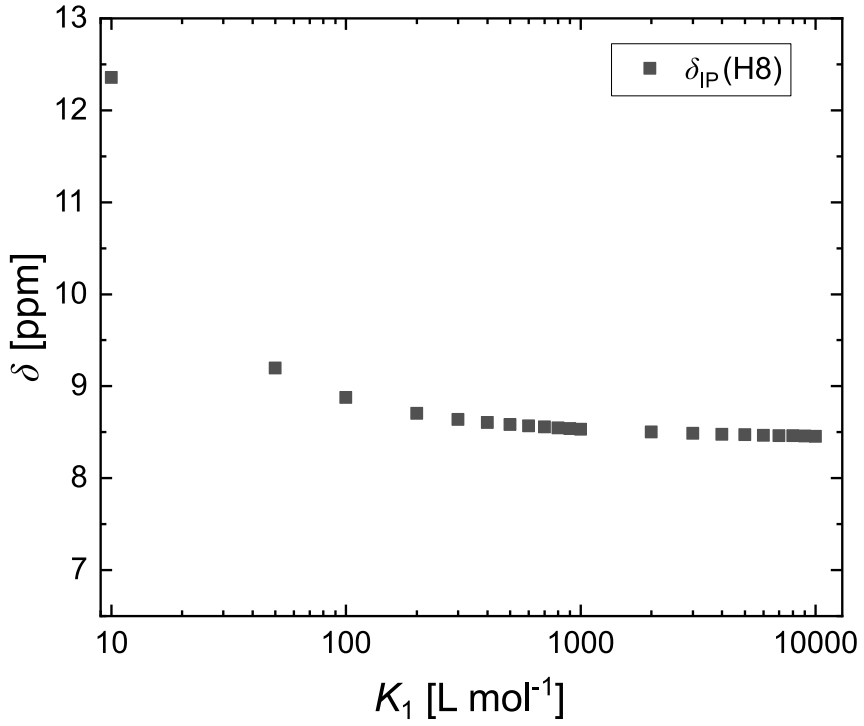

Figure 5.5 Chemical shift of the ion-pairs, δ_{IP}, as obtained from fitting eq. (5.3) to the data shown in Figure 5.1. Here, we keep K_1 constant, while all other parameters remain adjustable when fitting eq. (5.3) to the data. Selected fits are shown as solid lines in Figure 5.1 of the main manuscript.

5.5.2 Quantitative analysis of the dielectric spectra

In order to quantify the concentration of ion-pairs and multimers in solution, we analyse the dielectric spectra of the imine – DPP mixtures. Therefore, we fit a relaxation model to the experimental spectra. In line with our previous study, we find that a combination of three Debye type equations[74] excellently describes the experimental spectra (see also Figure 5.2). In this model the relaxation of the multimers (M), ion-pairs (IPs), and the solvent (solv) is each modelled with a separate Debye relaxation. Each relaxation is characterized by its relaxation strength (S_j) and relaxation time (τ_j). Using this model, we assume uncorrelated dipolar relaxation of the different molecules and/or molecular aggregates. All polarizations at frequencies (ν) higher than the experimentally covered frequency range are modelled by the limiting permittivity at infinite frequencies, ε_∞. Ohmic losses due to translational polarization are taken into account by the last term of eq. (5.4), with the d.c. conductivity κ assumed to be real and independent of frequency. ε_0 is the vacuum permittivity:

$$\hat{\varepsilon}(\nu) = \frac{S_\mathrm{M}}{1 + 2\pi \boldsymbol{i} \nu \tau_\mathrm{M}} + \frac{S_\mathrm{IP}}{1 + 2\pi \boldsymbol{i} \nu \tau_\mathrm{IP}} + \frac{S_\mathrm{solv}}{1 + 2\pi \boldsymbol{i} \nu \tau_\mathrm{solv}} + \varepsilon_\infty + \frac{\kappa}{2\pi \boldsymbol{i} \nu \varepsilon_0} \tag{5.4}$$

Based on the Cavell equation:

$$\frac{2\varepsilon_\mathrm{s} + 1}{\varepsilon_\mathrm{s}} \cdot S_j = \frac{N_\mathrm{A}[j]}{k_\mathrm{B} T \varepsilon_0} \cdot {\mu_j}^2 \tag{5.5}$$

the obtained relaxation amplitudes, S_j are directly related to concentration of the species, $[j]$, in solution[18,58,74] and their (squared) electrical dipole moment, μ_j. In eq. (5.5), $\varepsilon_\mathrm{s} (= S_\mathrm{M} + S_\mathrm{IP} + S_\mathrm{solv} + \varepsilon_\infty)$ is the static dielectric constant, N_A Avogadro's constant, k_B the Boltzmann constant, and T the thermodynamic temperature.

Accordingly, to relate the observed relaxation strengths to the concentration of the relaxing species, their electrical dipole moment is required. Here we assume the dipole moment of the ion-pair and of the multimer to be the same $\mu_\mathrm{IP,M} = \mu_\mathrm{IP} = \mu_\mathrm{M}$. This assumption is supported by *ab initio* calculations and experiments for DPP-Qu aggregates in DCM, which both indicate very similar dipole moments for both species.[74] Further *ab initio* calculations (DFT[142–144] / B3LYP 6-31+G(d)[145–147] as implemented in Gaussian 09[148]) for Qu-DPP ion-pairs and Qu-$(DPP)_2$ trimers in continuum solvents (PCM) suggest very similar dipole moments in the other studied solvents: $CHCl_3$ (μ_IP = 14.4 D, μ_M = 13.1 D), THF (μ_IP = 15.0 D, μ_M = 15.0 D).

Given that all imine bases form either ion-pairs or multimers ($c_\mathrm{Qu} \approx [\mathrm{IP}] + [\mathrm{M}]$), which can be justified for an excess of DPP, $\mu_\mathrm{IP,M}$ is obtained from the analytical concentration of base and from the combined relaxation strength $S_\mathrm{IP,M} = S_\mathrm{IP} + S_\mathrm{M}$ using eq. (5.5). Here,

we use the spectra with a five-fold excess of DPP to determine the dipole (see Table 5.1). This value allows obtaining the equilibrium concentrations [IP] and [M] from the experimental S_{IP} and S_{M} values (eq. (5.5)), respectively, at all three studied concentrations of each measurement series.

Table 5.1 shows the calculated combined dipole moments for ion-pairs and multimers.

Solvent	$\mu_{\mathrm{IP,M}}$(Qu) [D]	$\mu_{\mathrm{IP,M}}$(PhQu) [D]
DCM	23.6	25.2
$CHCl_3$	19.2	23.3
THF	20.8	23.9

5.5.3 Combined DRS and NMR fit

As described in the main manuscript, we perform a combined fit of the experimental chemical shifts for H8 ($\delta(\mathrm{H8})_{\mathrm{exp}}$) and H4 $\delta(\mathrm{H4})_{\mathrm{exp}}$ and the experimental concentrations of ion-pairs $[\mathrm{IP}]_{\mathrm{DRS}}$ and multimers $[\mathrm{M}]_{\mathrm{DRS}}$ based on the association equilibria as outlined in eqs. (5.1) & (5.2) of the main manuscript. To model the chemical shift of both protons we use eq. (5.3) (main manuscript). In the combined fit, we optimize the weighted sum of the square deviations from both experiments:

$$\chi = \frac{\sum\left(\left(\delta(\mathrm{H8})_{\mathrm{exp}} - \delta(\mathrm{H8})_{\mathrm{fit}}\right)/\Delta_{\mathrm{NMR}}\right)^2}{N_{\mathrm{NMR}}} + \frac{\sum\left(\left(\delta(\mathrm{H4})_{\mathrm{exp}} - \delta(\mathrm{H4})_{\mathrm{fit}}\right)/\Delta_{\mathrm{NMR}}\right)^2}{N_{\mathrm{NMR}}} + \frac{\sum\left(\left([\mathrm{M}]_{\mathrm{DRS}} - [\mathrm{M}]\right)/\Delta_{\mathrm{M,DRS}}\right)^2}{N_{\mathrm{DRS}}} + \frac{\sum\left(\left([\mathrm{IP}]_{\mathrm{DRS}} - [\mathrm{IP}]\right)/\Delta_{\mathrm{IP,DRS}}\right)^2}{N_{\mathrm{DRS}}} \quad (5.6)$$

where N_{NMR} and N_{DRS} are the number of data points of the NMR and the DRS experiments. Δ_{NMR}, $\Delta_{\mathrm{M,DRS}}$, and $\Delta_{\mathrm{IP,DRS}}$ are the errors in δ_{exp}, $[\mathrm{M}]_{\mathrm{DRS}}$, and $[\mathrm{IP}]_{\mathrm{DRS}}$, respectively. χ is optimized using, δ_{IP}, δ_M, K_1, and K_2 as adjustable parameters. For the value of δ_{Qu} we take the value from the experiments at $c_{\mathrm{DPP}} = 0$.

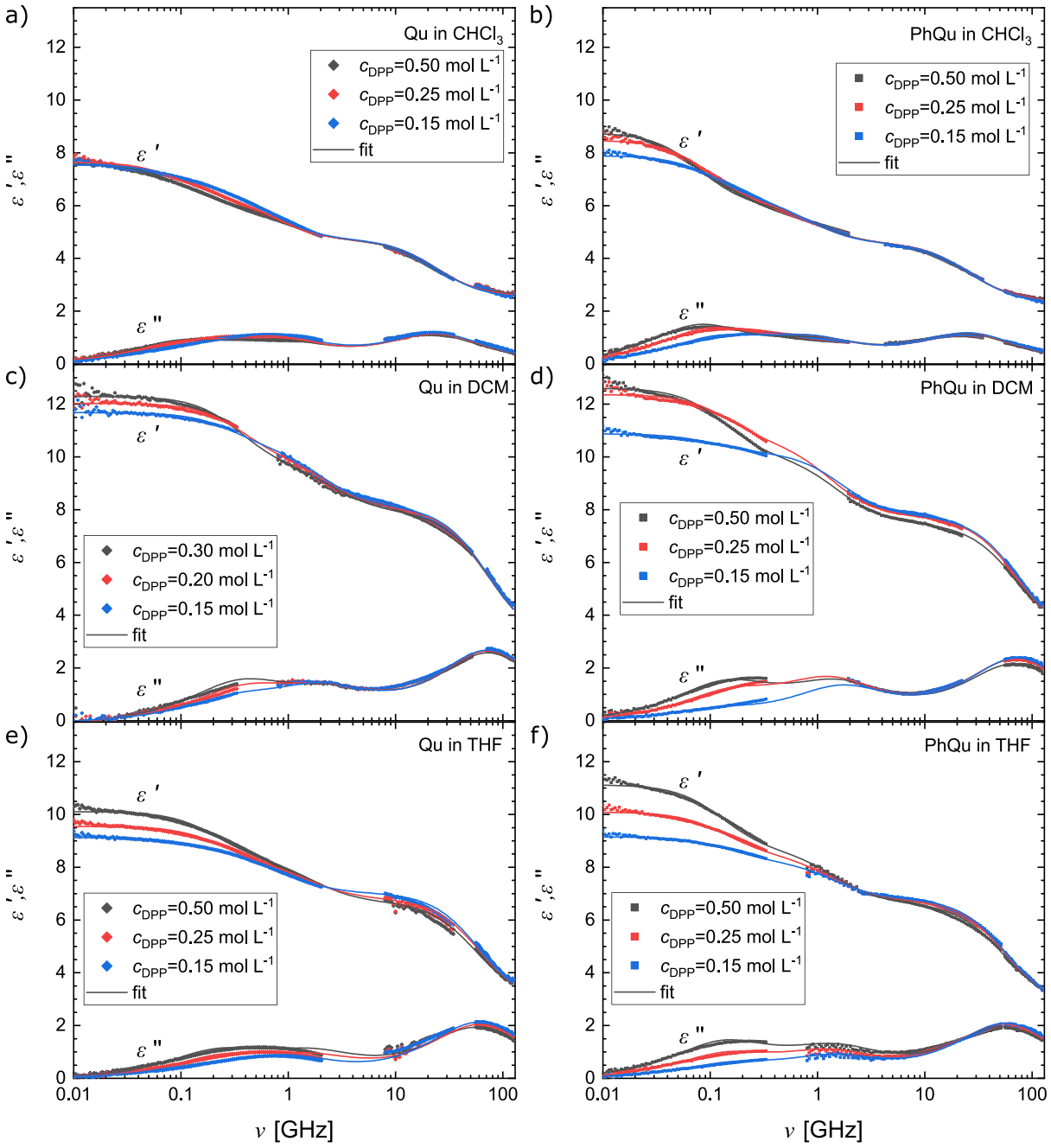

Figure 5.6 DRS spectra for (a, c, e) Qu and (b, d, f) PhQu in (a, b) DCM, (c, d) $CHCl_3$, and (e, f) THF. The imine concentration is kept constant at 0.1 mol L^{-1} in all samples. The data shown in a) are taken from ref [74]. Symbols correspond to experimental spectra, solid lines show fits of eq. (5.4) to the data.

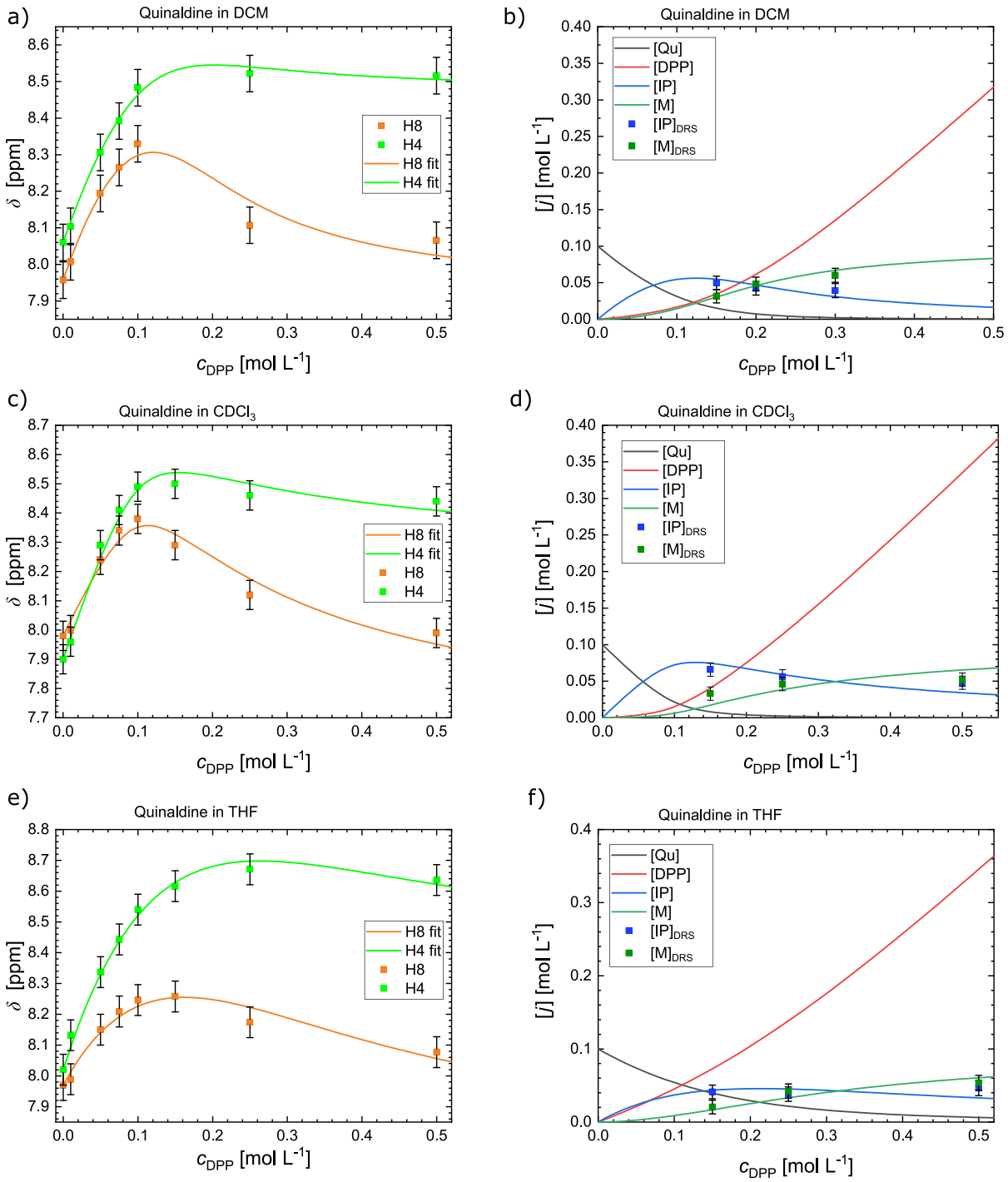

Figure 5.7 Combined fit of the NMR and DRS results for Qu (c_{Qu} = 0.1 mol L^{-1}) in (a, b) DCM, (c, d) chloroform, and (e, f) THF. (a, c, e) NMR chemical shift (symbols) of H4 and H8 together with the fits (solid lines) according to eq. (5.3). Error bars are estimated to ±0.05 ppm to account for the systematic error due to medium effects. (b, d, e) concentration of multimers and ion-pairs (symbols) as extracted from the DRS experiments together with the concentration of all species (solid lines) according to the fitted equilibrium constants (eqs. (5.1) & (5.2)). Error bars are calculated by propagation of error, based on an error in the DRS data of 2 % of ε_s.

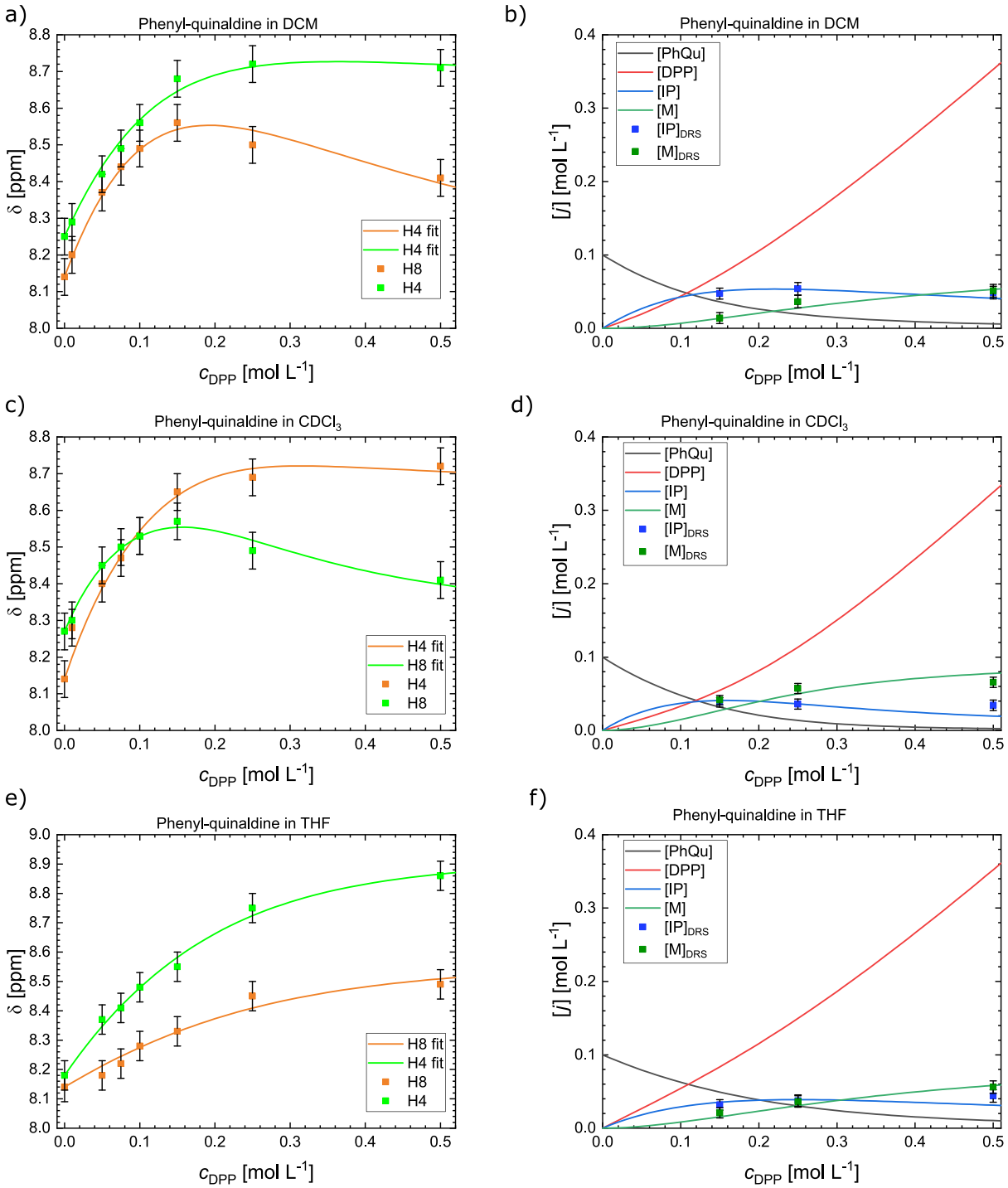

Figure 5.8 Combined fit of the NMR and DRS results for PhQu (c_{PhQu} = 0.1 mol L^{-1}) in (a, b) DCM, (c, d) chloroform, and (e, f) THF. (a, c, e) NMR chemical shift (symbols) of H4 and H8 together with the fits (solid lines) according to eq. (5.3) (main manuscript). Error bars are estimated to ±0.05 ppm to account for the systematic error due to medium effects. (b, d, e) concentration of multimers and ion-pairs (symbols) as extracted from the DRS experiments together with the concentration of all species (solid lines) according to the fitted equilibrium constants (eqs. (5.1) & (5.2), main manuscript). Error bars are calculated by propagation of error, based on an error in the DRS data of 2 % of ε_s.

6 Vibrational dynamics of doubly ionic hydrogen-bonded Brønsted acid-base pairs and multimers

This manuscript is submitted to PCCP.

This project has received funding from the European Research Council (ERC) under the European Union's Horizon 2020 research and innovation program (grant agreement No 714691). B.M. gratefully acknowledges financial support from Alexander von Humboldt foundation.

6.1 Introduction

Aggregates formed via association of a Brønsted acid and a Brønsted base are often considered as prototypes of strong hydrogen bonds.[149] The relevance of strong hydrogen bonds to e.g. photochemical transfer cascades in biological systems,[150,151] enzyme function,[152] or catalysis[9,11,153] has triggered intense interest in understanding of their fundamental physical and chemical characteristics.[90,154–157] Of particular interest are such strong hydrogen bonds for fast (photo-) chemical reactions, which go along with the transfer of the proton within such strong bonds.[151] Most of the current understanding of these strong hydrogen bonds stems from studies of carboxylic acids.[35,87,158,159] Dynamics of strong hydrogen bonds involving phosphoric acid groups, as they occur in enzymatic transition[152] states or in asymmetric catalysis,[9] are less well understood.[27]

Two limiting cases are usually considered for aggregation of a Brønsted acid with a Brønsted base: a neutral hydrogen bond with the acidic proton remaining located at the acid or a doubly ionic hydrogen bond (a strongly hydrogen-bonded ion-pair), which is formed by transfer of the proton from the acid to the base.[17,90,160,161] For example, the interaction between organo phosphoric acids and imines was initially described as coexistence of these two limiting cases.[25] However, in recent years there has been evidence that proton transfer and subsequent ion-pair formation (doubly ionic hydrogen bond) dominate.[18,74,95] Yet, our previous studies have revealed an even more complex association behaviour in the dipolar aprotic solvent dichloromethane: even for equimolar mixtures of phosphoric acids with imine bases, not only bimolecular aggregates (ion-pairs, Figure 6.1a) between the acid and the base are formed but also multimers, in which a phosphoric acid donates a hydrogen bond to the deprotonated acid anion of an ion-pair (Figure 6.1).[18,74] Conceptually, this multimer formation can be interpreted as an acid homodimer (Figure 6.1c), which are commonly observed for such mixtures,[162–164] protonating the imine base. These findings were however largely based on rather 'slow' experimental methods (nuclear magnetic resonance (NMR) and dielectric relaxation spectroscopies (DRS)), which typically provide information on the average charge and/or proton distribution.

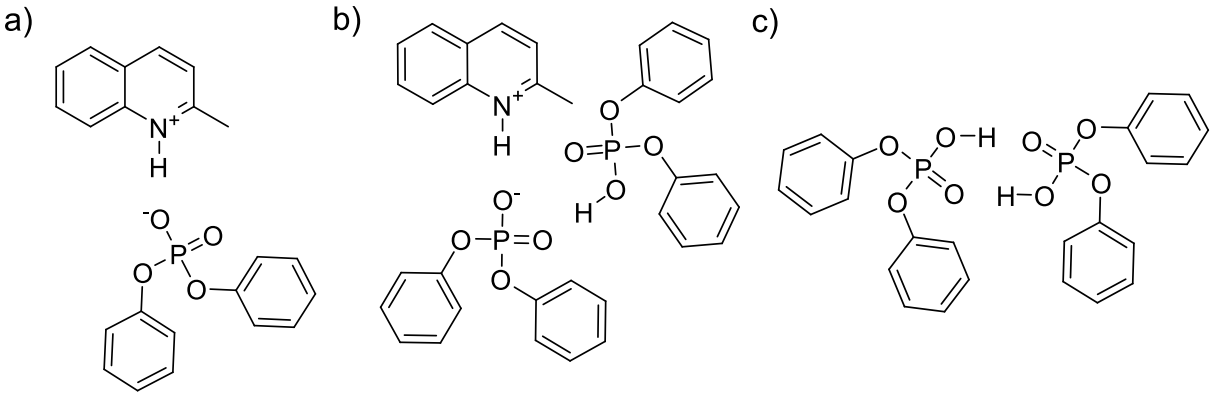

Figure 6.1 a) Structure of an ion-pair consisting of one Qu and one DPP molecule. b) For the simplest multimeric structure, i.e. a trimer, an additional DPP molecule donates a hydrogen bond to the acid anion. In panel c) a DPP homodimer is schematically shown.

For catalysis, the interaction strength and the hydrogen bond dynamics for the individual aggregates (dimers or multimers) are crucial, as proton transfer has been suggested to constitute, at least in part, the reaction coordinate.[165] Also the bond strength is relevant to asymmetric catalysis, as strong bonding can restrict the number of thermally accessible conformations of the base.[21,95] Conversely, the bonding geometry has to be sufficiently flexible in order to allow the Brønsted acid catalyst to reversibly bind a wide range of substrates.[93] As such, the location of the proton and bonding dynamics of the proton, which reports on the bond strength and geometry, affect the catalytic efficiency, yet the molecular details have remained somewhat elusive.[165]

In principle, the nature and strength of strong bonds can be traced by linear (and non-linear) infrared (IR) spectroscopies within individual aggregates. However, the anharmonic and flat potential along the proton transfer coordinate (e.g. as compared to a water-water hydrogen bond) together with strong anharmonic couplings, lead to complex infrared spectra[166] with the absorption bands spanning more than 1000 cm^{-1}. These broad bands can be structured and appear as several bands, which is caused by Fermi resonances with overtones and/or combination bands of stretch, bending and rocking modes.[160] The resulting reduced absorbance at a given frequency gives rise to a transmission window with reduced infrared absorbance, the so-called Evans hole.[30,38,166–170] For multiple Fermi resonances the broad absorbance can be even split into three main absorption features, so called A,B,C-type[39,154,166,171] spectra, which are common for strongly hydrogen-bonded systems[30] such as doubly ionic hydrogen-bonded systems. In principle, vibrational frequencies of the underlying molecular complexes have been shown to be a useful measure to predict catalytic activity of Brønsted acids,[22,23] yet the complexity of the experimental spectra make it challenging to relate the observed vibrations to molecular species in solution and to elucidate the underlying molecular bonding motifs and dynamics.

To experimentally capture the fast bonding dynamics of the intermolecular bond between acids and bases, ultrafast IR spectroscopy experiments are the method of choice. Though acid-base pairs containing phosphoric acids have – to the best of our knowledge – not been studied using ultrafast infrared spectroscopies, similar strongly bound

systems have been investigated by others: For strongly hydrogen-bonded systems with acetic acids, very rapid (tens to hundreds of femtoseconds) vibrational relaxation has been reported, which was rationalized by strong (anharmonic) coupling to lower frequency modes of the acid-base complex.[159,162] The energy released in the course of vibrational relaxation was suggested to be insufficient to weaken or dissociate the aggregates.[35,159,172] Moreover, experiments and simulations[90,173–176] have shown that coupling to the solvent critically affects the dynamics of the proton. Overall, the vibrational structure and dynamics of such acid-base pairs appears somewhat reminiscent of the structure and dynamics of the proton in aqueous solutions of Brønsted acids.[177–179]

Here we report on the vibrational dynamics of acid-base mixtures consisting of diphenyl phosphoric acid and the base quinaldine dissolved in dichloromethane, which are relevant to acid catalysed hydrogenation of quinaldine.[13,16] We find the broad infrared absorption of the phosphoric acid homodimers to red-shift upon addition of the base. *Ab initio* calculations suggest that the red-shift can be explained by a flatter potential along the proton transfer for hydrogen bonds in the presence of the base, as compared to the acid homodimer. Using IR pump-probe spectroscopy and two-dimensional IR (2D-IR) spectroscopy[44,47,180–182] to elucidate spectral dynamics of the doubly ionic hydrogen bonds, we find extremely fast (~100 fs) vibrational relaxation dynamics after vibrational excitation of the acidic proton. In the 2D-IR spectra, we observe a somewhat delayed appearance of a rather uncommon off-diagonal peak, most apparent for an excess of acid. We ascribe this off-diagonal signal to the population of lower energy states during vibrational relaxation, which – via strong anharmonic coupling – transiently modulate all hydrogen bonds within the formed molecular complexes. This coupling modulates both the doubly ionic hydrogen bond between an acid and a base and the singly ionic hydrogen bond formed between an acid and an acid anion in trimers, with the latter giving rise to the off-diagonal peak.

6.2 Experimental section

Diphenyl phosphoric acid (or diphenyl phosphate: DPP, 99 %) and quinaldine (Qu, 95 %), were purchased from Sigma-Aldrich. Dichloromethane (DCM, 99.9 %) was purchased from Fisher Scientific. To remove residual water from DCM and Qu, both liquids were dried over molecular sieves (4 Å). Prior to use, the liquids were filtered with a 0.2 mm Omnipore membrane filter (Merck) to remove solid residues from the molecular sieves. All samples were prepared by weight in volumetric glass equipment and subsequently sonicated for ~5 s. The samples were contained between two CaF_2 windows (4 mm thick) separated by a 25 µm PTFE spacer, except for infrared pump-probe experiments, where we used 2 mm thick CaF_2 windows separated by a 50 µm PTFE spacer. For infrared pump-probe and (2D-IR) spectroscopies the temperature was controlled to 22.0 ± 0.5 °C.

6.3 Results and discussion

6.3.1 FTIR spectra of DPP-Qu mixtures

To study the interaction between the acid and the base at different compositions, we measure FTIR spectra of DPP-Qu mixtures in DCM at a constant concentration of DPP (0.5 mol L^{-1}) and varying concentrations of Qu (0-1 mol L^{-1}). The infrared absorption spectrum of Qu in the 1700-2800 cm^{-1} spectral range (black line Figure 6.2a) shows no vibrational features in this spectral range. Solutions of only DPP (solid red line) exhibit a rather broad absorption spanning the full ~1000 cm^{-1} spectral range of Figure 6.2a. We assign this very broad absorption band to be due to DPP homodimers, similar to what has been reported to solutions of other Brønsted acids in aprotic solvents.[162,163] The remarkable width of such homodimer absorptions has been – besides different molecular conformations – related to strong coupling (anharmonic and excitonic) as well as Fermi resonances.[162]

Upon addition of the base Qu to the mixtures, we observe the emergence of two broad (more than 400 cm^{-1} wide), yet structured absorption features at ~2040 cm^{-1} and ~2500 cm^{-1} (Figure 6.2a). These two spectral features are separated by a minimum in the absorbance at ~2200 cm^{-1}, yet the absorbance does not fully vanish at this minimum. We note in passing that these spectral features correspond to the B (~2500 cm^{-1}) and C (2040 cm^{-1}) components of the A,B,C-type spectra common to strongly hydrogen-bonded systems, whereas the A feature is located around ~3400 cm^{-1} (see Figure 6.7, supporting information, SI).[30] Thus, similar to DPP homodimers, also doubly ionic ($O^{-}\cdots H\text{-}N^{+}$) hydrogen bonds,[17] which are the predominant intermolecular interaction motif for an excess of Qu (see e.g. blue solid line in Figure 6.1a), give rise to a very broad absorption in the infrared spectra spanning more than 1000 cm^{-1}.

Despite both, the neutral hydrogen bonds of DPP homodimers and the $O^{-}\cdots H\text{-}N^{+}$ hydrogen bonds of ion pairs, give rise to very broad absorption features, we find this broad absorption to depend on chemical composition. Upon increasing concentration of Qu the absorbance overall red-shifts, as can be seen from the composition-dependent infrared absorptions shown in Figure 6.2b: While the absorbance at blue-shifted frequencies decreases (2810 cm^{-1} in Figure 6.2b), the absorption at 2460 cm^{-1} increases by ~40 %, and at very red-shifted frequencies by ~90 % (2040 cm^{-1} in Figure 6.2b) with increasing Qu concentration. At 2220 cm^{-1} the absorbance decreases with increasing Qu. Noteworthy, the minimum in the absorbance at ~ 2220 cm^{-1} (at the so-called Evans hole[168]) is only apparent for samples containing Qu. This suggests that the reduced absorbance at 2220 cm^{-1} results from a Fermi resonance[162] with a vibrational mode of Qu. Figure 6.2b shows that the shift of the broad absorbance to lower frequencies is most pronounced for an excess of DPP, where our previous study evidenced the coexistence of ion-pairs and multimers.[74] Thus, gradual variation of the contribution of electroneutral hydrogen bonds within DPP homodimers, singly ionic hydrogen bonds between DPP and a DPP anion within multimers, and doubly ionic hydrogen bonds between DPP and Qu with composition give rise to the shift of the broad IR absorption feature.[74] For an excess of base, where ion-pairs Figure 6.1a prevail,[74] the spectral contributions as shown in Figure 6.2b plateau for increasing Qu concentration.

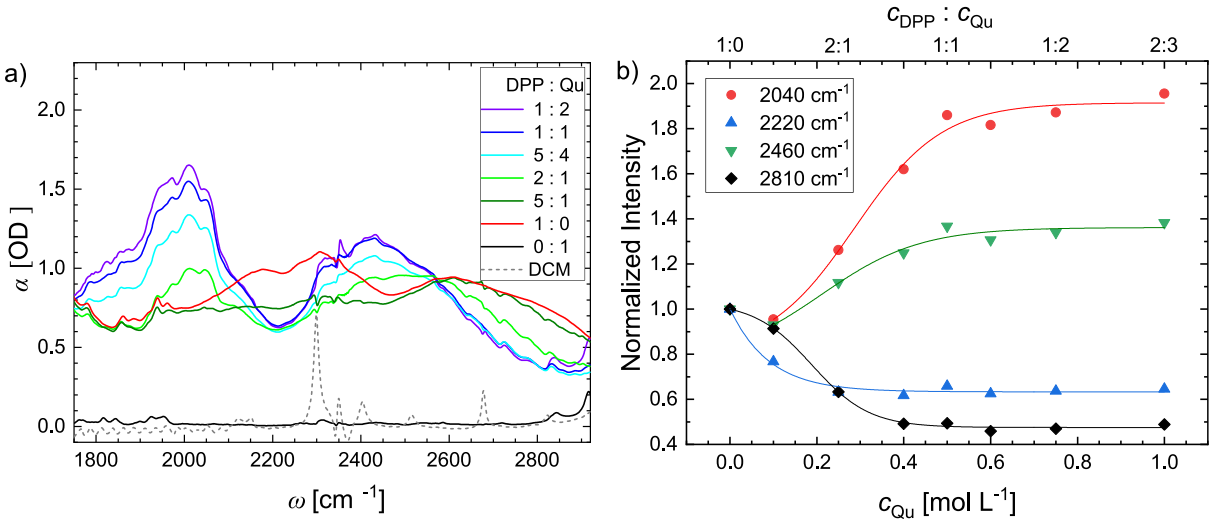

Figure 6.2 a) FTIR spectra for mixtures of DPP and Qu in DCM with varying Qu concentration. For all samples the concentration of DPP was kept constant at 0.5 mol L^{-1}. The spectrum of Qu in DCM (solid black line) shows essentially no spectral features in this frequency region. A solution of DPP in DCM (red solid line) exhibits a very broad band spanning more than 1000 cm^{-1} due to DPP-DPP homodimers. In mixtures of DPP and Qu two structured spectral features at ~2040 cm^{-1} and ~2500 cm^{-1} are observed. Note that contributions of the solvent (dotted grey line) have been subtracted from the mixture spectra. b) Normalized infrared absorbance of DPP-Qu mixtures at selected frequencies for solutions of 0.5 mol L^{-1} DPP as a function of c_{Qu}. Symbols are experimental data, lines are mere guides to the eye. Upon addition of Qu, spectral intensity at blue-shifted frequencies (2810 cm^{-1}) decreases, while the absorbance at 2460 cm^{-1} and 2040 cm^{-1} increases. Hence the overall spectral intensity red-shifts, except for the absorption at 2220 cm^{-1}, where a spectral minimum appears with increasing concentration of Qu.

6.3.2 Proton transfer potentials

The rather low (as compared to the ~3000-3500 cm^{-1} range for weaker hydrogen-bonded O-H and N-H stretching bands) resonance frequency observed here has been often related to the proton residing in a rather shallow and anharmonic potential[30]. Despite the experimentally observed broad and structured absorbance, which can obviously not be explained by considering only a single vibrational coordinate within one molecular conformation, the displacement of the proton along the proton transfer coordinate has been shown to be a good estimate for the overall position of the absorbance of the hydrogen bond in the vibrational spectra.[177–179]

To assess the resonance vibrational frequencies of the proton transfer for all conceivable hydrogen-bonding motifs illustrated in Figure 6.1, we calculate the potential energy landscapes for the proton transfer between the O (or N) atoms of DPP and Qu. To determine the potential of doubly ionic hydrogen bonds as in the ion-pairs and multimers (N-H^+···$^-$O, Figure 6.1a-b), of neutral hydrogen bonds as in the DPP homodimers (P-O···H-O-P, Figure 6.1c), and of singly ionic hydrogen bonds as in the multimers (P-O^-···H-O-P, Figure 6.1b), we perform *ab initio* calculations The *ab initio* calculations are performed for a Qu-DPP pair (IP), an electroneutral DPP-DPP pair, and an anionic DPP^--DPP pair with lithium as counterion. To this end, we perform density functional theory[142–144] calculations at the B3LYP-D3(BJ)/6-31G(d) level of theory[145–147] using Grimme's D3 dispersion with Becke-Johnson damping[183]. We use a polarizable continuum model for

DCM[184], as implemented in Gaussian 16.[185] Starting from an optimized geometry (Figure 6.8), a non-relaxed surface scan indeed indicates a very anharmonic potential upon translating the protons along the N--O (or O--O) axes (for details see Figure 6.3 and SI).

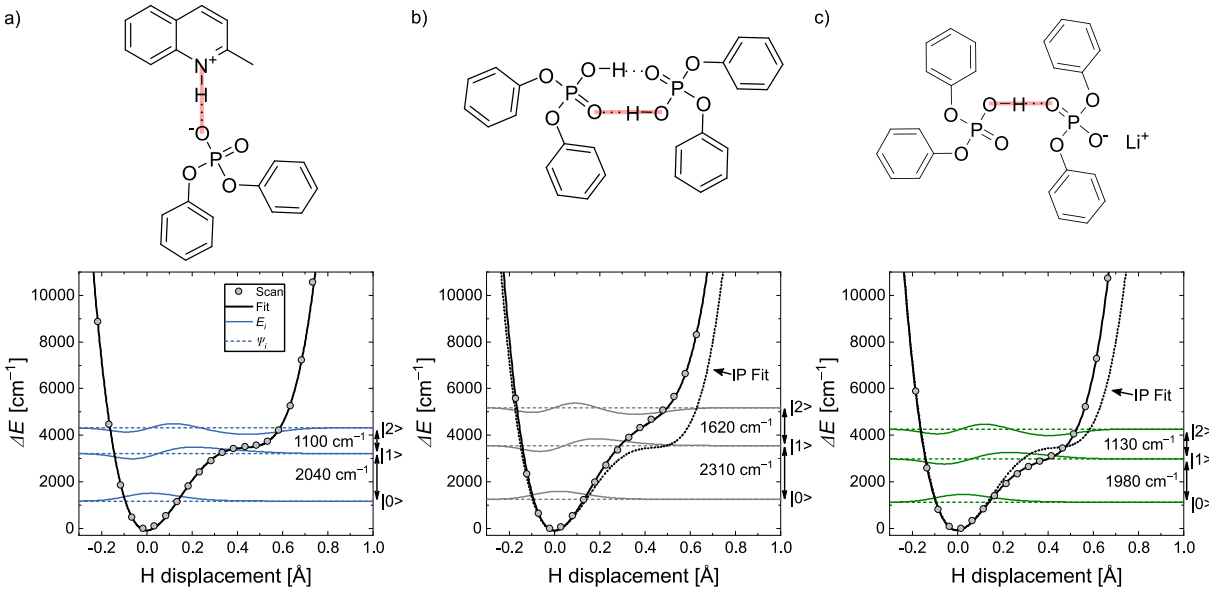

Figure 6.3 Potential energy profile along the proton transfer coordinate for hydrogen bonds between a) Qu and DPP, b) between two DPP molecules within a homodimer, and c) between DPP and a DPP$^-$ anion with lithium as counterion. Schematic molecular structures together with the proton transfer coordinate (shaded red lines) are shown on the top of each panel. Symbols correspond to relative energies as obtained from a non-relaxed energy scan for the hydrogen-bonding proton displaced along the N-O (or O-O coordinate) at the B3LYP-D3(BJ)/6-31G(d) level of theory[145–147] (DFT[142–144] using Gaussian 16[185]) with GD3BJ dispersion corrections[183] in a polarizable continuum solvent[184]. Black solid lines show quartic fits to the potential (see text and SI for details). For better comparison the potential shown in a) is shown as dotted line in panels b) and c). Energy levels of the three lowest eigenstates |0>, |1> and |2> obtained by numerically solving the one-dimensional Schrödinger equation are shown as dashed lines. The associated wave functions are depicted as solid lines and were vertically offset by the corresponding energies for clarity. Transition frequencies are highlighted with double-headed arrows.

For the doubly ionic hydrogen bond, the global minimum of the potential corresponds to the proton located close to the nitrogen (r(N-H) ≈ 1.1 Å in Figure 6.3a) and is separated by ~3000 cm^{-1} from the plateau close to DPP's oxygen (r(N-H) ≈ 1.5 Å in Figure 6.3). The overall shape of the potential with a pronounced minimum corresponding to the proton located close to the nitrogen atom of Qu in the vibrational ground state agrees well with the notion of the ion-pair nature of DPP-Qu dimers.[18,74] To relate this potential to the vibrational transitions, we fit the potential with a quartic asymmetric double-well function as described in ref. [179] (Figure 6.3). The corresponding one-dimensional nuclear Schrödinger equation based on the fitted potential was numerically solved, using the discrete variable representation method[186] (see ESI for details). The thus obtained wave functions of the three lowest-lying eigenstates together with their energies are shown in Figure 6.3. The first vibrational excited state for the ion-pair is energetically very close to the plateau, which corresponds to the proton back transfer to the oxygen atom of DPP. As such, the proton is significantly delocalized between the acid and the base in the first

vibrational excited state. The strong anharmonicity of the potential also results in a very large difference in transition energies between the lowest-lying states: |0>-|1> ~2040 cm^{-1} vs. |1>-|2> ~1100 cm^{-1}, with the fundamental transition in broad agreement with the experimentally observed bands for an excess of Qu in Figure 6.2a.

For the electroneutral hydrogen bond in DPP homodimers (Figure 6.3b), we find the proton transfer potential to be steeper, resulting in the vibrational transitions to be located at ~2470 cm^{-1} (|0>-|1>) and at ~1780 cm^{-1} (|1>-|2>). We note that for the slightly non-linear O-H-O bond of the DPP homodimers, the results are somewhat sensitive to the exact choice of the coordinate: translating the proton along the O-H axis results in higher transition frequencies of up to 160 cm^{-1} (see Figure 6.9), which may serve as an estimate for the uncertainty of the predicted transitions.

Overall, the thus calculated transition energies are in broad agreement with our experimental observation of an overall red-shift of the broad absorbance upon addition of Qu (Figure 6.2). In the absence of Qu, the DPP homodimers give rise to spectral contributions at higher frequencies, in line with the transition energy of the DPP-DPP homodimers (Figure 6.3b). For an excess of Qu, ion-pairs dominate, for which the proton transfer is suggested to give rise to spectral contributions as low as 2000 cm^{-1} (Figure 6.3a). Despite the experimental infrared spectra do not provide direct evidence for the formation of singly ionic hydrogen bonds, the gradual shift as shown in Figure 6.2b is consistent with such hydrogen bonds in trimers (Figure 6.1b) leading to spectral contributions at red-shifted frequencies (Figure 6.3c).

6.3.3 Vibrational dynamics

To further disentangle the vibrational modes underlying the FTIR spectra shown in Figure 6.2a, we perform 2D-IR experiments. In a 2D-IR experiment, the modulation of the infrared absorbance of the sample is probed (probe frequency, ω_{Probe}) as a function of (excitation) pump frequency, ω_{Pump}. Vibrational dynamics are detected by varying the delay time, t, between the pump and the probe pulse. Commonly, for each vibrational mode a pair of peaks is observed in the 2D-IR spectra: a negative peak on the diagonal ($\omega_{Pump} = \omega_{Probe}$) and a positive peak at red-shifted probe frequencies ($\omega_{Pump} > \omega_{Probe}$). The former results from ground-state depletion and stimulated emission, while the positive peak is due to excited state absorption of the anharmonic vibrational mode. Vibrational coupling (and/or chemical exchange/energy transfer) between distinct vibrational modes give typically rise to two instantaneous (or delayed) off-diagonal peaks. The position of such off-diagonal peaks is symmetric with respect to the diagonal.[44,47,48,182,187]

In Figure 6.4 we show the absorptive 2D-IR spectra for mixtures of DPP and Qu with varying molar ratios at t = 50 fs (see Figure 6.4a). In all spectra, we observe a bleaching signal on the diagonal, centred at 2040 cm^{-1}. Even at this early delay time (50 fs), the signal is already fairly round and we find no significant elongation along the diagonal. This round shape indicates that no inhomogeneous broadening is detectable within our spectral window and time resolution (~150 fs). Thus, the peak at 2040 cm^{-1} is either homogeneously broadened or – if also inhomogeneously broadened – spectral diffusion

is very fast. Despite the round shape of the on-diagonal peak at 2040 cm^{-1}, the overall transient signal is somewhat structured, with two minima on the diagonal at ~2010 cm^{-1} and ~2040 cm^{-1} (see diagonal cut in Figure 6.10). This structure is also observed in the FTIR spectra (Figure 6.2a). For similar strongly hydrogen-bonded dimers such structuring has been ascribed to Fermi resonances.[37,158,159] Remarkably, at all delay times we do not detect an excited state absorption adjacent to the bleaching signal at red-shifted probe frequencies. The absence of such detectable positive signals is in line with our *ab initio* calculations, which predict the excited state absorptions at ~1000 cm^{-1} (Figure 6.3). Additionally, a rapid relaxation of the first vibrational excited state, which will be discussed below, can result in a significant attenuation of the excited state absorption.

In contrast to the absence of a detectable off-diagonal peak due to the excited state absorption, we find at all molar ratios the predominant bleaching signal to be elongated towards higher probe frequencies: depending on molar composition a more or less intense blue-shifted bleaching signal at ($\omega_{\mathrm{Pump}}/\omega_{\mathrm{Probe}}$) (2040 cm^{-1}/2110 cm^{-1}) adjacent to the transient signal at the diagonal is present. The fact that we do not detect corresponding spectral intensity on the diagonal (2110 cm^{-1}/2110 cm^{-1}) suggests that the transition dipole moment of the modes giving rise to the signal at ω_{Probe} = 2110 cm^{-1} is too low to be directly excited in the 2D-IR experiment. Also the absence of a corresponding transient signal above the diagonal (symmetric with respect to the diagonal at (2110 cm^{-1}/2040 cm^{-1}) renders coupling, chemical exchange, or resonant energy transfer as origin of this feature unlikely as these mechanisms would lead to a second peak above the diagonal. Thus, the signal must rather have different origins. A possible explanation for the appearance of such transient bleaching signals only below the diagonal could be a transient modulation of vibrational modes in the course of vibrational relaxation: vibrational relaxation (transiently) populates lower-frequency modes. If some of these lower frequency modes are strongly coupled to the modes that give rise to the weak, yet detectable, absorbance in the FTIR spectra at ~2110 cm^{-1} (Figure 6.2a), an off-diagonal peak appears. Consistent with this notion, other strongly hydrogen-bonded aggregates have been reported[35,158,159,188] to exhibit such strong coupling.

Since this scenario results in off-diagonal contributions to the spectra only after vibrational relaxation, one may expect a delayed appearance of the transient signal below the diagonal. Despite our pulse duration being ~150 fs and the contribution of different 'artifacts'[44] at such early delay times, the delay traces in Figure 6.5a may indeed indicate that the signal below the diagonal appears delayed relative to the signal on the diagonal. The observed 60 fs delay is in fact similar to the vibrational relaxation time of the on-diagonal peak (see discussion below). As such, also the temporal evolution of the signals supports the scenario described above: After vibrational relaxation with a ~100 fs time scale, a manifold of lower frequency vibrational states is transiently populated, which modulate the spectral signatures of both, the initially excited modes underlying the peak at 2040 cm^{-1} and the modes giving rise to the absorbance at ~2100 cm^{-1} (Figure 6.2). It is important to note, that for the present samples, where molecular aggregates between the base and acid molecule(s) are separated from each other by solvent molecules, the

vibrational energy is initially (within ~100 fs) distributed over lower energy modes of molecules in spatial proximity. Conversely, relaxation and dissipation of the energy to low-frequency modes of more distant molecules typically occur on much longer timescales.[45,189,190] As such, the delayed, though very fast appearance of the bleaching signal at ω_{Probe} ~2110 cm^{-1} suggests that after excitation of the vibrations at 2040 cm^{-1} the transiently populated lower frequency modes are localized within the same molecular aggregate.

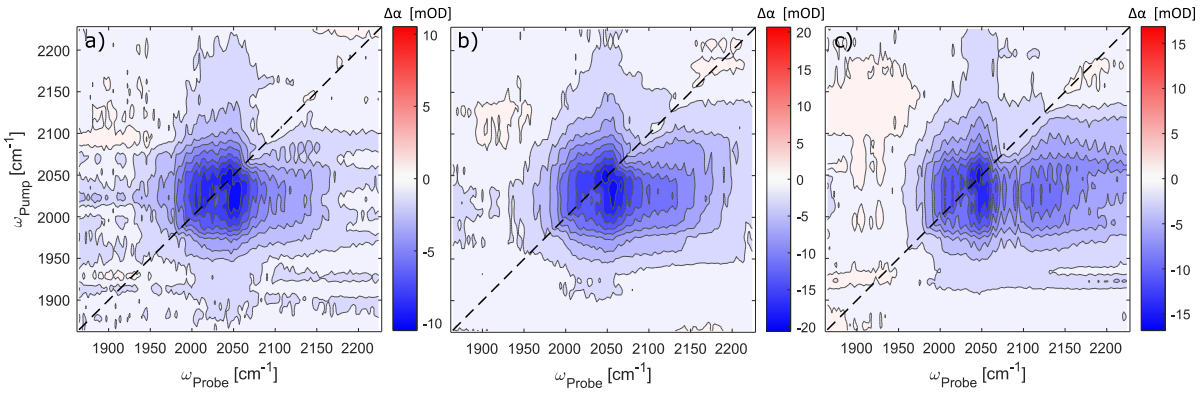

Figure 6.4: 2D-IR spectra at t = 50 fs for solutions of 0.5 mol L^{-1} DPP and a) 0.75 mol L^{-1}, b) 0.5 mol L^{-1}, and c) 0.25 mol L^{-1} Qu in DCM. All spectra show a bleach at 2040 cm^{-1}, which is related to ionic hydrogen bonds. With increasing DPP concentration an off-diagonal peak at 2040 cm^{-1}/2110 cm^{-1}appears.

An observation that provides further insight into the origins of the transient bleach below the diagonal is its dependence on the molar composition. As can be already seen from the 2D-IR spectra in Figure 6.4, the negative signal at (2110 cm^{-1}/2040 cm^{-1}) is weak for an excess of base (Figure 6.4a), while for an excess of acid the bleaching signal below the diagonal is more pronounced (Figure 6.4c). To quantify the contribution of this off-diagonal peak to the 2D-IR spectra, we determine the volume integrals of both signals at (2110 cm^{-1}/2040 cm^{-1}) and (2040 cm^{-1}/2040 cm^{-1}). The ratios of the integrated intensities (over ω_{Pump} = 1980-2083 cm^{-1} and ω_{Probe} = 1980-2083 cm^{-1} or 2083-2230 cm^{-1}) in Figure 6.5b show a marked correlation with the concentration of base, indicating that the spectral signature below the diagonal correlates with the excess of acid. We note that for an excess of acid also DPP homodimers are present (Figure 6.2a), yet for excitation centred at 2040 cm^{-1} for solutions of only DPP, we find no detectable signals (see Figure 6.11). This renders the signal below the diagonal in Figure 6.4 to be due to acid homodimers unlikely. Conversely, the trend (Figure 6.5b) is in line with the formation of the previously reported trimers and/or multimers.[74] In these multimers, the P-O$^-$···H-O-P hydrogen bonds are also spatially close to O$^-$···H-N$^+$ hydrogen bonds (see also Figure 6.1) and our *ab initio* calculations indicate that also their transition frequencies are rather similar (Figure 6.3a and Figure 6.3c). Hence, the appearance of the signal at (2110 cm^{-1}/2040 cm^{-1}) can be explained by excitation and relaxation of the O$^-$···H-N$^+$ hydrogen bond at 2040 cm^{-1} after which the dissipated excess energy gives rise to a transient modulation of the P-O$^-$···H-O-P hydrogen bonds (and the O$^-$···H-N$^+$ hydrogen bonds) within multimers.

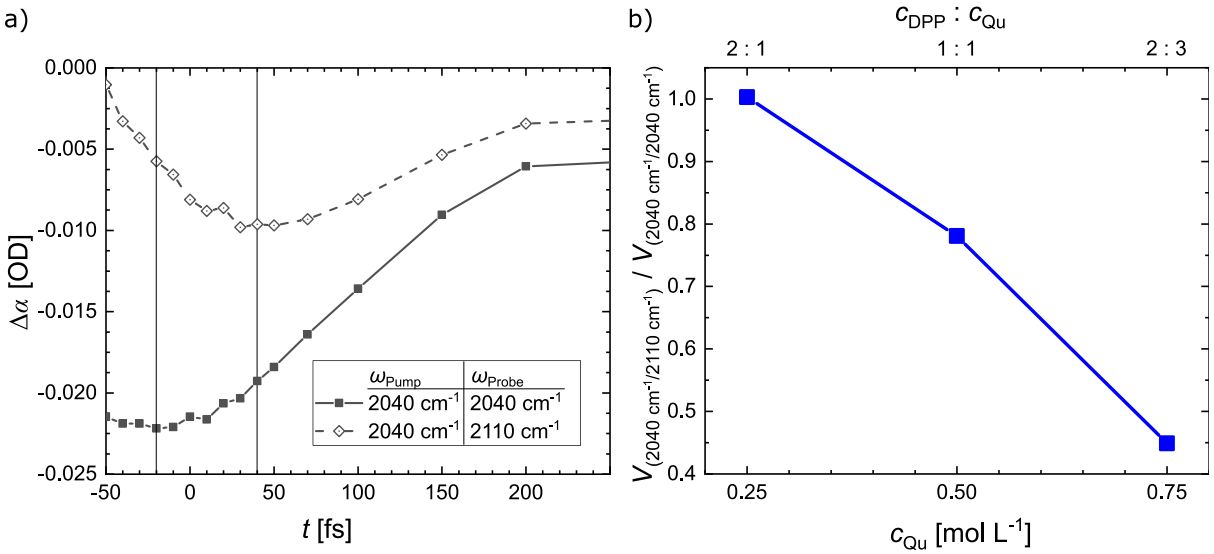

Figure 6.5: a) Time traces of selected 2D-IR peaks (2040 cm^{-1}/2040 cm^{-1}) and (2040 cm^{-1}/2110 cm^{-1}) for the equimolar mixture of DPP and Qu in DCM. A ~60 fs delayed appearance of the maximum bleach for the (2040 cm^{-1}/2110 cm^{-1}) trace, relative to the (2040 cm^{-1}/2040 cm^{-1}) trace can be observed. The two vertical solid black lines mark maximum bleach of both signals. b) Ratio of the volume integrals of the off-diagonal peak to the on-diagonal peak vs concentration of Qu at $t = 50$ fs. The integrals were taken at pump frequencies from 1980 to 2083 cm^{-1} and probe frequencies 1980-2083 cm^{-1} or 2083-2230 cm^{-1}. It shows the increase of the peak integral at (2040 cm^{-1}/2110 cm^{-1}) with increasing DPP to Qu ratio.

To further support the notion that fast vibrational relaxation leads to an off-diagonal peak due to the P-O⁻···H-O-P group in trimers, we investigate the vibrational dynamics of Qu-DPP mixtures in more detail. Since the 2D-IR spectra exhibit very little dependence on the pump frequency, we explore the vibrational dynamics based on broadband IR pump-probe experiments at 1880-2135 cm^{-1} (for experiments centred at ~2500 cm^{-1} see Figure 6.12 & Figure 6.13). In an IR pump-probe experiment the transient signals are recorded as a function of delay time; in contrast to a 2D-IR experiment, the sample's response is integrated over all pump frequencies. The thus obtained transient spectra at early delay times (Figure 6.6a) resemble the spectral signatures (dominant bleach at 2040 cm^{-1} and a shoulder above ~2100 cm^{-1}) as seen in the 2D-IR experiments. Similar to the 2D-IR experiments, also in the pump-probe experiments the bleaching signal above 2100 cm^{-1} reaches its maximum somewhat delayed (Figure 6.6a). Yet, to avoid contributions from optical artefacts, we omit data at $t < 0.1$ ps for the analysis below.

As can be seen from the delay traces in Figure 6.6b and Figure 6.14 the transient signals rapidly decay with increasing delay time. This rapid decay indicates that the population of the excited state relaxes fast to lower frequency modes. At $t > 5$ ps the signals plateau and the remaining, weak modulation arises from a heated ground state for which the spectral modulation results from a slight local rise in temperature. To quantitatively extract the vibrational relaxation dynamics, we fit a kinetic relaxation model to the transient signals (Figure 6.6d):[191] In this model, infrared excitation populates a vibrationally excited state, **1***. Upon relaxation with a relaxation time τ_A an intermediate state, **0'**, is transiently populated, which further

relaxes with a relaxation time τ_B to a heated ground state, **0''**. We note that in this model, the states **0'** and **0''** subsume the manifold of states over which the vibrational energy is distributed. For instance, the thermal states **0''** contains all states that are populated upon increase of the temperature after reaching a local thermal equilibrium. We assume the same population dynamics at all probe frequencies, with different transient spectra for the three-states (i.e. different spectral contributions of the three states, see Figure 6.15). Similar to previous reports on the vibrational dynamics of 7-azaindole-acetic acid dimers[159] and acetic acid homodimers,[47] this three state model can describe the experimental data with the least number of adjustable parameters: As can be seen from the solid lines in Figure 6.6a-b, the model excellently describes the experimental data for the DPP-Qu mixtures studied here over the entire delay time range at all probe frequencies, while a two-state model cannot fully capture the dynamics at $0.1 \leq t/\text{ps} < 5$ (see red dashed line in Figure 6.6b). From this model we find the initial relaxation time τ_A to be very fast, ~100 fs, and independent of the concentration of the base (Figure 6.6c). The short relaxation time is again indicative of strong (anharmonic) coupling to lower-frequency modes, which also provides efficient transfer paths for the excess vibrational energy.[47,159]

From the kinetic model, we find that τ_B – the relaxation from the intermediate state **0'** – depends on the molar ratio of acid and base (Figure 6.6c). We find faster relaxation from the intermediate state for high concentrations of Qu ($\tau_B \approx 0.8$ ps at c_{Qu}=0.75 mol L^{-1}), while the relaxation is slower for an excess of the acid ($\tau_B \approx 1.1$ ps at c_{Qu}=0.25 mol L^{-1}). This variation of the relaxation rate again suggests that the formation of multimers critically affects vibrational couplings and thus energy relaxation pathways. Together, these results together with our findings from 2D-IR experiments are consistent with fast relaxation and strong coupling within the dimer/multimer structures.

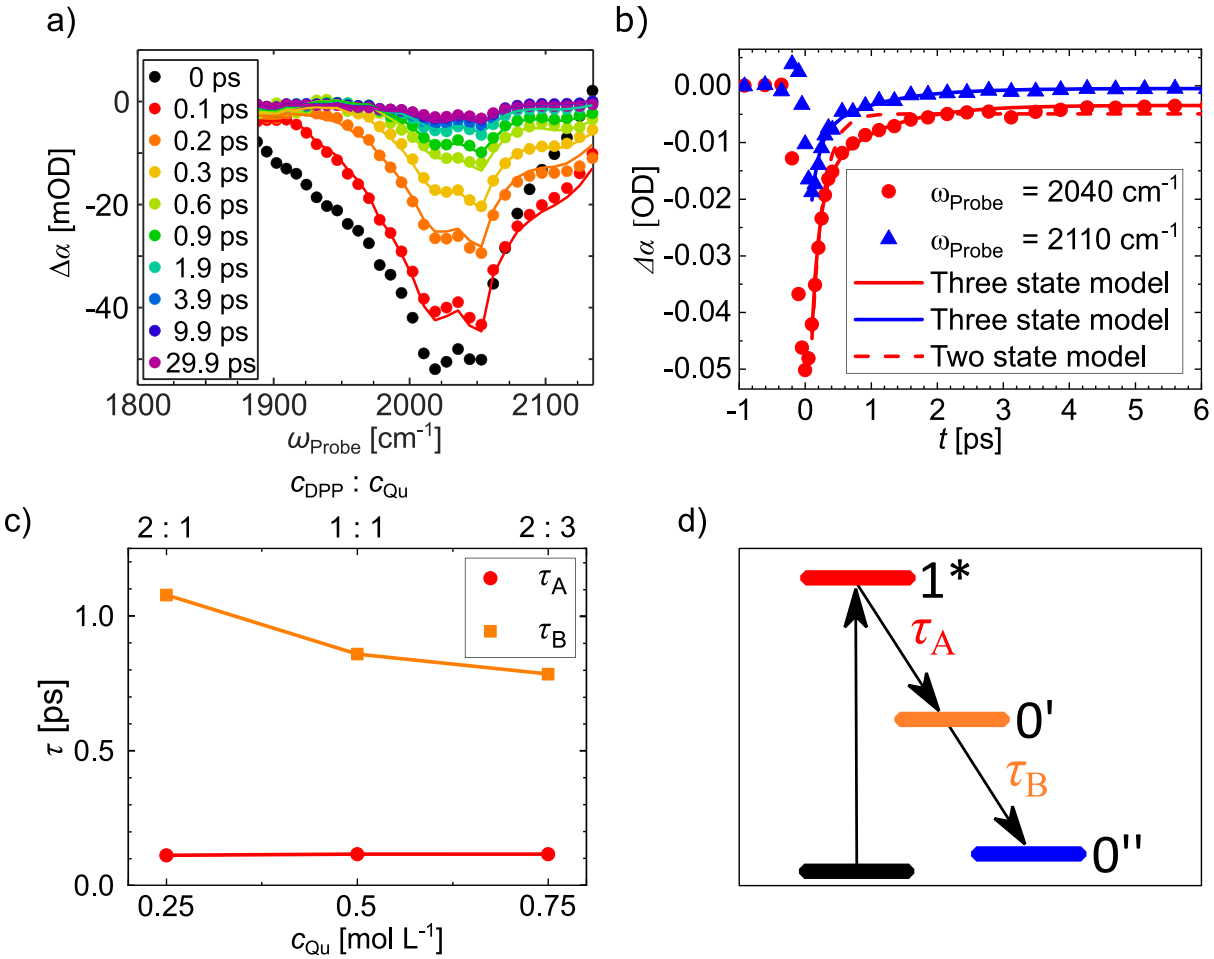

Figure 6.6 a) Transient infrared spectra of an equimolar mixture of Qu and DPP showing a structured peak at 2040 cm^{-1} and a shoulder at 2110 cm^{-1}, which appears ~100 fs delayed. b) Delay traces at selected probing frequencies for an equimolar mixture of DPP and Qu in DCM. Symbols show experimental data and solid lines show the fits with the three-state kinetic model. The dashed red line shows the fit with a two-state model at ω_{Probe} = 2040 cm^{-1}. c) Relaxation times as a function of concentration of Qu, as extracted from fitting the kinetic model (panel d) to the transient data.

6.3.4 Concluding remarks

We report on the vibrational structure and dynamics of hydrogen-bonded complexes consisting of the base quinaldine and diphenyl phosphoric acid. At all compositions, we find broad absorption features in the infrared absorption spectra spanning more than 1000 cm^{-1}. Upon addition of quinaldine to a solution of diphenyl phosphoric acid, the infrared absorption gradually red-shifts to lower frequencies and for an excess of base the observed absorbance peaks at ~2040 cm^{-1}. *Ab initio* calculations of the potential energy for translating a proton within a doubly ionic hydrogen bonds between DPP and Qu, within a singly ionic hydrogen bond between a DPP acid and a DPP^- anion, and a neutral hydrogen bond within an DPP homodimer, suggest that all these hydrogen-bonding motifs contribute to the observed infrared absorption at 1800 cm^{-1} – 2800 cm^{-1}. The associated proton potentials of these bonds are very anharmonic: within the doubly ionic hydrogen bonds the proton is localized near the base in its vibrational ground state, but becomes more delocalized in the first excited state. Thus, anharmonic coupling of the proton vibrations to other modes, together thermally induced fluctuations, are the likely

cause for to the width of the absorptions in the IR spectra. Yet, our calculations indicate that at ~2040 cm^{-1} contributions from doubly ionic hydrogen bonds and singly ionic hydrogen bonds within ion-pairs and/or multimers dominate.

Ultrafast infrared experiments reveal very fast vibrational relaxation on a ~100 fs timescale after excitation at ~2040 cm^{-1}. This fast vibrational relaxation goes along with (transient) population of lower-frequency vibrational modes, which give rise to somewhat longer lived (0.8-1.1ps) spectral modulations. A somewhat delayed off-diagonal peak in the 2D-IR spectra, which is most pronounced for an excess of acid, suggests that some of these lower-frequency vibrational modes are strongly coupled to both the $^{+}$N-H···$^{-}$O-P hydrogen bond and the P-O^{-}···H-O-P hydrogen bond in multimers. Given the strong coupling of the lower-frequency modes to both hydrogen bonds within such multimeric structures, our results suggest that the relevant lower frequency modes are presumably located at the phosphate group of the DPP anion.

Our results indicate that the molar ratio of acid to base critically affects vibrational structure and dynamics. Even for equimolar mixtures, formation of trimers and/or larger multimers results in additional vibrational coupling and dynamics that differ from those of isolated acid-base dimers. Thus, equimolar mixtures can be sometimes misleading when one aims at isolating the strong hydrogen bonds between acids and bases. More generally, our results indicate very fast proton dynamics in strong, doubly ionic hydrogen-bonded aggregates of DPP and quinaldine, which are relevant to Brønsted acid organocatalysis. Fast vibrational relaxation and strong coupling of the studied vibrational modes show that the doubly ionic hydrogen bond can efficiently dissipate excess energy from Qu into lower-frequency modes. Coordination of an additional DPP molecule to form a trimer alters energy transfer paths and rates. As the strong anharmonicity of the vibrational modes enables this energy transfer, it may be also relevant to the transport of energy upon chemical conversion.

6.4 Supporting information

6.4.1 Fourier transform infrared spectra

Figure 6.7 shows linear infrared (IR) spectra of quinaldine (Qu) and diphenyl phosphoric acid (diphenyl phosphate, DPP) dissolved in dichloromethane (DCM). Two unique bands at 2040 cm^{-1} and 2500 cm^{-1} and a minor band at about 3400 cm^{-1} appear in solutions containing Qu and DPP, i.e. the A,B,C-type pattern.[154,166] Further, with increasing c_{Qu} the intensity of the DPP-DPP homodimer OH mode at ~2800 cm^{-1} decreases as aggregates between Qu and DPP are formed.

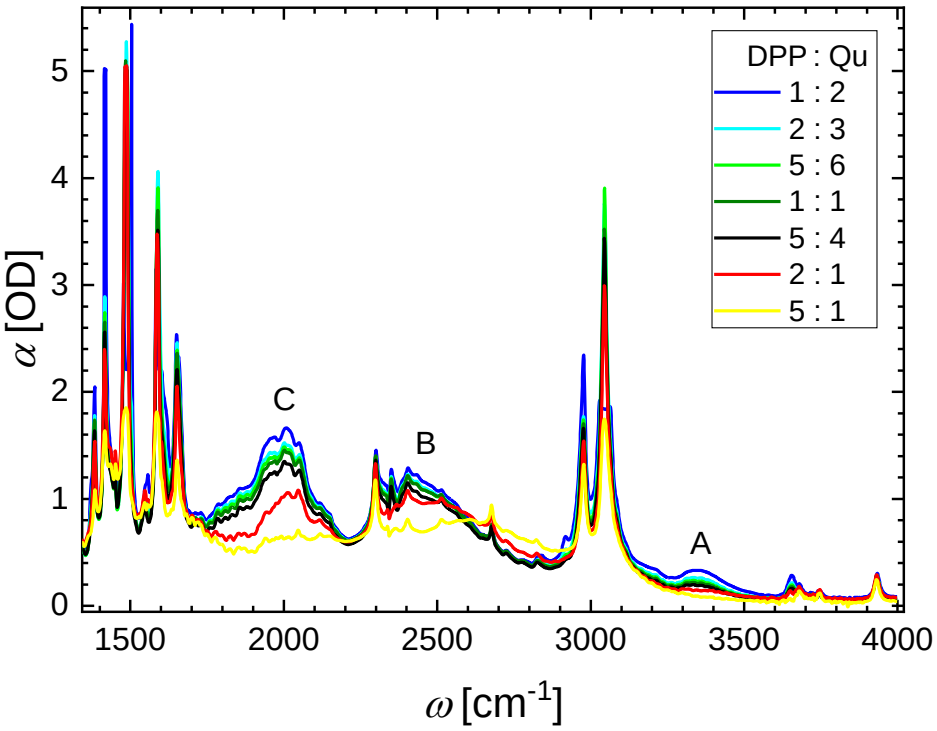

Figure 6.7 FTIR spectra of Qu and DPP mixtures in DCM, with the A,B,C-type pattern at 3400 cm^{-1}, 2500 cm^{-1}, and 2040 cm^{-1}. All solutions contain 0.5 mol L^{-1} Qu with varying DPP concentration (1, 0.75, 0.6, 0.5, 0.4, 0.25, and 0.1 mol L^{-1}).

6.4.2 Ab initio calculations

All calculations were performed using Gaussian 16[185] *(*B3LYP-D3(BJ)/6-31G(d) level of theory[145–147]) applying a polarizable continuum model[184] (dichloromethane) and Grimme's D3 dispersion with Becke-Johnson damping[183]. Figure 6.8 shows the optimized geometries of the ion-pair a), the DPP···DPP homodimer b) and c) the negatively charged DPP···DPP homodimer with Lithium as counterion.

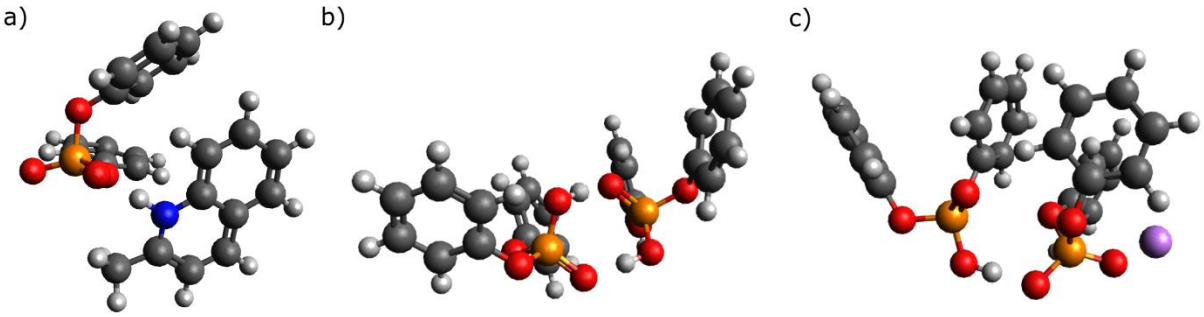

Figure 6.8 Optimized geometry for a) doubly ionic hydrogen-bonded DPP-Qu ion-pairs, b) the DPP homodimer and c) the negatively charged DPP···DPP homodimer with Lithium as counterion. All structures were calculated with DCM as solvent.

The potential shown in Figure 6.3 were obtained from a non-relaxed potential energy surface scan, starting from the optimized geometry and varying the N-H distance along the N-O axis of the doubly ionic hydrogen bond. Note that in the optimized geometry the hydrogen bonds are not perfectly linear, instead the IP has an HNO angle of 3.6°, the DPP homodimer has an HOO angle of 6.0° and the negatively charged DPP···DPPP homodimer with Lithium as counterion has an HOO angle of 0.6°.

In order to estimate vibrational transition frequencies of the N^+-H···O^- and O-H···O stretching mode we calculated the energies of the three lowest-lying eigenstates taking the potential energy as a function of the proton displacement along N-O/O-O bond vector. To this end, we have approximated the potential energy obtained on a scarce 0.05 Å grid from a non-relaxed energy scan (see above) with a quartic function describing an asymmetric double-well potential (similar to the function employed by Tokmakoff et al.[179]):

$$U(x) = \mu * (x - x_0)^4 - \kappa * (x - x_0)^2 + \beta * (x - x_0) + y_0 \qquad (6.1)$$

The values of the fitted parameters and their explanation are given in Table 6.1.

Table 6.1 Parameters obtained from fitting eq. (6.1) to the potential shown in Figure 6.3.

Parameter	Fit result			Description
	QuH^+···DPP^-	DPP···DPP	Li^+···DPP^-···DPP	
μ, $cm^{-1}/Å^4$	286000 ± 4000	323000 ± 5000	338000 ± 4000	quartic parameter that controls the potential steepness at the edges
κ, $cm^{-1}/Å^2$	35000 ± 800	30500 ± 1000	27700 ± 800	quadratic parameter that controls the barrier height and steepness
β, $cm^{-1}/Å$	7300 ± 100	11200 ± 100	7800 ± 100	linear parameter that controls the asymmetry of the potential (inequivalence of the two wells)
x_0, Å	1.355 ± 0.001	1.301 ± 0.001	1.286 ± 0.001	centre of the potential
y_0, cm^{-1}	2990 ± 30	3440 ± 40	2280 ± 20	offset

The obtained potential function was used to construct the Hamiltonian matrix within discrete variable representation (DVR) using the 'particle in a box' eigenfunctions as basis.[186] The reduced mass was assumed to be the proton mass. The eigenvalues of the Hamiltonian matrix were used to calculate the transition frequencies between the corresponding eigenstates shown in Figure 6.3 in the main text.

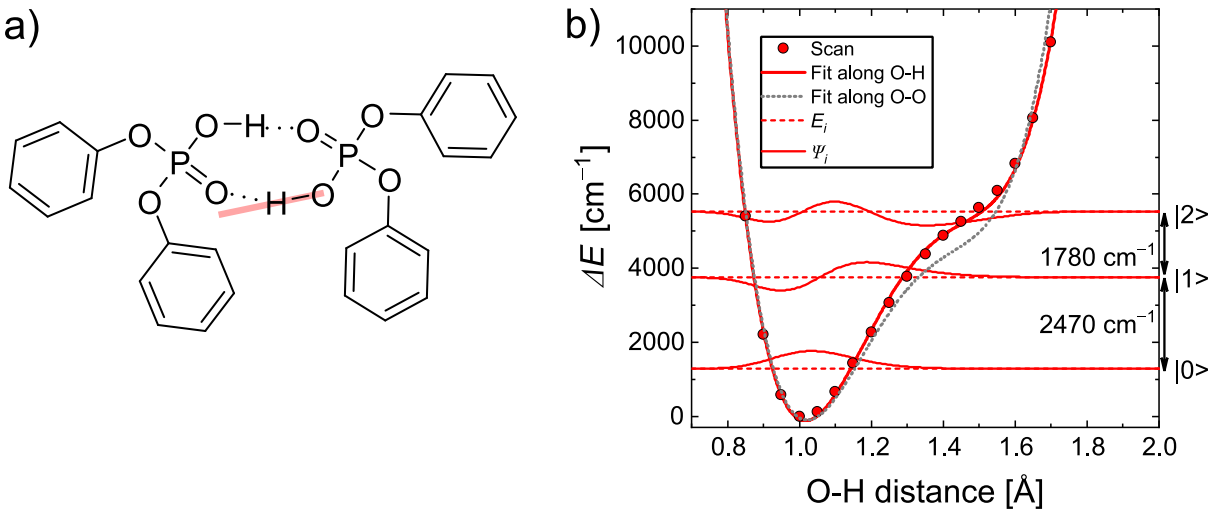

Figure 6.9 a) shows a schematic of the optimized geometry, where the O···HO hydrogen bond is not straight, but has a OOH angle of 6°. In b) the potential corresponding to the proton displacement along the original OH axis of the optimized geometry is shown, which results in a |0> to |1> transition energy of 2470 cm^{-1}. The potential of a proton movement along the O-O axis is shown as grey dots for comparison.

In order to quantify the accuracy of the derived transition frequencies, we compare the transition frequency difference of a scan along the O-H axis of the optimized geometry with the one along the O-O axis for a DPP homodimer. The difference is 160 cm^{-1}, which shows that only the general frequency trends received by the calculations can be trusted.

6.4.3 Diagonal cut of the 2D-IR spectrum

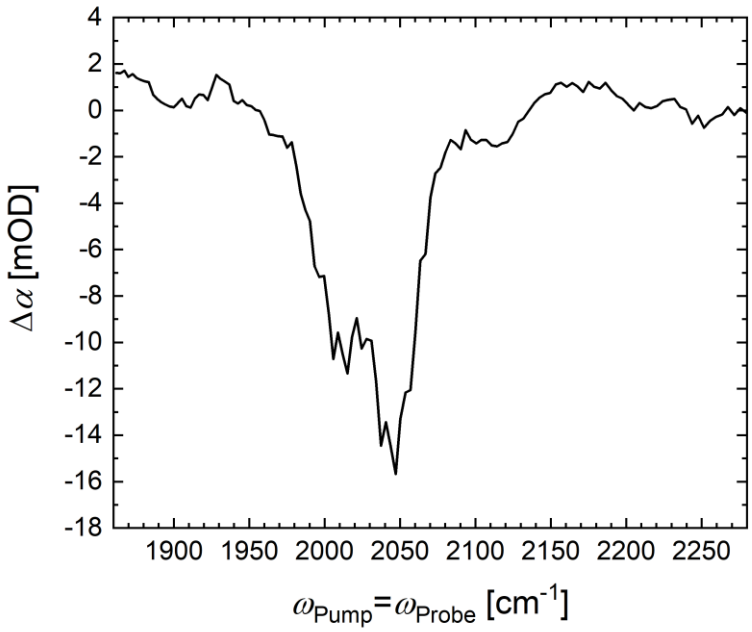

Figure 6.10 Cut along the diagonal for the 2D-IR spectrum of a 1:1 mixture of DPP and Qu at t = 50 fs, (Figure 6.4b), which exhibits two main maxima at ~2010 cm^{-1} and ~2040 cm^{-1}.

6.4.4 Transient IR experiments on DPP in DCM

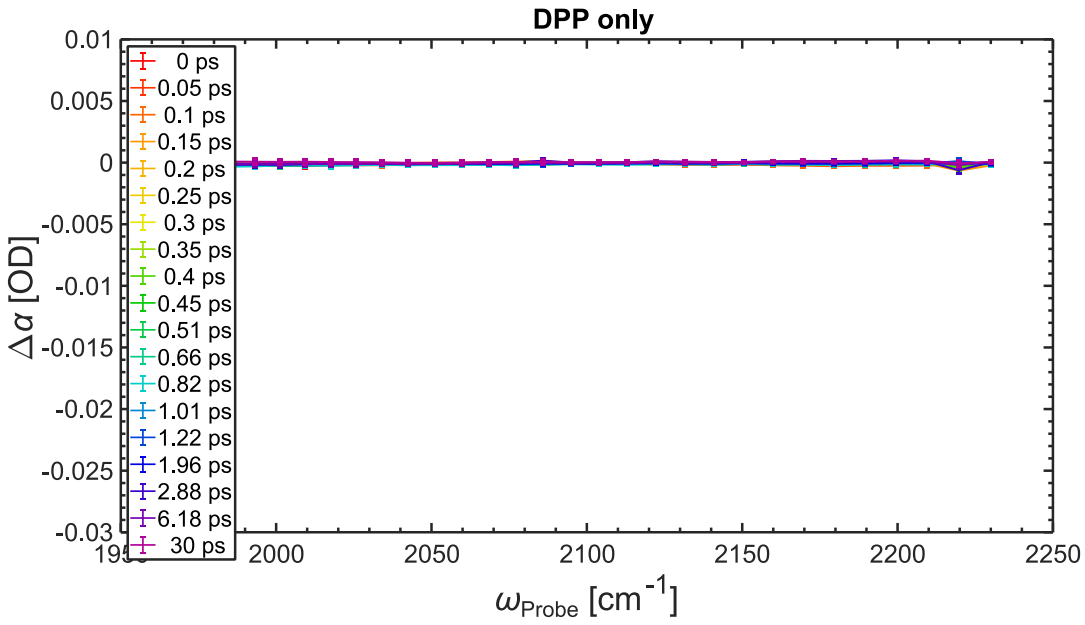

Figure 6.11 Transient IR spectra of 0.5 mol L^{-1} DPP in DCM exhibit no detectable signals. All other experimental parameters are the same as for the experiments shown in Figure 6.6a of the main manuscript.

6.4.5 Transient IR experiments on Qu and DPP at 2500 cm^{-1}

Figure 6.12 shows the transient IR spectra of different DPP-Qu mixtures in DCM with the pump and probe pulses centred at ~2500 cm^{-1}. With increasing Qu concentration, the maximum bleach shifts to lower frequencies, similar to the IR absorption peak (Figure 6.7). The transient absorption spectra are fitted with the same three state relaxation model as the transient absorption data measured at 2040 cm^{-1} (Figure 6.6). The thus obtained relaxation times (Figure 6.13) exhibit the same variation with Qu concentration as the data shown in Figure 6.6c. The fast component (~100 fs) agrees well with the results shown Figure 6.6. The slower relaxation time is slower for experiments at ~2500 cm^{-1}, as compared to the experiments at 2040 cm^{-1}, which may indicate different relaxation pathways. The similarity of the relaxation at 2500 cm^{-1} and at 2040 cm^{-1} supports the notion that both frequency ranges have a common molecular origin (separated by the Evans hole[27,166,168]).

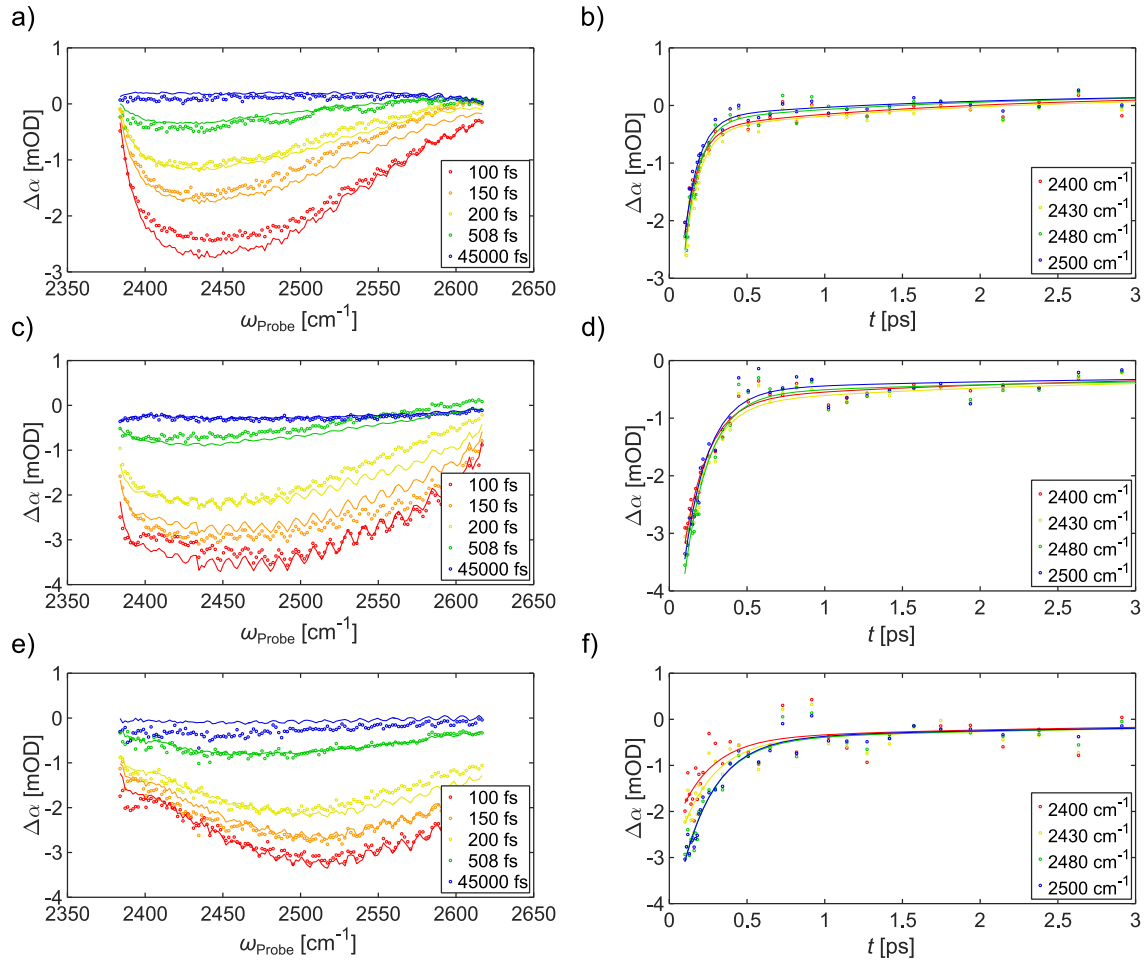

Figure 6.12 Transient IR experiments on mixtures of Qu and DPP in DCM at 2500 cm^{-1}. The DPP concentration is kept constant at 0.5 mol L^{-1}, while c_{Qu} decreases from top to bottom: a) & b) is 0.75 mol L^{-1}. c) & d) 0.5 mol L^{-1}, and e) & f) 0.25 mol L^{-1}. The transient spectra are shown on the left, while the time traces are shown on the right. Symbols represent experimental data and lines show fits with the three-state kinetic model.

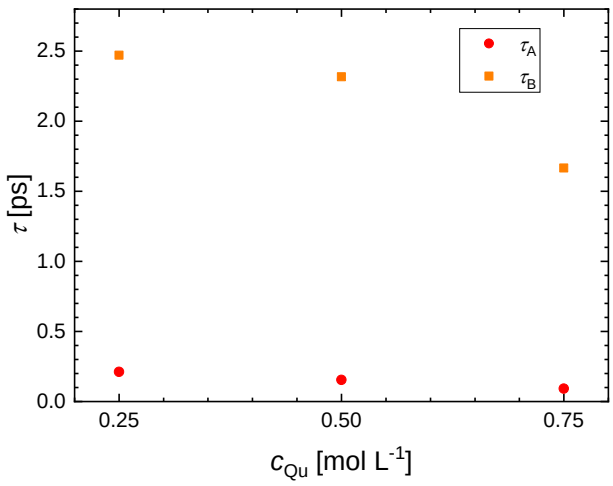

Figure 6.13 Relaxation times obtained from fitting the three-state kinetic model to the data in Figure 6.12.

6.4.6 Transient IR experiments on Qu and DPP in DCM at 2000 cm^{-1}

Figure 6.14 shows the transient IR data of Qu and DPP mixtures in DCM at 2000 cm^{-1} together with the fits using the kinetic model to obtain the relaxation times shown in Figure 6.6c. The spectra associated with the excited state **1***, the intermediate state **0'**, and the heated ground state **0''** as obtained from fitting the kinetic model to the experimental spectra are shown in Figure 6.15.

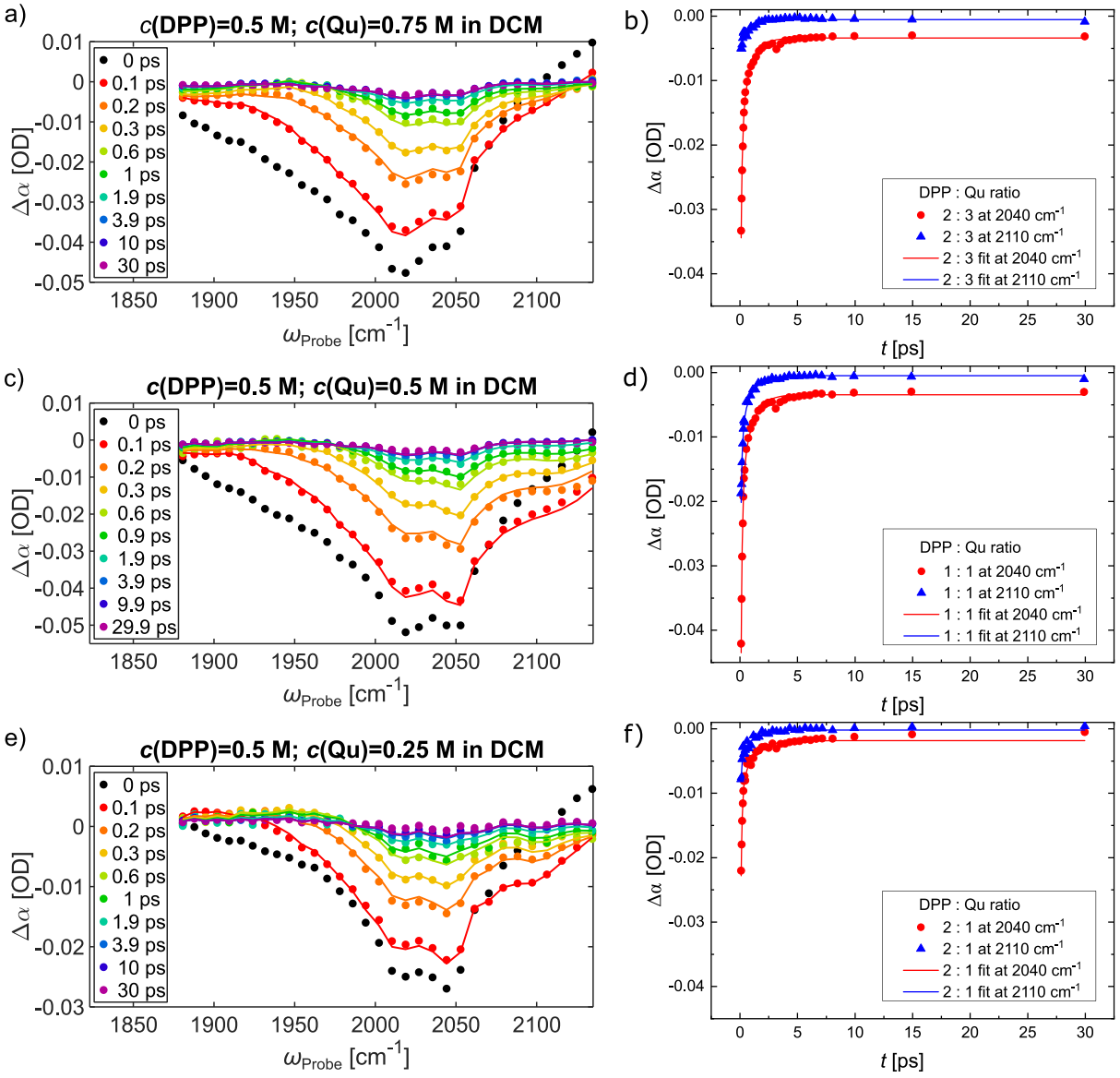

Figure 6.14 Transient infrared spectra and delay traces at selected probing frequencies for DPP:Qu mixtures at molar ratios 2:3 (a-b), at 1:1 (c-d), and 2:1 (e-f). Symbols show experimental data and lines show the fits with the kinetic model.

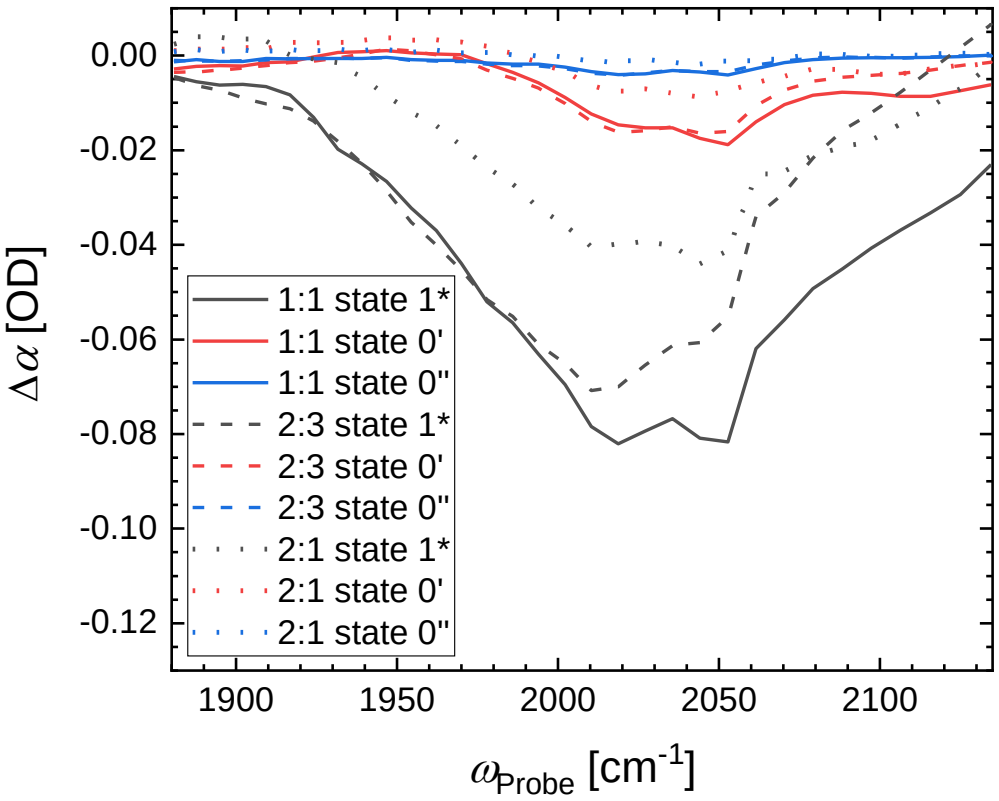

Figure 6.15 Spectra of the excited state, the intermediate state, and the heated ground state obtained by fitting the kinetic model to the experimental spectra for solutions at different DPP:Qu ratios (1:1, 2:3, and 2:1).

7 Conclusion and outlook

In this thesis I have studied the interaction of Brønsted acid organocatalysts with substrates, using equimolar mixtures of an organocatalyst (diphenyl phosphate (DPP)) and two imines (quinaldine (Qu) and 2-phenylquinoline (PhQu)) as model systems. I have shown that these model systems for acid base interactions do not only form the expected one-to-one aggregates, but also multimers consisting of one imine and more than one DPP molecule. With the help of both, DRS and NMR spectroscopy, I have shown that ion-pairs are the dominating species, however, already at low DPP concentrations a significant amount of multimers is formed. Both types of aggregates, ion-pairs and multimers, have relatively similar dipole moments and the lifetime of their intermolecular bonds are in the range of hundreds of picoseconds up to milliseconds. Furthermore, I have proposed a plausible structure for the trimers based on the NMR data. In general, my results show that the multimer formation in equimolar mixtures can explain the previously reported splitting of the acidic proton peak in low-temperature NMR and show that multimer formation needs to be considered in model systems for catalyst development.

One major goal for catalyst development is the implementation of rational design, replacing the current approach which is mainly based on trial and error. To the development of a rational organocatalysis design, I have contributed a study on the ion-pair and multimer formation in three different solvents, which are relevant for organocatalysis. A quantification of the ion-pair formation for different imine and solvent combinations is important, as ion-pairs are considered to constitute the reactive intermediate in a catalytic reaction. Furthermore, the study is expanded, including a second imine (PhQu), as a first step in order to generalize the findings for imines. Here, I have shown that, for a given solvent, there is a correlation between the association constant governing the ion-pair formation and the yield, which is valid for both investigated imines. The association constant is smaller for solvents with a higher hydrogen bonding affinity. In this study, the lowest ion-pair formation is found in solutions in THF for both imines. However, not only the solvent, but also the imine affects the ion-pair formation, as a clear difference in the tendency to form ion-pairs is found between the two imines. More ion-pairs are formed when Qu is added to DPP solved in DCM as compared to PhQu. The same trend is observed in chloroform. Even though organocatalysis requires relatively high catalyst loadings, which suggests that multimers could play a role, I have found no correlation between the solvent dependent multimer formation and the yields reported in literature. In general, the combined approach based on NMR and DRS shows that the multimer formation is not a unique property of Qu and DPP mixtures in DCM but seems to be a more common phenomenon in nonpolar solvents, which I have quantified.

To understand Brønsted acid organocatalysis on a fundamental level, not only knowledge of the species formed in solution is needed, but also on how they interact. Therefore, I studied the hydrogen bond motif in mixtures of Qu and DPP by means of infrared spectroscopy. The resulting linear IR spectra of the mixtures show very broad and intense peaks, which are not present in the IR spectra of solutions of only Qu or DPP. The broad

peaks around 2000 cm^{-1} are the spectral feature of strongly hydrogen-bonded systems such as the doubly ionic hydrogen bonds ($^{+}$N-H···O^{-}) present in ion-pairs and multimers formed by Qu and DPP. I have found very fast vibrational relaxation, which changes with concentration. This suggests an influence of the formed aggregates in solution on the relaxation pathways. Further, I observed the appearance of an off-diagonal peak in the 2D-IR data. The observed off-diagonal peak can be explained by strong anharmonic coupling involving a lower-frequency mode. Another unusual feature of the non-linear IR spectra is the absence of an excited state absorption around 2000 cm^{-1}. This observation can be explained by a shift of the excited state absorption to much lower frequencies due to the very strong anharmonicity of the ($^{+}$N-H···O^{-}) proton potential. This is supported by non-relaxed potential energy scans for the proton potential based on *ab initio* calculations. These findings are relevant to Brønsted acid catalysis, as the very strong coupling of the H-bond allows efficient dissipation of excess energy, which could be important during the catalytic reaction as a potential pathway of energy transport.

Following up on the findings presented in this thesis, it would be interesting to identify the involved low-frequency vibrations. For that purpose, two-dimensional terahertz-infrared-visible spectroscopy can be applied. It allows investigating the coupling between the modes in the IR and the THz / far-IR frequency range. The THz / far-IR range is of special interest, as it is the frequency range of collective molecular motions and librations, such as hydrogen bonds. Further, two-colour 2D-IR spectroscopy can be applied to study the dynamics of the peaks at 2000 cm^{-1} and 2500 cm^{-1} and the origin of the transmission window (Evans hole) between these peaks. In this way the current knowledge on doubly ionic hydrogen bonds can be expanded.

Another important question is how the stereo information of the catalyst is transferred onto the substrate. Here, solutions of BINOL-phosphate-based chiral Brønsted acid catalysts (e.g. trisisopropenylphenyl BINOL phosphate, phenanthrenyl BINOL phosphate) are a good catalytic system to study, as these catalysts provide very good stereoselectivities, however, the origin of their stereoselectivity is unclear. Until today no one has yet been able to unambiguously predict stereoselectivity for new catalyst substrate combinations. To answer this question, a set of experiment on chiral Brønsted acid organocatalysts and substrates could be used to study the transfer of chirality on the previously non-chiral substrate. This can be observed using vibrational circular dichroism (VCD) on catalyst-substrate aggregates. In both suggested experiments, the use of isotope labels may be very beneficial, as it allows to select or identify individual vibrations.

8 Bibliography

1. Atkins, P. & de Paula, J. *Physical Chemistry*. (Oxford University Press, 2006).
2. Vogel, P., Lam, Y., Simon, A. & Houk, K. Organocatalysis: Fundamentals and Comparisons to Metal and Enzyme Catalysis. *Catalysts* **6**, 128 (2016).
3. Morbidelli, M., Gavriilidis, A. & Varma, A. *Catalyst Design*. (Cambridge University Press, 2001).
4. Hopmann, K. H. Quantum chemical studies of asymmetric reactions: Historical aspects and recent examples. *Int. J. Quantum Chem.* **115**, 1232–1249 (2015).
5. MacMillan, D. W. C. The advent and development of organocatalysis. *Nature* **455**, 304–308 (2008).
6. Rueping, M., Antonchick, A. P. & Theissmann, T. A Highly Enantioselective Brønsted Acid Catalyzed Cascade Reaction: Organocatalytic Transfer Hydrogenation of Quinolines and their Application in the Synthesis of Alkaloids. *Angew. Chemie Int. Ed.* **45**, 3683–3686 (2006).
7. Mahlau, M. & List, B. Asymmetric Counteranion-Directed Catalysis (ACDC): A Remarkably General Approach to Enantioselective Synthesis. *Isr. J. Chem.* **52**, 630–638 (2012).
8. List, B. Introduction: Organocatalysis. *Chem. Rev.* **107**, 5413–5415 (2007).
9. Parmar, D., Sugiono, E., Raja, S. & Rueping, M. Complete Field Guide to Asymmetric BINOL-Phosphate Derived Brønsted Acid and Metal Catalysis: History and Classification by Mode of Activation; Brønsted Acidity, Hydrogen Bonding, Ion Pairing, and Metal Phosphates. *Chem. Rev.* **114**, 9047–9153 (2014).
10. Akiyama, T., Itoh, J., Yokota, K. & Fuchibe, K. Enantioselective Mannich-Type Reaction Catalyzed by a Chiral Brønsted Acid. *Angew. Chemie Int. Ed.* **43**, 1566–1568 (2004).
11. Akiyama, T. Stronger Brønsted Acids. *Chem. Rev.* **107**, 5744–5758 (2007).
12. Mahlau, M. & List, B. Asymmetric Counteranion-Directed Catalysis: Concept, Definition, and Applications. *Angew. Chemie Int. Ed.* **52**, 518–533 (2013).
13. Rueping, M., Sugiono, E. & Azap, C. A Highly Enantioselective Brønsted Acid Catalyst for the Strecker Reaction. *Angew. Chemie Int. Ed.* **45**, 2617–2619 (2006).
14. Brak, K. & Jacobsen, E. N. Asymmetric Ion-Pairing Catalysis. *Angew. Chemie Int. Ed.* **52**, 534–561 (2013).
15. Yang, X. & Toste, F. D. Direct asymmetric amination of α-branched cyclic ketones catalyzed by a chiral phosphoric acid. *J. Am. Chem. Soc.* **137**, 3205–3208 (2015).
16. Rueping, M., Azap, C., Sugiono, E. & Theissmann, T. Brønsted Acid Catalysis: Organocatalytic Hydrogenation of Imines. *Synlett* 2367–2369 (2005).
17. Hunt, P. A., Ashworth, C. R. & Matthews, R. P. Hydrogen bonding in ionic liquids. *Chem. Soc. Rev.* **44**, 1257–1288 (2015).

18. Kim, H. *et al.* Role of Ion-Pairs in Brønsted Acid Catalysis. *ACS Catal.* **5**, 6630–6633 (2015).

19. Staib, A., Borgis, D. & Hynes, J. T. Proton transfer in hydrogen-bonded acid–base complexes in polar solvents. *J. Chem. Phys.* **102**, 2487–2505 (1995).

20. Rueping, M., Antonchick, A. P. & Theissmann, T. Remarkably Low Catalyst Loading in Brønsted Acid Catalyzed Transfer Hydrogenations: Enantioselective Reduction of Benzoxazines, Benzothiazines, and Benzoxazinones. *Angew. Chemie Int. Ed.* **45**, 6751–6755 (2006).

21. Overvoorde, L. M., Grayson, M. N., Luo, Y. & Goodman, J. M. Mechanistic Insights into a BINOL-Derived Phosphoric Acid-Catalyzed Asymmetric Pictet–Spengler Reaction. *J. Org. Chem.* **80**, 2634–2640 (2015).

22. Milo, A., Bess, E. N. & Sigman, M. S. Interrogating selectivity in catalysis using molecular vibrations. *Nature* **507**, 210–214 (2014).

23. Milo, A., Neel, A. J., Toste, F. D. & Sigman, M. S. A data-intensive approach to mechanistic elucidation applied to chiral anion catalysis. *Science.* **347**, 737–743 (2015).

24. Mori, K. *et al.* Prediction of suitable catalyst by 1H NMR: asymmetric synthesis of multisubstituted biaryls by chiral phosphoric acid catalyzed asymmetric bromination. *Chem. Sci.* **4**, 4235 (2013).

25. Fleischmann, M., Drettwan, D., Sugiono, E., Rueping, M. & Gschwind, R. M. Brønsted Acid Catalysis: Hydrogen Bonding versus Ion Pairing in Imine Activation. *Angew. Chemie Int. Ed.* **50**, 6364–6369 (2011).

26. Chacko, S. & Ramapanicker, R. Enantiospecific Synthesis of (-)-Cuspareine and (-)-Galipinine. *J. Heterocycl. Chem.* **52**, 1902–1906 (2015).

27. Van Hoozen, B. L. & Petersen, P. B. Vibrational tug-of-war: The pK A dependence of the broad vibrational features of strongly hydrogen-bonded carboxylic acids. *J. Chem. Phys.* **148**, 134309 (2018).

28. Bakker, H. J. & Bonn, M. Femtosecond Vibrational Spectroscopy of Aqueous Systems. in *Ultrafast Infrared Vibrational Spectroscopy* (ed. Fayer, M.) (CRC Press, 2013).

29. Elsaesser, T., Heyne, K., Huse, N. & Nibbering, E. T. J. Ultrafast vibrational dynamics of hydrogen-bonded dimers in solution. *Femtochemistry Femtobiology Ultrafast Events Mol. Sci.* **341**, 157–164 (2004).

30. Elsaesser, T. & Bakker, H. J. *Ultrafast Hydrogen Bonding Dynamics and Proton Transfer Prosesses in the Condensed Phase*. (Springer Netherlands, 2002).

31. Elsaesser, T. Ultrafast Vibrational Dynamics of Hydrogen-Bonded Dimers and Base Pairs. in *Ultrafast Infrared Vibrational Spectroscopy* (ed. Fayer, M. D.) 35–72 (CRC Press/Taylor & Francis, 2013).

32. Lehn, J.-M. From supramolecular chemistry towards constitutional dynamic chemistry and adaptive chemistry. *Chem. Soc. Rev.* **36**, 151–160 (2007).

33. Cowan, M. L. *et al.* Ultrafast memory loss and energy redistribution in the hydrogen

bond network of liquid H2O. *Nature* **434**, 199–202 (2005).

34. Nibbering, E. T. J. & Elsaesser, T. Ultrafast Vibrational Dynamics of Hydrogen Bonds in the Condensed Phase. *Chem. Rev.* **104**, 1887–1914 (2004).

35. Gündoğdu, K., Bandaria, J., Nydegger, M., Rock, W. & Cheatum, C. M. Relaxation and anharmonic couplings of the O–H stretching vibration of asymmetric strongly hydrogen-bonded complexes. *J. Chem. Phys.* **127**, 044501 (2007).

36. Du, Q., Superfine, R., Freysz, E. & Shen, Y. R. Vibrational spectroscopy of water at the vapor/water interface. *Phys. Rev. Lett.* **70**, 2313–2316 (1993).

37. Huse, N. *et al.* Anharmonic Couplings Underlying the Ultrafast Vibrational Dynamics of Hydrogen Bonds in Liquids. *Phys. Rev. Lett.* **95**, 147402 (2005).

38. Evans, J. C. Further studies of unusual effects in the infrared spectra of certain molecules. *Spectrochim. Acta* **16**, 994–1000 (1960).

39. Bratos, S. & Ratajczak, H. Profiles of hydrogen stretching IR bands of molecules with hydrogen bonds: A stochastic theory. II. Strong hydrogen bonds. *J. Chem. Phys.* **76**, 77–85 (1982).

40. Parson, W. W. *Modern Optical Spectroscopy*. *Modern Optical Spectroscopy* (Springer Berlin Heidelberg, 2015).

41. Wedler, G. *Lehrbuch der Physikalischen Chemie*. (Wiley-VCH Verlag GmbH & Co. KGaA, 2007).

42. Boyd, R. W. *Nonlinear optics*. (Academic Press, 2008).

43. Hollas, J. M. *Modern Spectroscopy*. (John Wiley & Sons, 2004).

44. Hamm, P. & Zanni, M. T. *Concepts and Methods of 2D Infrared Spectroscopy*. (Cambridge University Press, 2011).

45. Mazur, K., Bonn, M. & Hunger, J. Hydrogen Bond Dynamics in Primary Alcohols: A Femtosecond Infrared Study. *J. Phys. Chem. B* **119**, 1558–1566 (2015).

46. Hamm, P. Femtosecond IR Pump-Probe Spectroscopy of Nonlinear Energy Localization in Protein Models and Model Proteins. *J. Biol. Phys.* **35**, 17–30 (2009).

47. Elsaesser, T. Two-dimensional infrared spectroscopy of intermolecular hydrogen bonds in the condensed phase. *Acc. Chem. Res.* **42**, 1220–1228 (2009).

48. Shim, S.-H. & Zanni, M. T. How to turn your pump–probe instrument into a multidimensional spectrometer: 2D IR and Vis spectroscopiesvia pulse shaping. *Phys. Chem. Chem. Phys.* **11**, 748–761 (2009).

49. Kim, Y. S. & Hochstrasser, R. M. Applications of 2D IR Spectroscopy to Peptides, Proteins, and Hydrogen-Bond Dynamics. *J. Phys. Chem. B* **113**, 8231–8251 (2009).

50. Fayer, M. D. Dynamics of Liquids, Molecules, and Proteins Measured with Ultrafast 2D IR Vibrational Echo Chemical Exchange Spectroscopy. *Annu. Rev. Phys. Chem.* **60**, 21–38 (2009).

51. Böttcher, C. F. J. *Theory of Electric Polarization*. **1** and **2**, (Elsevier, 1978).

52. Barthel, J. & Buchner, R. Dielectric permittivity and relaxation of electrolyte solutions and their solvents. *Chem. Soc. Rev.* **21**, 263 (1992).

53. Feldman, Y., Puzenko, A. & Ryabov, Y. Dielectric relaxation phenomena in complex materials. in *Fractals, Diffusion, and Relaxation in Disordered Comploex Systems: A Special Volume of Advances in Chemical Physics* (eds. Kalmykov, Y. P., Coffey, W. T. & Rice, S. A., John Wiley & Sons, Inc., 2006).

54. Buchner, R. & Barthel, J. Kinetic processes in the liquid phase studied by high-frequency permittivity measurements. *J. Mol. Liq.* **63**, 55–75 (1995).

55. Barthel, J. *et al.* Dielectric relaxation spectroscopy of electrolyte solutions. Recent developments and prospects. *J. Mol. Liq.* **78**, 83–109 (1998).

56. Barthel, J. M. G. & Buchner, R. High frequency permittivity and its use in the investigation of solution properties. *Pure Appl. Chem.* **63**, 1473–1482 (1991).

57. Kremer, F. & Schönhals, A. *Broadband Dielectric Spectroscopy*. (Springer Berlin Heidelberg, 2003).

58. Cavell, E. A. S., Knight, P. C. & Sheikh, M. A. Dielectric relaxation in non aqueous solutions. Part 2.—Solutions of tri(n-butyl)ammonium picrate and iodide in polar solvents. *Trans. Faraday Soc.* **67**, 2225–2233 (1971).

59. Hunger, J., Stoppa, A., Thoman, A., Walther, M. & Buchner, R. Broadband dielectric response of dichloromethane. *Chem. Phys. Lett.* **471**, 85–91 (2009).

60. Barthel, J., Hetzenauer, H. & Buchner, R. Dielectric Relaxation of Aqueous Electrolyte Solutions II. Ion-Pair Relaxation of 1:2, 2:1, and 2:2 Electrolytes. *Berichte der Bunsengesellschaft für Phys. Chemie* **96**, 1424–1432 (1992).

61. Balci, M. Resonance Phenomena. in *Basic 1H- and 13C-NMR Spectroscopy* 9–24 (Elsevier, 2005).

62. Covington, A. K. & Dickinson, T. *Physical Chemistry of Organic Solvent Systems*. (Springer US, 1973).

63. Balci, M. Chemical Shift. in *Basic 1H- and 13C-NMR Spectroscopy* 25–85 (Elsevier, 2005).

64. Balci, M. Multiple-Pulse NMR Experiments. in *Basic 1H- and 13C-NMR Spectroscopy* 339–375 (Elsevier, 2005).

65. Carbajo, R. J. & Neira, J. L. *NMR for Chemists and Biologists*. (Springer Netherlands, 2013).

66. Yu, C. & Levy, G. C. Two-dimensional heteronuclear NOE (HOESY) experiments: investigation of dipolar interactions between heteronuclei and nearby protons. *J. Am. Chem. Soc.* **106**, 6533–6537 (1984).

67. Blümich, B. *Essential NMR*. (Springer International Publishing, 2019).

68. Buchner, R. What can be learnt from dielectric relaxation spectroscopy about ion solvation and association? *Pure Appl. Chem.* **80**, 1239–1252 (2008).

69. Huang, M.-M., Schneiders, K., Schulz, P. S., Wasserscheid, P. & Weingärtner, H. Ion

speciation driving chirality transfer in imidazolium-based camphorsulfonate ionic liquid solutions. *Phys. Chem. Chem. Phys.* **13**, 4126–4131 (2011).

70. Kaatze, U. Measuring the dielectric properties of materials. Ninety-year development from low-frequency techniques to broadband spectroscopy and high-frequency imaging. *Meas. Sci. Technol.* **24**, 012005 (2013).

71. Ensing, W., Hunger, J., Ottosson, N. & Bakker, H. J. On the orientational mobility of water molecules in proton and sodium terminated nafion membranes. *J. Phys. Chem. C* **117**, 12930–12935 (2013).

72. Blackham, D. V. & Pollard, R. D. An improved technique for permittivity measurements using a coaxial probe. *IEEE Trans. Instrum. Meas.* **46**, 1093–1099 (1997).

73. Balos, V., Bonn, M. & Hunger, J. Quantifying transient interactions between amide groups and the guanidinium cation. *Phys. Chem. Chem. Phys.* **17**, 28539–28543 (2015).

74. Malm, C., Kim, H., Wagner, M. & Hunger, J. Complexity in Acid-Base Titrations: Multimer Formation Between Phosphoric Acids and Imines. *Chem. - A Eur. J.* **23**, 10853–10860 (2017).

75. Göttmann, O., Kaatze, U. & Petong, P. Coaxial to circular waveguide transition as high-precision easy-to-handle measuring cell for the broad band dielectric spectrometry of liquids. *Meas. Sci. Technol.* **7**, 525–534 (1996).

76. Hunger, J., Ottosson, N., Mazur, K., Bonn, M. & Bakker, H. J. Water-mediated interactions between trimethylamine-N-oxide and urea. *Phys. Chem. Chem. Phys.* **17**, 298–306 (2015).

77. Hillegas, C. W., Tull, J. X., Goswami, D., Strickland, D. & Warren, W. S. Femtosecond laser pulse shaping by use of microsecond radio-frequency pulses. *Opt. Lett.* **19**, 737–739 (1994).

78. Shim, S.-H., Strasfeld, D. B., Fulmer, E. C. & Zanni, M. T. Femtosecond pulse shaping directly in the mid-IR using acousto-optic modulation. *Opt. Lett.* **31**, 838–840 (2006).

79. Shim, S.-H., Strasfeld, D. B., Ling, Y. L. & Zanni, M. T. Automated 2D IR spectroscopy using a mid-IR pulse shaper and application of this technology to the human islet amyloid polypeptide. *Proc. Natl. Acad. Sci.* **104**, 14197–14202 (2007).

80. Middleton, C. T., Woys, A. M., Mukherjee, S. S. & Zanni, M. T. Residue-specific structural kinetics of proteins through the union of isotope labeling, mid-IR pulse shaping, and coherent 2D IR spectroscopy. *Methods* **52**, 12–22 (2010).

81. Strasfeld, D. B., Shim, S.-H. & Zanni, M. T. Controlling Vibrational Excitation with Shaped Mid-IR Pulses. *Phys. Rev. Lett.* **99**, 038102 (2007).

82. Strasfeld, D. B., Middleton, C. T. & Zanni, M. T. Mode selectivity with polarization shaping in the mid-IR. *New J. Phys.* **11**, 105046 (2009).

83. Park, S., Kwak, K. & Fayer, M. D. Ultrafast 2D-IR vibrational echo spectroscopy: a probe of molecular dynamics. *Laser Phys. Lett.* **4**, 704–718 (2007).

84. Shim, S.-H., Strasfeld, D. B. & Zanni, M. T. Generation and characterization of phase and amplitude shaped femtosecond mid-IR pulses. *Opt. Express* **14**, 13120-13130 (2006).

85. Barrow, G. M. The Nature of Hydrogen Bonded Ion-Pairs: The Reaction of Pyridine and Carboxylic Acids in Chloroform. *J. Am. Chem. Soc.* **78**, 5802–5806 (1956).

86. Tolstoy, P. M. *et al.* Characterization of Fluxional Hydrogen-Bonded Complexes of Acetic Acid and Acetate by NMR: Geometries and Isotope and Solvent Effects. *J. Am. Chem. Soc.* **126**, 5621–5634 (2004).

87. Smirnov, S. N. *et al.* Hydrogen deuterium isotope effects on the NMR chemical shifts and geometries of intermolecular low-barrier hydrogen-bonded complexes. *J. Am. Chem. Soc.* **118**, 4094–4101 (1996).

88. Tolstoy, P. M., Koeppe, B., Denisov, G. S. & Limbach, H.-H. Combined NMR and UV/Vis Spectroscopy in the Solution State: Study of the Geometries of Strong OHO Hydrogen Bonds of Phenols with Carboxylic Acids. *Angew. Chemie Int. Ed.* **48**, 5745–5747 (2009).

89. Brycki, B. & Szafran, M. Infrared and 1H nuclear magnetic resonance studies of hydrogen bonds in some pyridine N-oxide trifluoroacetates and their deuteriated analogues in dichloromethane. *J. Chem. Soc. Perkin Trans. 2* 1333-1338 (1982).

90. Koeppe, B. *et al.* Polar solvent fluctuations drive proton transfer in hydrogen bonded complexes of carboxylic acid with pyridines: NMR, IR and ab initio MD study. *Phys. Chem. Chem. Phys.* **19**, 1010–1028 (2017).

91. Koeppe, B., Guo, J., Tolstoy, P. M., Denisov, G. S. & Limbach, H.-H. Solvent and H/D Isotope Effects on the Proton Transfer Pathways in Heteroconjugated Hydrogen-Bonded Phenol-Carboxylic Acid Anions Observed by Combined UV–vis and NMR Spectroscopy. *J. Am. Chem. Soc.* **135**, 7553–7566 (2013).

92. Jarczewski, A. & Hubbard, C. D. A review of proton transfer reactions between various carbon-acids and amine bases in aprotic solvents. *J. Mol. Struct.* **649**, 287–307 (2003).

93. Greindl, J., Hioe, J., Sorgenfrei, N., Morana, F. & Gschwind, R. M. Brønsted Acid Catalysis—Structural Preferences and Mobility in Imine/Phosphoric Acid Complexes. *J. Am. Chem. Soc.* **138**, 15965–15971 (2016).

94. Mori, K. *et al.* Enantioselective Synthesis of Multisubstituted Biaryl Skeleton by Chiral Phosphoric Acid Catalyzed Desymmetrization/Kinetic Resolution Sequence. *J. Am. Chem. Soc.* **135**, 3964–3970 (2013).

95. Sorgenfrei, N. *et al.* NMR Spectroscopic Characterization of Charge Assisted Strong Hydrogen Bonds in Brønsted Acid Catalysis. *J. Am. Chem. Soc.* **138**, 16345–16354 (2016).

96. Sharif, S. *et al.* NMR Localization of Protons in Critical Enzyme Hydrogen Bonds. *J. Am. Chem. Soc.* **129**, 9558–9559 (2007).

97. Gridnev, I. D., Kouchi, M., Sorimachi, K. & Terada, M. On the mechanism of stereoselection in direct Mannich reaction catalyzed by BINOL-derived phosphoric acids. *Tetrahedron Lett.* **48**, 497–500 (2007).

98. Grayson, M. N. & Goodman, J. M. Understanding the mechanism of the asymmetric propargylation of aldehydes promoted by 1,1'-bi-2-naphthol-derived catalysts. *J. Am. Chem. Soc.* **135**, 6142-6148 (2013).

99. Marcelli, T., Hammar, P. & Himo, F. Phosphoric Acid Catalyzed Enantioselective Transfer Hydrogenation of Imines: A Density Functional Theory Study of Reaction Mechanism and the Origins of Enantioselectivity. *Chem. - A Eur. J.* **14**, 8562–8571 (2008).

100. Reid, J. P., Simón, L. & Goodman, J. M. A Practical Guide for Predicting the Stereochemistry of Bifunctional Phosphoric Acid Catalyzed Reactions of Imines. *Acc. Chem. Res.* **49**, 1029–1041 (2016).

101. Simón, L. & Goodman, J. M. Theoretical Study of the Mechanism of Hantzsch Ester Hydrogenation of Imines Catalyzed by Chiral BINOL-Phosphoric Acids. *J. Am. Chem. Soc.* **130**, 8741–8747 (2008).

102. Buchner, R. & Hefter, G. Interactions and dynamics in electrolyte solutions by dielectric spectroscopy. *Phys. Chem. Chem. Phys.* **11**, 8984–8999 (2009).

103. Golubev, N. S., Denisov, G. S., Smirnov, S. N., Shchepkin, D. N. & Limbach, H.-H. Evidence by NMR of Temperature-dependent Solvent Electric Field Effects on Proton Transfer and Hydrogen Bond Geometries. *Zeitschrift für Phys. Chemie* **196**, 73–84 (1996).

104. Giacalone, F., Gruttadauria, M., Agrigento, P. & Noto, R. Low-loading asymmetric organocatalysis. *Chem. Soc. Rev.* **41**, 2406-2447 (2012).

105. Terada, M., Machioka, K. & Sorimachi, K. High substrate/catalyst organocatalysis by a chiral Brønsted acid for an enantioselective aza-ene-type reaction. *Angew. Chemie Int. Ed.* **45**, 2254–2257 (2006).

106. Li, N. *et al.* Asymmetric Amplification in Phosphoric Acid Catalyzed Reactions. *Angew. Chemie Int. Ed.* **49**, 6378–6381 (2010).

107. Hatano, M., Moriyama, K., Maki, T. & Ishihara, K. Which is the actual catalyst: Chiral phosphoric acid or chiral calcium phosphate? *Angew. Chemie Int. Ed.* **49**, 3823–3826 (2010).

108. Čorić, I. & List, B. Asymmetric spiroacetalization catalysed by confined Brønsted acids. *Nature* **483**, 315–319 (2012).

109. Das, S. *et al.* Nitrated Confined Imidodiphosphates Enable a Catalytic Asymmetric Oxa-Pictet–Spengler Reaction. *J. Am. Chem. Soc.* **138**, 9429–9432 (2016).

110. Liu, L. *et al.* Confined Acid-Catalyzed Asymmetric Carbonyl–Ene Cyclization. *J. Am. Chem. Soc.* **137**, 13268–13271 (2015).

111. Neese, F. The ORCA program system. *WIREs Comput. Mol. Sci.* **2**, 73–78 (2012).

112. Fischer, C. F. *Hartree--Fock method for atoms. A numerical approach*. (John Wiley and Sons, Inc.,New York, 1977).

113. Eichkorn, K. *et al.* Auxiliary basis sets to approximate Coulomb potentials (Chem . Phys . Letters 240 (1995) 283) * Auxiliary basis sets to approximate Coulomb potentials. *Chem. Phys. Lett.* **240**, 283–290 (1995).

114. Sinnecker, S., Rajendran, A., Klamt, A., Diedenhofen, M. & Neese, F. Calculation of Solvent Shifts on Electronic g -Tensors with the Conductor-Like Screening Model (COSMO) and Its Self-Consistent Generalization to Real Solvents (Direct COSMO-RS). *J. Phys. Chem. A* **110**, 2235–2245 (2006).

115. Kaupmees, K., Tolstoluzhsky, N., Raja, S., Rueping, M. & Leito, I. On the Acidity and Reactivity of Highly Effective Chiral Brønsted Acid Catalysts: Establishment of an Acidity Scale. *Angew. Chemie Int. Ed.* **52**, 11569–11572 (2013).

116. Ouellet, S. G., Walji, A. M. & Macmillan, D. W. C. Enantioselective Organocatalytic Transfer Hydrogenation Reactions using Hantzsch Esters. *Acc. Chem. Res.* **40**, 1327–1339 (2007).

117. Guo, Q.-S., Du, D.-M. & Xu, J. The Development of Double Axially Chiral Phosphoric Acids and Their Catalytic Transfer Hydrogenation of Quinolines. *Angew. Chemie Int. Ed.* **47**, 759–762 (2008).

118. Rueping, M., Sugiono, E., Azap, C., Theissmann, T. & Bolte, M. Enantioselective Brønsted Acid Catalyzed Transfer Hydrogenation: Organocatalytic Reduction of Imines. *Org. Lett.* **7**, 3781–3783 (2005).

119. Renzi, P., Hioe, J. & Gschwind, R. M. Decrypting Transition States by Light : Photoisomerization as a Mechanistic Tool in Brønsted Acid Catalysis. *J. Am. Chem. Soc.* 139, 6752–6760 (2017).

120. Pastor, J. *et al.* Revised Theoretical Model on Enantiocontrol in Phosphoric Acid Catalyzed H -Transfer Hydrogenation of Quinoline. *J. Org. Chem.* **83**, 2779–2787 (2018).

121. Hammes-Schiffer, S. Catalysts by Design: The Power of Theory. *Acc. Chem. Res.* **50**, 561–566 (2017).

122. Dhayalan, V., Gadekar, S. C., Alassad, Z. & Milo, A. Unravelling mechanistic features of organocatalysis with in situ modifications at the secondary sphere. *Nat. Chem.* **11**, 543–551 (2019).

123. Malm, C., Prädel, L. A., Marekha, B., Grechko, M. & Hunger, J. Vibrational dynamics of doubly ionic hydrogen bonded Brønsted acid -base pairs and multimers. *submitted*

124. Samoilichenko, Y. *et al.* A mechanistic study of the Lewis acid–Brønsted base–Brønsted acid catalysed asymmetric Michael addition of diethyl malonate to cyclohexenone. *Catal. Sci. Technol.* **7**, 90–101 (2017).

125. Chen, J., Brooks, C. L. & Scheraga, H. A. Revisiting the Carboxylic Acid Dimers in Aqueous Solution: Interplay of Hydrogen Bonding, Hydrophobic Interactions, and Entropy †. *J. Phys. Chem. B* **112**, 242–249 (2008).

126. Amenta, V. *et al.* Interplay of Self-Association and Solvation in Polar Liquids. *J. Am. Chem. Soc.* **135**, 12091–12100 (2013).

127. Reid, J. P. & Goodman, J. M. Selecting Chiral BINOL-Derived Phosphoric Acid Catalysts: General Model To Identify Steric Features Essential for Enantioselectivity. *Chem. - A Eur. J.* **23**, 14248–14260 (2017).

128. Simón, L. & Goodman, J. M. A model for the enantioselectivity of imine reactions catalyzed by BINOL-phosphoric acid catalysts. *J. Org. Chem.* **76**, 1775–1788 (2011).

129. Melikian, M., Gramüller, J., Hioe, J., Greindl, J. & Gschwind, R. M. Brønsted acid catalysis – the effect of 3,3′-substituents on the structural space and the stabilization of imine/phosphoric acid complexes. *Chem. Sci.* **10**, 5226–5234 (2019).

130. Geraldes, C. F. G. C., Sherry, A. D., Marques, M. P. M., Alpoim, M. C. & Cortes, S. Protonation scheme for some triaza macrocycles studied by potentiometry and NMR spectroscopy. *J. Chem. Soc. Perkin Trans. 2* 137 (1991).

131. Szakács, Z., Kraszni, M. & Noszál, B. Determination of microscopic acid–base parameters from NMR–pH titrations. *Anal. Bioanal. Chem.* **378**, 1428–1448 (2004).

132. Chu, F., Flatt, L. S. & Anslyn, E. V. Complexation of Phosphoric Acid Diesters with Polyaza-Clefts in Chloroform: Effects of Phosphodiester Dimerization, Changing Cavity Size, and Preorganizing Amine Recognition Units. *J. Am. Chem. Soc.* **116**, 4194–4204 (1994).

133. Foster, R. & Fyfe, C. A. Interaction of electron acceptors with bases. Part 15.—Determination of association constants of organic charge-transfer complexes by n.m.r. spectroscopy. *Trans. Faraday Soc.* **61**, 1626–1631 (1965).

134. Hladílková, J. *et al.* Effects of End-Group Termination on Salting-Out Constants for Triglycine. *J. Phys. Chem. Lett.* **4**, 4069–4073 (2013).

135. Xu, M., Eyring, E. M. & Petrucci, S. Dielectric relaxation of chloroform and chloroform-cyclohexane mixtures at gigahertz and terahertz frequencies. The inertial term. *J. Mol. Liq.* **73–74**, 41–48 (1997).

136. Mayer, U., Gutmann, V. & Gerger, W. The acceptor number - A quantitative empirical parameter for the electrophilic properties of solvents. *Monatshefte für Chemie* **106**, 1235–1257 (1975).

137. Hansen, C. M. The Universality of the Solubility Parameter. *Ind. Eng. Chem. Prod. Res. Dev.* **8**, 2–11 (1969).

138. More, G. V. & Bhanage, B. M. Chiral phosphoric acid catalyzed asymmetric transfer hydrogenation of quinolines in a sustainable solvent. *Tetrahedron: Asymmetry* **26**, 1174–1179 (2015).

139. Pearson, R. G. & Williams, F. V. Rates of Ionization of Pseudo Acids. 1 V. Steric Effects in the Base-catalyzed Ionization of Nitroethane. *J. Am. Chem. Soc.* **75**, 3073–3075 (1953).

140. Jones, G. Quinolines, Part 2. in *Chemistry of Hetereocyclic Compounds: A Series of Monographs* (ed. Jones, G.) 698 (John Wiley & Sons, 2009).

141. Kaatze, U., Pottel, R. & Wallusch, A. A new automated waveguide system for the precise measurement of complex permittivity of low-to-high-loss liquids at microwave frequencies. *Meas. Sci. Technol.* **6**, 1201–1207 (1995).

142. Parr, R. G. & Yang, W. Density-Functional Theory of the Electronic Structure of Molecules. *Annu. Rev. Phys. Chem.* **46**, 701–728 (1995).

143. Hohenberg, P. & Kohn, W. Inhomogeneous Electron Gas. *Phys. Rev.* **136**, B864–B871 (1964).

144. Kohn, W. & Sham, L. J. Self-Consistent Equations Including Exchange and Correlation Effects. *Phys. Rev.* **140**, A1133–A1138 (1965).

145. Becke, A. D. Density-functional thermochemistry. III. The role of exact exchange. *J. Chem. Phys.* **98**, 5648–5652 (1993).

146. Petersson, G. A. *et al.* A complete basis set model chemistry. I. The total energies of closed-shell atoms and hydrides of the first-row elements. *J. Chem. Phys.* **89**, 2193–2218 (1988).

147. Petersson, G. A. & Al-Laham, M. A. A complete basis set model chemistry. II. Open-shell systems and the total energies of the first-row atoms. *J. Chem. Phys.* **94**, 6081–6090 (1991).

148. Frisch, M. J. *et al.* Gaussian 09, Revision B.01. *Gaussian, Inc., Wallingford CT,* (2010).

149. Gilli, P., Pretto, L., Bertolasi, V. & Gilli, G. Predicting Hydrogen-Bond Strengths from Acid–Base Molecular Properties. The p K a Slide Rule: Toward the Solution of a Long-Lasting Problem. *Acc. Chem. Res.* **42**, 33–44 (2009).

150. Petersen, P. B., Roberts, S. T., Ramasesha, K., Nocera, D. G. & Tokmakoff, A. Ultrafast N–H Vibrational Dynamics of Cyclic Doubly Hydrogen-Bonded Homo- and Heterodimers. *J. Phys. Chem. B* **112**, 13167–13171 (2008).

151. Carra, C., Iordanova, N. & Hammes-Schiffer, S. Proton-Coupled Electron Transfer in a Model for Tyrosine Oxidation in Photosystem II. *J. Am. Chem. Soc.* **125**, 10429–10436 (2003).

152. Perrin, C. L. & Nielson, J. B. "Strong" hydrogen bonds in chemistry and biology. *Annu. Rev. Phys. Chem.* **48**, 511–544 (1997).

153. Skubi, K. L., Blum, T. R. & Yoon, T. P. Dual Catalysis Strategies in Photochemical Synthesis. *Chem. Rev.* **116**, 10035–10074 (2016).

154. Hadzi, D. Infrared spectra of strongly hydrogen-bonded systems. *Pure Appl. Chem.* **11**, 435–453 (1965).

155. Zundel, G. Hydrogen Bonds with Large Proton Polarizability and Proton Transfer Processes in Electrochemistry and Biology. in *Advances in Chemical Physics Volume 111* (eds. Prigogine, I. & Rice, S. A.) 1–217 (John Wiley & Sons, Inc., 1999).

156. Eigen, M. Proton Transfer, Acid-Base Catalysis, and Enzymatic Hydrolysis. Part I: Elementary Processes. *Angew. Chemie Int. Ed.* **3**, 1–19 (1964).

157. Szafran, M. Recent aspects of the proton transfer reaction in H-bonded complexes. *J. Mol. Struct.* **381**, 39–64 (1996).

158. Stingel, A. M., Calabrese, C. & Petersen, P. B. Strong Intermolecular Vibrational Coupling through Cyclic Hydrogen-Bonded Structures Revealed by Ultrafast Continuum Mid-IR Spectroscopy. *J. Phys. Chem. B* **117**, 15714–15719 (2013).

159. Stingel, A. M. & Petersen, P. B. Couplings Across the Vibrational Spectrum Caused by Strong Hydrogen Bonds: A Continuum 2D IR Study of the 7-Azaindole–Acetic

Acid Heterodimer. *J. Phys. Chem. B* **120**, 10768–10779 (2016).

160. Huyskens, P. L., Luck, W. A. P. & Zeegers-Huyskens, T. *Intermolecular Forces*. (Springer Berlin Heidelberg, 1991).

161. Ashworth, C. R., Matthews, R. P., Welton, T. & Hunt, P. A. Doubly ionic hydrogen bond interactions within the choline chloride–urea deep eutectic solvent. *Phys. Chem. Chem. Phys.* **18**, 18145–18160 (2016).

162. Heyne, K. *et al.* Coherent low-frequency motions of hydrogen bonded acetic acid dimers in the liquid phase. *J. Chem. Phys.* **121**, 902–913 (2004).

163. Detoni, S. & Hadži, D. Hydroxyl bands in the infra-red spectra of organophosphoric and phosphinic acids. *Spectrochim. Acta* **20**, 949–955 (1964).

164. Peppard, D. F., Ferraro, J. R. & Mason, G. W. The preparation, physical properties and infra-red spectra of several new organophosphonates. *J. Inorg. Nucl. Chem.* **12**, 60–70 (1959).

165. Maji, R., Mallojjala, S. C. & Wheeler, S. E. SI Chiral phosphoric acid catalysis: From numbers to insights. *Chem. Soc. Rev.* **47**, 1142–1158 (2018).

166. Hadzi, D. Spectroscopic and Structural Aspects of Very Strong Hydrogen Bonds. *Chimia (Aarau).* **26**, 7–13 (1972).

167. Claydon, M. F. & Sheppard, N. The nature of "A,B,C"-type infrared spectra of strongly hydrogen-bonded systems; pseudo-maxima in vibrational spectra. *J. Chem. Soc. D* 1431–1433 (1969).

168. Bratos, S. Profiles of hydrogen stretching ir bands of molecules with hydrogen bonds: A stochastic theory. I. Weak and medium strength hydrogen bonds. *J. Chem. Phys.* **63**, 3499–3509 (1975).

169. Odinokov, S. E. & Iogansen, A. V. Torsional γ(OH) vibrations, Fermi resonance [2γ(OH) ⇐ ν(OH)] and isotopic effects in i.r. spectra of H-complexes of carboxylic acids with strong bases. *Spectrochim. Acta Part A Mol. Spectrosc.* **28**, 2343–2350 (1972).

170. Šoptrajanov, B., Jovanovski, G., Kuzmanovski, I. & Stefov, V. Fourier Transform Vibrational Spectra of Magnesium Hydrogenphosphate Trihydrate. I. The O-H Stretching Region. *Spectrosc. Lett.* **31**, 1191–1205 (1998).

171. Van Hoozen, B. L. & Petersen, P. B. Origin of the Hadži ABC structure: An ab initio study. *J. Chem. Phys.* **143**, 184305 (2015).

172. Giebels, I. A. M. E., van den Broek, M. A. F. H., Kropman, M. F. & Bakker, H. J. Vibrational dynamics of hydrogen-bonded HCl-diethyl ether complexes. *J. Chem. Phys.* **112**, 5127–5132 (2000).

173. King, J. T., Baiz, C. R. & Kubarych, K. J. Solvent-Dependent Spectral Diffusion in a Hydrogen Bonded "Vibrational Aggregate". *J. Phys. Chem. A* **114**, 10590–10604 (2010).

174. Hanna, G. & Geva, E. Computational study of the signature of hydrogen-bond strength on the infrared spectra of a hydrogen-bonded complex dissolved in a polar liquid. *Chem. Phys.* **370**, 201–207 (2010).

175. Stare, J., Mavri, J., Ambrožič, G. & Hadži, D. Strong intramolecular hydrogen bonds. Part I. Vibrational frequencies of the OH group in some picolinic acid N -oxides predicted from DFT calculated potentials and located in the infrared spectra. *J. Mol. Struct. THEOCHEM* **500**, 429–440 (2000).

176. Grafton, A. B. & Cheatum, C. M. Two-dimensional infrared study of the C D and C O stretching vibrations in strongly hydrogen-bonded complexes. *Chem. Phys.* **512**, 3–12 (2018).

177. Daly, C. A. *et al.* Decomposition of the Experimental Raman and Infrared Spectra of Acidic Water into Proton, Special Pair, and Counterion Contributions. *J. Phys. Chem. Lett.* **8**, 5246–5252 (2017).

178. Cannon, C. G. The nature of hydrogen bonding. *Spectrochim. Acta* **10**, 341–368 (1958).

179. Fournier, J. A., Carpenter, W. B., Lewis, N. H. C. & Tokmakoff, A. Broadband 2D IR spectroscopy reveals dominant asymmetric H5O2+ proton hydration structures in acid solutions. *Nat. Chem.* **10**, 932–937 (2018).

180. Bredenbeck, J., Helbing, J., Kolano, C. & Hamm, P. Ultrafast 2D–IR Spectroscopy of Transient Species. *ChemPhysChem* **8**, 1747–1756 (2007).

181. Cho, M. Coherent Two-Dimensional Optical Spectroscopy. *Chem. Rev.* **108**, 1331–1418 (2008).

182. Cyran, J. D., Nite, J. M. & Krummel, A. T. Characterizing Anharmonic Vibrational Modes of Quinones with Two-Dimensional Infrared Spectroscopy. *J. Phys. Chem. B* **119**, 8917–8925 (2015).

183. Grimme, S., Ehrlich, S. & Goerigk, L. Effect of the damping function in dispersion corrected density functional theory. *J. Comput. Chem.* **32**, 1456–1465 (2011).

184. Scalmani, G. & Frisch, M. J. Continuous surface charge polarizable continuum models of solvation. I. General formalism. *J. Chem. Phys.* **132**, 114110 (2010).

185. Frisch, M. J. . *et al.* Gaussian 16 B.01. *Gaussian, Inc., Wallingford CT,* (2016).

186. Colbert, D. T. & Miller, W. H. A novel discrete variable representation for quantum mechanical reactive scattering via the S-matrix Kohn method. *J. Chem. Phys.* **96**, 1982–1991 (1992).

187. Rosenfeld, D. E., Kwak, K., Gengeliczki, Z. & Fayer, M. D. Hydrogen Bond Migration between Molecular Sites Observed with Ultrafast 2D IR Chemical Exchange Spectroscopy. *J. Phys. Chem. B* **114**, 2383–2389 (2010).

188. Lindemann, R. & Zundel, G. Polarizability, proton transfer and symmetry of energy surfaces of carboxylic acid—N-base hydrogen bonds. Infrared investigations. *J. Chem. Soc., Faraday Trans. 2* **73**, 788–803 (1977).

189. Hunger, J. *et al.* Hydrogen-bond dynamics in a protic ionic liquid: Evidence of large-angle jumps. *J. Phys. Chem. Lett.* **3**, 3034–3038 (2012).

190. Zheng, Z.-P. P. *et al.* Ionic liquids: Not only structurally but also dynamically heterogeneous. *Angew. Chemie Int. Ed.* **54**, 687–690 (2015).

191. Rezus, Y. L. A. & Bakker, H. J. On the orientational relaxation of HDO in liquid water. *J. Chem. Phys.* **123**, 114502 (2005).